2010

A fast ascent trajectory optimization method for hypersonic air-breathing vehicles

Oscar Jaime Murillo
Iowa State University

Recommended Citation

Murillo, Oscar Jaime, "A fast ascent trajectory optimization method for hypersonic air-breathing vehicles" (2010). *Graduate Theses and Dissertations*. 11825.
https://lib.dr.iastate.edu/etd/11825

A fast ascent trajectory optimization method for hypersonic air-breathing vehicles

by

Oscar J Murillo Jr

A dissertation submitted to the graduate faculty

in partial fulfillment of the requirements for the degree of

DOCTOR OF PHILOSOPHY

Major: Aerospace Engineering

Program of Study Committee:
Ping Lu, Major Professor
Stephen Holland
Atul Kelkar
Zhi J Wang
Qingze Zou

Iowa State University

Ames, Iowa

2010

DEDICATION

To my wife, Amy, for her love and patience through graduate school and while working on my dissertation. To Mom and Dad, for the support they gave me while in school.

TABLE OF CONTENTS

LIST OF TABLES

LIST OF FIGURES

ABSTRACT

The objective of this dissertation is to investigate a fast and reliable method to generate three-dimensional optimal ascent trajectories for hypersonic air-breathing vehicles. The problem is notoriously difficult because of the strong nonlinear coupling amongst aerodynamics, propulsion, vehicle attitude and trajectory state. As such an algorithm matures, the ultimate goal is to realize optimal closed-loop ascent guidance for hypersonic air-breathing vehicles. The problem is formulated as a fuel-optimal control problem. The corresponding necessary conditions are given. It is shown how the original problem of search for the optimal control commands can be reduced to a univariate root-finding problem at each point along the trajectory. A finite difference scheme is used to numerically solve the associated two-point-boundary-value problem. Evaluation of the approach is done through open-loop solutions and closed-loop simulations. The results show promising potential of the proposed approach as a rapid trajectory optimization tool for the class of hypersonic air-breathing vehicles.

CHAPTER 1. INTRODUCTION

1.1 History of Hypersonic Vehicles

The term *Hypersonic* was first used in 1946 by Hsue-shen Tsien, an aerodynamicist at the California Institute of Technology (1). The term describes flight "at speeds where aerodynamic heating dominates the physics of the problem,"(1) which, on average, are speeds greater than Mach 5. Vehicles that exceed that range are missiles, rockets, and the Space Shuttle. However, the holy grail in the aerospace industry is a single-stage, reusable, air-breathing vehicle that can achieve orbit. The desire is driven by the reduction in cost of payloads delivered to low Earth orbit. Such a vehicle could deliver payloads into orbit by entering orbit itself or releasing the payload and return back for a runway landing.

In 1957, Convair was first to investigate a combined engine system that allowed the vehicle to take off from a runway and enter orbit(1). The concept, called Space Plane, had highly-swept wings, and had a length of 235 feet. Gross take off weight was 450,000 pounds, of which 270,000 pounds was fuel. Rocket power would accelerate the vehicle to Mach 3 and to an altitude of 40,000 feet and then transition to ramjets. At Mach 7 the ramjets would shut down and move back to rocket power.

The inability for the Convair Space Plane to use an air-breathing engine to propel past Mach 7 was due to the capability of the ramjet engine. The answer to that problem was a scramjet (supersonic ramjet) engine. The first open-literature study of theoretic scramjet performance was published in 1958 by Weber and MacKay at NACA's Lewis

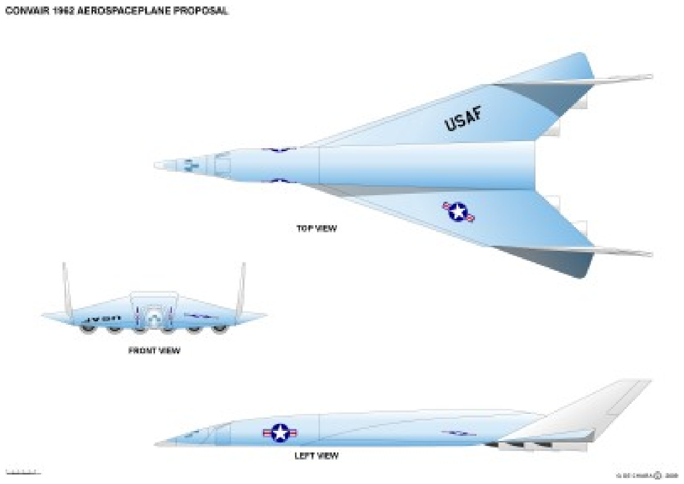

Figure 1.1 Convair's Space Plane Concept

Flight Propulsion Laboratory(2). The advantage of such an engine is the ability for a single unit that could take off from a runway and go into orbit. The Aerospace Plane concept continued in the late 50's and 60's with companies like Lockheed and Republic Aviation joining in the design of a single-stage to orbit (SSTO) vehicle.

The desire for a SSTO vehicle faded after the Aerospace Plane era of the 50's and 60's. It was not until the Ronald Reagan administration implemented the Strategic Defense Initiative (SDI) that an interest in a space plane concept returned. The result of SDI's expectation of high demand in access to space was the National Aerospace Plane (NASP), designated the X-30. NASP had several different iterations, beginning with the program baseline, a result of the Copper Canyon studies. Following this initial design was the government baseline, which had a gross weight of 80,000 pounds. Five companies then developed their own conceptual designs, with the following weight estimates for NASP listed in Tabel 1.1.

NASP continued through the early 90's. Figure 1.2 shows the concept drawing of the X-30 in 1990. The vehicle had grown to weigh 400,000 pounds, used two vertical stabilizers instead of one, three scramjet engines, and a single rocket engine that gave approximately 60,000 pounds of thrust. Faced with budget overruns and delays, the Air

Table 1.1 Weight Estimates for NASP

Rockwell International	175,000 pounds
McDonnell Douglas	245,000 pounds
General Dynamics	280,000 pounds
Boeing	340,000 pounds
Lockheed	375,000 pounds

Force initiated the formal termination of NASP in 1995.

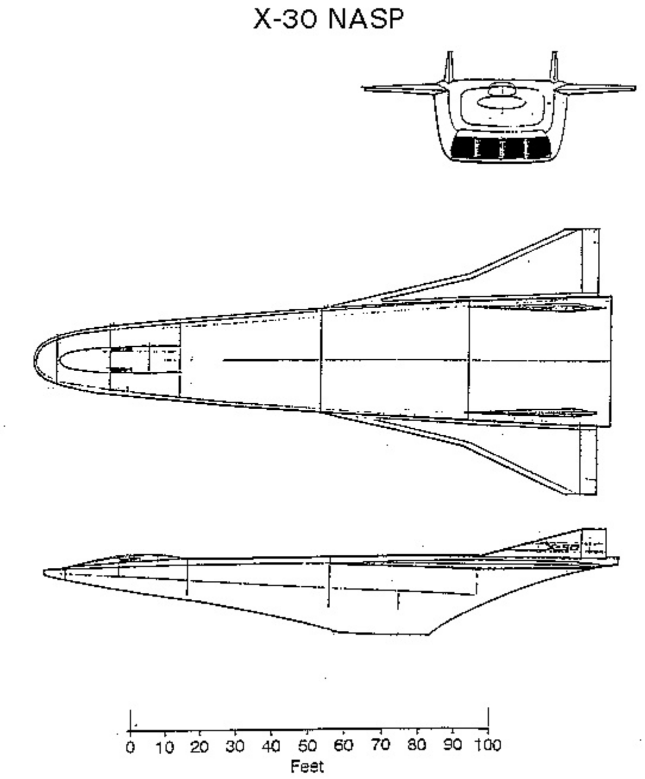

Figure 1.2 X-30 Concept of 1990

Research on hypersonic flight continued on even after the end of NASP. A component of the Aerospace Plane concept that had not been flight tested was the scramjet engine. NASA's Hyper-X (X-43A) program was designed to test such critical technologies. The program was announced in 1996. The vehicle was 12 feet long and weighed 2,800 pounds. The vehicle was designed to be boosted to test conditions by a Pegasus rocket and would then separate for free flight. Figures 1.3 and 1.4 are images of the vehicle, while Figure 1.5

depicts the trajectory of the vehicle.

Figure 1.3 NASA Hyper-X (X-43A)

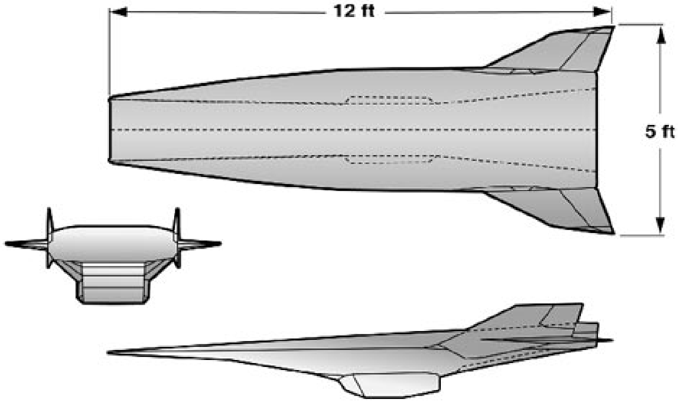

Figure 1.4 Layout Diagram of Hyper-X (X-43A)

Three vehicles were built for flight test. The first two vehicles were planned Mach 7 flights and the last vehicle was slated for a Mach 10 flight. The first flight attempt occurred in June 2001. The Pegasus was air-dropped at 24,000 feet but after about eight seconds the control surfaces began to fail and the vehicle started going out of control. The safety officer initiated the termination system and the first vehicle did not have

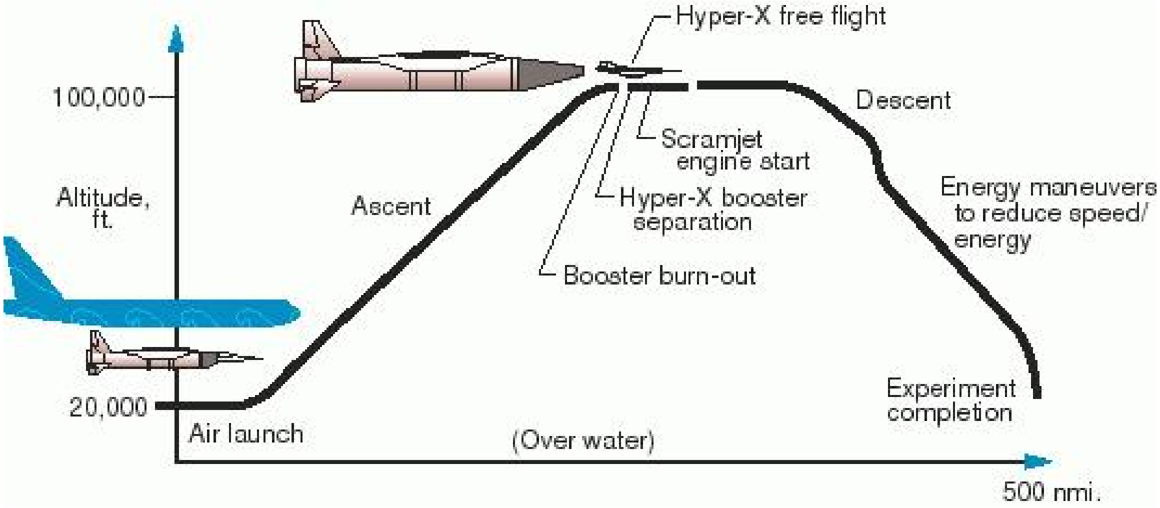

Figure 1.5 NASA Hyper-X (X-43A) Trajectory

the opportunity to fly. The second flight took place in March 2004, after analysis was conducted to fix the issues encountered in the first flight. This time the booster rocket was successful in taking the X-43A to the Mach 7 test condition and the first successful flight of a scramjet engine occurred. Data from the accelerometers showed that the X-43A gained speed while the engine was on. In November of that same year the final X-43A vehicle took flight and was tested at Mach 9.65, for a total scramjet engine on time of 10 to 12 seconds.

In early 2004, following the success of X-43A, the Air Force Research Laboratory (AFRL) selected a Pratt & Whitney and Boeing Phantom Works to began flight test on the Scramjet Engine Demonstrator - Waverider. In September of 2005 the vehicles was given the X-designation X-51A. Similar to the X-43A, the X-51A would be carried by a B-52 to approximately 50,000 ft and then rocket boosted to between Mach 4.6 to Mach 4.8. The 25 foot long vehicle would separate and the scramjet engine ignited and ran for nearly 300 seconds, 30 times longer than the X-43A. Figure 1.6 is a artist rendering of the vehicle.

On May 25, 2010 the first X-51, Vehicle FTV-1, took flight. It was deemed a success,

Figure 1.6 X-51A Waverider

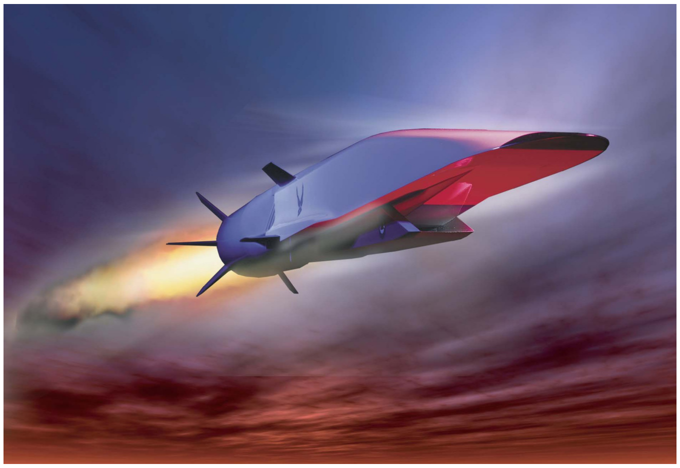

however the the flight lasted just over 200 seconds, not the planned 300 seconds. The scramjet burn time was 140 seconds. The vehicle accelerated from Mach 4.5 to Mach 5, using JP-7 jet fuel.

1.2 Cheap Access To Space

It has been said that current technology launch systems have payload costs of approximately $10,000 per pound. However, the true cost of launch is dependent on cost accounting methodology and therefore has been controversial. For the Space Shuttle, it is estimated that each launch costs $400 million which comes out to $7,000 to $8,000 per pound (4). Table 1.2 shows the cost of payloads for various vehicles, in 1994 dollars(4).

Table 1.2 Expendable launch vehicle payload costs in 1994 dollars

Launch Vehicle	Payload to 160 n.m. due East, lb	Payload $/lb
Delta	10,100	3960
Atlas Centar	18,100	6077
Titan IV	44,400	4054
Proton	38,000	1974
Saturn V	270,000	4241

The advantage of a SSTO air-breathing vehicle is the cost savings of putting a payload to orbit. By using air as the oxidizer rather than carrying it onboard, a substantial weight savings can be realized. Recent projects such as the X-33 Advanced Technology Demonstrator had a goal of reducing payload cost by an order of magnitude. Achievement of this goal could be done with a SSTO air-breathing vehicle.

1.3 Motivation

The guidance system of an aerospace vehicle impacts the performance of any aerospace vehicle. The purpose of the guidance system is to establish and/or follow a desired trajectory and control the vehicle through attitude and propulsion commands. The trajectory should meet all vehicle constraints and fulfill any objectives outlined. The system can be characterized as "outer-loop", since the system steers the vehicle in a certain direction where the flight control system (inner-loop) stabilizes the vehicles attitude.

Current guidance technology within the atmosphere is considered "open-loop." The optimal trajectory is determined offline, including off-nominal case and abort scenarios. In regards to the Space Shuttle, it can take two engineers ten days to get a first stage optimal trajectory.(5) First, a three degree of freedom (3DOF) model is used to obtain the guidance commands. At this point, the commands are checked with flight control system in a six degree of freedom (6DOF) simulation. Any changes in flight schedule can result in significant atmosphere effects, requiring a repeat in the guidance process. On day of flight, the trajectory is update with the current winds and uploaded to the flight computer.

In the 1980's it was realized that all future launch vehicles would have to incorporate onboard algorithms that "maximize payload capability, achieve high accuracy, adapt to changing mission demands and environment, and be fault tolerant while minimizing the costs for software design, life cycle maintenance, and launch operations."(3). Hardtla et al. concluded with a set of requirements for onboard guidance algorithms, a few of which are

- Easy to maintain and adapt to the current mission.
- Able to maximize the payload delivered from launch to orbit.
- Adaptable to new missions that were not in the original design requirements.
- Reliable, self-starting, and robust

To date, the goal of onboard guidance is still being sought after. The difficulty for onboard guidance of a hypersonic air-breathing SSTO vehicle is due to the nonlinear coupling between the aerodynamics, propulsion, vehicle attitude, and trajectory state. Additionally, application of optimal control theory to determine an optimal trajectory leads to a two point boundary value (TPBVP), which have been computationally intensive to solve.

1.4 Previous Work

Past research on ascent guidance for hypersonic SSTO vehicles have been done with NASP in mind. The nonlinearity of the problem has resulted in simplification of the problem to solve the TPBVP. In addition, the goal of an onboard, closed-loop guidance requires a converge solution to be obtain relatively fast.

Some of the earliest research was conducted by Corban and Calise (6; 7; 8; 9). For that research, the vehicle dynamics were restricted to a vertical plane and were represented using a four state model. In attempt to reduce the problem further for possible on-board real-time implementation, singular perturbation theory is applied. The theory separates the dynamics into two time scales, describing fast dynamics and slow dynamics. The authors suggested that altitude and flight path angle change much faster than energy and mass. The equations are reduced to the energy state approximation, which leads to the derivation of the ascent profile. When the boundary layer analysis was conducted, it resulted in an optimal feedback guidance law for control. However, when state inequality constraints are introduced, an additional calculations is needed. It is noted in (9) that the application of singular perturbation analysis onto problems with state inequality constraints is not fully developed. In order to avoid this, a non-linear transformation technique is used to control the altitude and flight path dynamics (the fast dynamics). Additional assumptions are made to employ the use of feedback linearization.

Cliff and Well (10; 11) expanded on singular perturbation method by using three-dimensional ascent dynamics. The vehicle was represented by a point mass over a spherical non-rotating Earth. A performance index using a weighted sum of time and final fuel weight is investigated, allowing a trajectory to minimize both final time and fuel consumed. To reduce the problem using time scale separation, the authors introduce three time scales. They hypothesized that cross range position, downrange position, and fuel weight changed slower than energy and velocity heading, which were slower than change in height and flight path angle. When reduced to the slow dynamics, a upper mach limit was required to find a atmospheric cruise solution. The energy-heading dynamics were also analyzed, resulting in feedback control charts that would allow a controller to be developed.

Van Buren and Mease (12; 13; 14) began their investigation by first characterizing fuel minimized optimal trajectories obtained from optimization software. They expanded their research by creating a feedback controller using geometric control theory. The dynamics of the problem are modeled by a point mass in the vertical plane over a non-rotating spherical Earth. Time scale separation is used to separate the energy and mass dynamics from the altitude and flight path angle dynamics, similar to Corban et al. Van Buren et al. verified that the time scale separation was valid by comparing their optimal trajectories to those obtained from a optimization package. Two controllers can be designed separately for each set of dynamics and combined into one feedback controller. The "slow" controller would control the slow dynamics to minimize fuel consumption while the "fast" controller would ensure time scale separation and vehicle stabilization.

Schmidt et al. (15; 16; 17) continues using energy-state methods to develop a fuel optimal ascent trajectory. The dynamics are two-dimensional describing longitudinal motion over a spherical non-rotating Earth. Their approach differs in that they changes the independent variable from time to weight of fuel burned. Because of this change, the solution algorithm is,

> "*At each energy level, E, operate the vehicle so as to maximize* dE/dW_{fuel}"
> (energy change per weight of fuel burned).

This algorithm allows the trajectory to be generated graphically. In order to handle constraints, the vehicle would fly along the constraint when the trajectory violated said constraint. A feedback controller was then developed to track the optimal trajectory.

Kremer et al. (18) realized that hard constraints could be problematic when using singular perturbation methods. For example, if the vehicle is perturbed into a constraint region, then no solution can be determined. Kremer proposed using soft constraints (i.e constraints that can be violated for short duration) in developing the optimal ascent trajectory. The soft constraint is implemented using a penalty function to discourage the solution from entering the constrained region. In this approach, a solution can be obtained when a vehicle is perturbed into a constraint region. A resulting guidance law was shown to handle a dynamic pressure constraint for the ascent guidance problem.

Lu used inverse dynamics to produce an optimal trajectory (19; 20; 21; 22; 23). He models the problem using two-dimensional point mass equations over a spherical non-rotating Earth. By using an inverse dynamic approach, he can find the solution to the problem for a given altitude and throttle profile. Those two variables are parametrized and the problem is reduced into a nonlinear programming problem. One advantage to this approach is that quick ascent profiles can be generated for a desired profile, although they would be non-optimal. In References (19) and (20), the guidance law is handled by observing the characteristics of the resulting trajectories. It was noted that there were three segments of flight, initial climb out, midcourse cruise, and final pull up. The midcourse cruise had near unity of the equivalence ratio, small angle-of-attack, slow varying flight path angle, and dynamic pressure at the maximum constraint. A feedback controller is developed that mimicked these characteristics. In Ref. (21) the guidance laws were developed to track the desired flight profiles. The guidance laws were evaluated by showing the vehicles performance in the presence of density perturbations, aerodynamic model perturbations, and engine model perturbations. Lastly, Lu investigated three-dimensional ascent profiles, but noted that the vehicle used large bank during the initial portion of flight and then remains in planar motion and having characteristics similar to two-dimensional optimal trajectories.

In Ref. (24), Paus solves the three-dimensional equations of motion for a rigid body vehicle on a spherical rotating Earth. The ascent trajectory optimization problem is reduced by linearizing the problem at discrete set of points within a time interval. The equations of motion are then integrated within each subinterval using transition matrices given piecewise constant or linear control. The controls are adjusted by using a nonlinear programming (NLP) solver that includes the path constraints. For that research, the vehicle used for evaluation was the Sänger 2 vehicle. Only the second phase of flight was addressed, where the vehicle is on ramjet power accelerating from Mach = 3 to Mach ≈ 6.8, beginning at an altitude of 19 km and ends at about 30 km. A feedback controller was generated using feedback linearization. The following onboard guidance algorithm was proposed: 1) Generate state and control estimates; 2) Evaluate cost function and boundary conditions at final time and check path constraints at the specified time intervals; 3) Adjust the final time and control using a NLP solver; 4)

Guide the vehicle along the trajectory using a feedback controller in between trajectory calculations. A feedback controller was developed using feedback linearization.

Recent research has focused on closed-loop guidance and fault tolerant autonomous systems (25). Although much of the discussion is on rocket based vehicles, the same applies to hypersonic vehicles. Specific to ascent guidance, abort planning requires time consuming trajectory planning for a range of scenarios, such as engine loss. Additionally, non-catastrophic events, such as thrust reduction or off-nominal engine performance, would effect the ability to track a predetermined trajectory and also need to be taken into consideration. Integrated vehicle health management systems are suggested to be added so that failure detection can occur, allowing both the inner loop controller and outer loop guidance system to adapt. Closed loop guidance would allow for onboard rapid re-planning of trajectories and can reduce mission design.

For onboard, closed-loop guidance to be feasible, convergence to an optimal solution need to be fast enough to be generated by an inflight computer. The approach in Lu et al.(26) was to pose the ascent guidance problem as a two point boundary value problem (TPBVP) and use a finite difference method to solve the optimal control problem. A rocket based reusable launch vehicle (RLV) was studied. An indirect method, also known as the calculus of variation method, is used for optimization. The indirect method can produce very accurate results, but are sensitive to changes to any parameter (i.e. changes to the dynamics, vehicle, etc.). Detailed mathematical analysis of each problem is required. Solution convergence was quick and showed closed-loop guidance was possible.

The same approach is used in this study, applied to a generic hypersonic vehicle (GHV). Because the method used has promise to be used closed-loop, the resulting guidance algorithm could be incorporated with a fault tolerant autonomous system. Additionally, the research done here is to expand the work done on guidance for NASP. The restriction for only vertical plane dynamics is not used here. Unlike rocket based vehicles, a hypersonic vehicle has the ability to cover a larger cross range. The inclusion of both vertical and lateral dynamics allows for an optimize trajectory to be determined given a wider range of terminal conditions. This work also avoids the two time scale separation approach. State constraints are easily incorporated into the optimal control problem for which a solution to the TPBVP can be obtained. Finally, the previous research on NASP ascent guidance used a simplified vehicle model. The approach in Ref. (26) allows for a more complex model.

1.5 Overview of Dissertation

Chapter 2 is a brief overview of optimal control theory. The general formulation of the optimal control problem is presented. The effects of both control and state variable constraints are reviewed. Additionally, inequality constraints are examined.

Chapter 3 starts by describing the coordinate systems that are involved with the ascent guidance problem. Included in the discussion is the formulation of the vehicle body axis. Next, the equations of motion for a vehicle in an inertial coordinate system are presented. Finally, the equations are nondimensionalized for better number conditioning.

Chapter 4 formulates the ascent guidance problem as an optimal control problem. The objective for the guidance algorithm is to find the vehicle orientation for any given time. Special care is taken in the derivation of the costate, optimality, and transversality equations. Path constraints that are typical for hypersonic air-breathing vehicles are considered. The result of the optimal control problem formulation is a two-point boundary value problem.

Chapter 5 describes the vehicle used in this research. The GHAME (Generic Hypersonic Aerodynamics Model Example) vehicle geometry is given, as well as descriptions of the aerodynamic data and engine model. Since the costate equations in the optimal control problem are specific to the engine model, the costate equation derivation is revisited.

Chapter 6 describes the numerical method used in solving the two point boundary value problem. The finite difference algorithm takes advantage of the special structure of the Jacobian matrix and using Gauss eliminations and sequential back substitution, results in a fast and efficient algorithm. Efficient in the sense of storage of the matrix coefficients. The boundary conditions for the Jacobian are solved analytically and described in the chapter. Finally, a secant method is used to adjust the final time because the finite difference method solves the fixed final time problem.

Chapter 7 presents the results to the ascent guidance problem. First, the solution from the finite difference method is compared to a commercial optimization software. This is done to verify and validate the technique. The commercial software is based on a pseudospectral method and used the same aerodynamic and engine model as the finite difference method. Various open-loop trajectories at different initial and final conditions are shown. This is done to demonstrate the capability of the scheme as well as to show the characteristics of the trajectories. Angle-of-attack constraints are include in some of the open-loop solutions. Closed-loop simulations were also conducted to show the feasibility of using the guidance algorithm with a flight control system. Simulations were done with varied initial and final conditions, and some included either angle-of-attack or dynamic pressure constraints. Winds were included in all the closed-loop simulations. Lastly, atmospheric and vehicle model perturbed solutions are shown.

The final chapter, Chapter 8, summarizes the research done in this dissertation.

1.6 Main Contributions

The research conducted for this dissertation was done to expand on work previous done on SSTO air-breathing hypersonic vehicles and incorporate some recent developments in on-board ascent guidance. The main contributions of this work are as follows:

- Expand on the previous research of hypersonic air-breathing guidance and generate three-dimensional fuel-optimal ascent trajectories.
- Incorporate an engine model that is dependent on the state of the vehicle so that the coupling between aerodynamics, propulsion, vehicle attitude and trajectory state are included in the development of the optimal trajectory.
- Incorporate control and state constraints that are typical to this class of vehicle.
- Validate the solution to the optimal ascent trajectory problem with a commercial available optimization software.
- Investigate the effects of initial and final conditions on the trajectory of a hypersonic air-breathing vehicle.
- Provide a guidance algorithm that can be used for onboard trajectory calculation.
- Illustrate closed-loop feasibility and capability.

CHAPTER 2. OPTIMAL CONTROL THEORY

The goal of optimal control is to create an input to a system, u^*, to drive the system along a trajectory, x^*, such that a performance index, J, is minimized.

2.1 Problem Formulation

Describe the system by

$$\dot{x}(t) = f(x,\ u,\ t) \tag{2.1}$$

where $x \in R^n$ is the state of the system, $u \in R^m$ is the control input, and t is time. The associated performance index (also described as the cost function) can be written as

$$J = \phi(x(t_f), t_f) + \int_{t_0}^{t_f} L(x(t), u(t), t) dt \tag{2.2}$$

where $\phi(x(t_f), t_f)$ is the final weighting function and depends on the final state, $x(t_f)$, and final time, t_f, $L(x(t), u(t), t)$ is the weighting function and depends on the state and input, $x(t)$ and $u(t)$ respectively, along the trajectory, and $[t_0, t_f]$ is the specified time interval. In addition to minimizing the cost function, the state must satisfy a final condition

$$\psi(x(t_f), t_f) = 0 \tag{2.3}$$

for a given function $\psi \in R^p$.

To minimize the cost function, Eq. (2.2), subject to the constraints, Eqs.(2.1) and (2.3), Lagrange multipliers are used to combine both functions with the performance index. The updated performance index to be minimized is written as

$$J' = \phi(x(t_f), t_f) + \nu^T \psi(x(t_f), t_f) + \int_{t_0}^{t_f} \left[L(x,u,t) + \lambda^T(t)(f(t)(x,u,t) - \dot{x})\right] dt \quad (2.4)$$

where $\lambda(t) \in R^n$ is the Lagrange multiplier associated with Eq. (2.1) and is a function of time since Eq. (2.1) holds true for the entire trajectory, and $\nu \in R^p$ is the constant multiplier associated with Eq. (2.3). Define the following constant function, the Hamiltonian, as

$$H(x,u,t) \triangleq L(x,u,t) + \lambda^T f(x,u,t) \quad (2.5)$$

then Eq. (2.4) can be rewritten as

$$J' = \phi(x(t_f), t_f) + \nu^T \psi(x(t_f), t_f) + \int_{t_0}^{t_f} \left[H(x,u,t) - \lambda^t \dot{x}\right] dt. \quad (2.6)$$

The calculus of variation formulation is used to minimize the augmented performance index (28; 29). The reason is because the change in J' will depend on the time and state differentials, dt and dx. If $x(t)$ is a continuous function of time, t, then the differentials $dx(t)$ and dt are not independent. However, one can define a small change in $x(t)$ that is independent of time. Define the variation in $x(t)$, $\delta x(t)$, as the incremental change in $x(t)$ when time is held fixed. The following relationship can then be established,

$$dx(t_f) = \delta x(t_f) + \dot{x}(t_f) dt_f. \quad (2.7)$$

To minimize the updated performance index, its derivative is set to zero. From Eq. (2.6), the effect of changing the independent variables can be shown to be

$$\begin{aligned} dJ' \;&=\; \left(\phi_x + \psi_x^T \nu\right)^T dx|_{t_f} + \left(\phi_t + \psi_t^T \nu\right) dt|_{t_f} + \psi^T|_{t_f} d\nu \\ &\quad + \left(H - \lambda^T \dot{x}\right) dt|_{t_f} - \left(H - \lambda^T \dot{x}\right) dt|_{t_0} \\ &\quad + \int_{t_0}^{t_f} \left[H_x^T \delta x + H_u^T \delta u - \lambda^T \delta \dot{x} + \left(H_\lambda - \dot{x}\right)^T \delta \lambda\right] dt \end{aligned} \quad (2.8)$$

where the subscript means the derivative with respect to that variable. Integration by parts can be done to eliminate the variation in $\dot{x}$,

$$-\int_{t_0}^{t_f} \lambda^T \delta \dot{x} dt = -\lambda^T \delta x|_{t_f} + \lambda^T \delta x|_{t_0} + \int_{t_0}^{t_f} \dot{\lambda}^T \delta x dt. \quad (2.9)$$

When substituting Eq. (2.9) into Eq. (2.8), the resulting terms at $t = t_f$ are dependent on both $dx(t)$ and $\delta x(t_f)$. Using Eq. (2.7), $\delta x(t_f)$ can be replaced with terms of $dx(t)$ and dt_f, resulting in

$$\begin{aligned} dJ' &= \left(\phi_x + \psi_x^T \nu - \lambda\right)^T dx|_{t_f} + \left(\phi_t + \psi_t^T \nu + H - \lambda^T \dot{x} + \lambda^T \dot{x}\right) dt|_{t_f} \\ &\quad + \psi^T|_{t_f} d\nu - \left(H - \lambda^T \dot{x} + \lambda^T \dot{x}\right) dt|_{t_0} + \lambda^T dx|_{t_0} \\ &\quad + \int_{t_0}^{t_f} \left[\left(H_x + \dot{\lambda}\right)^T \delta x + H_u^T \delta u + \left(H_\lambda - \dot{x}\right)^t \delta\lambda \right] dt \\ &= (1) dx|_{t_f} + (2) dt|_{t_f} + (3) d\nu + (4) dt|_{t_0} + (5) dx|_{t_0} + \int_{t_0}^{t_f} (6) dt. \qquad (2.10) \end{aligned}$$

Setting to zero the coefficients of the independent increments (terms 1-6 above) in Eq. (2.10) give the necessary conditions for the minimum of J', and therefore the minimum of J. First, setting to zero the three parts in term 6 results in the state equation, costate equation, and stationary condition. Since both t_0 and $x(t_0)$ are known and fixed, then terms 4 and 5 are automatically equal to zero. Term 3 is just the final-state constraint. Lastly, terms 1 and 2 need special consideration. Since $dx(t_f)$ and dt_f are not independent, they can not be independently set equal to zero. Rather, the entire expression must be zero at $t = t_f$. For fixed final state problems, $dx(t_f) = 0$ and only the term associated with dt_f is considered. For fixed final time problems, $dt_f = 0$, and the term associated with $dx(t_f)$ is considered. Table 2.1 summarizes the optimal control problem.

2.1.1 Functions of the Control Variable Constraints

Consider the optimal control problem with the following control variable equality constraint

$$C(u, t) = 0 \qquad (2.11)$$

Table 2.1 Optimal Control Problem

System Equation:	$\dot{x} = f(x,u,t), \quad t \geq t_0$
Performance Index:	$J = \phi(x(t_f),t_f) + \int_{t_0}^{t_f} L(x,u,t)dt$
Final-state Constraint:	$\psi(x(t_f),t_f) = 0$
Hamiltonian:	$H(x,u,t) = L(x,u,t) + \lambda^T f(x,u,t)$
State Equation:	$\dot{x} = \frac{\partial H}{\partial \lambda} = f, \quad t \geq t_0$
Costate Equation:	$-\dot{\lambda} = \frac{\partial H}{\partial x} = \frac{\partial f^T}{\partial x}\lambda + \frac{\partial L}{\partial x}, \quad t \leq t_f$
Stationary Condition:	$0 = \frac{\partial H}{\partial u} = \frac{\partial L}{\partial u} + \frac{\partial f^T}{\partial u}\lambda$
Boundary Conditions:	$x(t_0)$given
	$(\phi_x + \psi_x^T \nu - \lambda)^T \vert_{t_f} dx(t_f) + (\phi_t + \psi_t^T \nu + H)\vert_{t_f} dt_f = 0$

where C is a scalar function. Adjoin the constraint, Eq. (2.11), to the Hamiltonian with a Lagrange multiplier $\mu(t)$, resulting in

$$H = L + \lambda^T f + \mu C. \tag{2.12}$$

This change only effects the stationary condition, giving

$$0 = \frac{\partial H}{\partial u} = \frac{\partial L}{\partial u} + \frac{\partial f^T}{\partial u}\lambda + \mu\frac{\partial C}{\partial u}. \tag{2.13}$$

All other equations in Table 2.1 remain the same.

2.1.2 Functions of Control and State Variables Constraints

This time, consider the following constraint

$$C(x,u,t) = 0 \tag{2.14}$$

where $\partial C/\partial u \neq 0$ for any u. Using the same procedure as above, the constraint is added to the Hamiltonian to give

$$H = L + \lambda^T f + \mu C. \tag{2.15}$$

The same stationary equation given above, Eq. (2.13), applies in this case. Additionally, the costate equation is modified to give

$$-\dot{\lambda} = \frac{\partial H}{\partial x} = \frac{\partial f^T}{\partial x}\lambda + \frac{\partial L}{\partial x} + \mu\frac{\partial C}{\partial x}. \tag{2.16}$$

All other equations in Table 2.1 remain the same.

2.1.3 Functions of the State Variable Constraints

Consider a constraint which has no explicit dependence on the control variable

$$S(x, t) = 0. \tag{2.17}$$

The constraint applies to all time, $t_0 \leq t \leq t_f$, and therefore its time derivative along the path must also be zero, i.e.

$$\frac{dS}{dt} = \frac{\partial S}{\partial t} + \frac{\partial S}{\partial x}\dot{x} = \frac{\partial S}{\partial t} + \frac{\partial S}{\partial x} f(x, u, t) = 0. \tag{2.18}$$

If the above equation has an explicit dependence on u, then Eq. (2.18) is the same type of constraint as Eq. (2.14). If no explicit dependence is present, then another time derivative is taken and repeated until some explicit dependence on u does occur. If this occurs on the q-th time derivative, d^qS/dt^q, then the constraint is called a q-th order state variable equality constraint. The additional q components of x would need to be eliminated, using the following q relationships

$$\begin{bmatrix} S(x,t) \\ S^{(1)}(x,t) \\ \vdots \\ S^{(q-1)}(x,t) \end{bmatrix} = 0. \tag{2.19}$$

In this form, the qth total time derivative is treated as a control variable constraint in the form of Eq. (2.14) with the additional q equations, Eq. (2.19).

2.1.4 Inequality Constraints on the Control Variable

If instead of an equality constraint as in Eq. (2.11), the following inequality constraint on the control variable is given

$$C(u, t) \leq 0. \tag{2.20}$$

The same process is repeated, resulting in the same equations as Eqs. (2.12) and (2.13), but the following requirement applies,

$$\mu \begin{cases} \geq 0, & C = 0 \\ = 0, & C < 0. \end{cases} \tag{2.21}$$

2.1.5 Inequality Constraints on Functions of Control and State Variables

If instead of an equality constraint as in Eq. (2.14), the following inequality constraint on the control variable is given

$$C(x, u, t) \leq 0. \tag{2.22}$$

The same process as the equality constraint is followed. Define the Hamiltonian as

$$H = L + \lambda^T f + \mu C \tag{2.23}$$

where

$$\mu \begin{cases} > 0, & C = 0 \\ = 0, & C < 0 \end{cases} \tag{2.24}$$

and the costate equations are given by

$$-\dot{\lambda} = \frac{\partial H}{\partial x} = \begin{cases} \frac{\partial f^T}{\partial x}\lambda + \frac{\partial L}{\partial x} + \mu\frac{\partial C}{\partial x}, & C = 0 \\ \frac{\partial f^T}{\partial x}\lambda + \frac{\partial L}{\partial x}, & C < 0. \end{cases} \tag{2.25}$$

The stationary condition also changes to

$$0 = \frac{\partial H}{\partial u} = \frac{\partial L}{\partial u} + \frac{\partial f^T}{\partial u}\lambda + \mu\frac{\partial C}{\partial u}. \tag{2.26}$$

When $C < 0$, then $\mu = 0$ and Eq. (2.26) determines the control, $u(t)$. When $C = 0$, Eqs. (2.22) and (2.26) together determine the control, $u(t)$ and $\mu(t)$, since $\mu(t)$ is needed for Eq. (2.25).

2.1.6 Inequality Constraints on Functions of the State Variables

If instead of an equality constraint as in Eq. (2.20), the following inequality constraint on the control variable is given

$$C(x,t) \leq 0. \tag{2.27}$$

The same process as in Section 2.1.3 is used, taking successive total time derivatives of Eq. (2.27) and substituting the state equation until an expression that is explicitly dependent on u. The constraint is again refereed as a q-th order state variable inequality constraint, where q is the number of time derivatives. Now $S^{(q)}(x,u,t)$, the q-th total time derivative of S, is treated the same as $C(x,u,t)$ in Section (2.1.5). The Hamiltonian is defined as

$$H = L + \lambda^T f + \mu S^{(q)} \tag{2.28}$$

where

$$S^{(q)} = 0 \text{ on the constraint boundary,} \quad S = 0 \tag{2.29}$$

$$\mu = 0 \text{ off the constraint boundary,} \quad S < 0. \tag{2.30}$$

The costate equations are then

$$-\dot{\lambda} = \frac{\partial H}{\partial x} = \begin{cases} \frac{\partial f^T}{\partial x}\lambda + \frac{\partial L}{\partial x} + \mu\frac{\partial S^{(q)}}{\partial x}, & S = 0 \\ \frac{\partial f^T}{\partial x}\lambda + \frac{\partial L}{\partial x}, & S < 0 \end{cases} \tag{2.31}$$

and the stationary condition are given as

$$0 = \frac{\partial H}{\partial u} = \frac{\partial L}{\partial u} + \frac{\partial f^T}{\partial u}\lambda + \mu\frac{\partial S^{(q)}}{\partial u}. \tag{2.32}$$

Also, as before, the following condition is necessary for μ

$$\mu(t) \geq 0 \quad \text{on} \quad S = 0, \quad \text{if minimizing J.} \tag{2.33}$$

The constraint may only be active for part of the path. If this occurs, there may be a jump condition that is required for the costate equations. Additionally, the interior boundary conditions (the endpoints on the constraint boundary) where the constraint is active, needs to meet the following tangency constraints

$$\begin{bmatrix} S(x,t) \\ S^{(1)}(x,t) \\ \vdots \\ S^{(q-1)}(x,t) \end{bmatrix} = 0. \tag{2.34}$$

CHAPTER 3. THREE-DIMENSIONAL ASCENT GUIDANCE

3.1 Coordinate Systems

Describing the ascent guidance problem can be simplified by using different coordinate systems. Certain frames of reference “make sense” when describing the position and velocity of the vehicle. All coordinate systems used will be orthogonal and right-handed. Three different coordinate frames are used here, the Earth-Center Inertial frame, the Guidance frame, and the Vehicle Body frame.

3.1.1 Earth-Center Inertial Coordinate System

The Earth-Center Inertial (ECI) coordinate system has its origin at the center of the Earth and is shown in Figure 3.1. The equator lies in the X_I and Y_I plane, where the positive X_I direction points towards the Greenwich Meridian. The Z_I axis is parallel to the axis of rotation and points towards the north pole. Y_I completes the right hand rule.

3.1.2 Guidance Coordinate System

The Guidance coordinate system has its origin at the center of the Earth and is also shown in Figure 3.1. The x-axis, X_G, points from the origin towards the launch site, while the z-axis, Z_G, points downrange in the launch azimuth direction. The y-axis, Y_G,

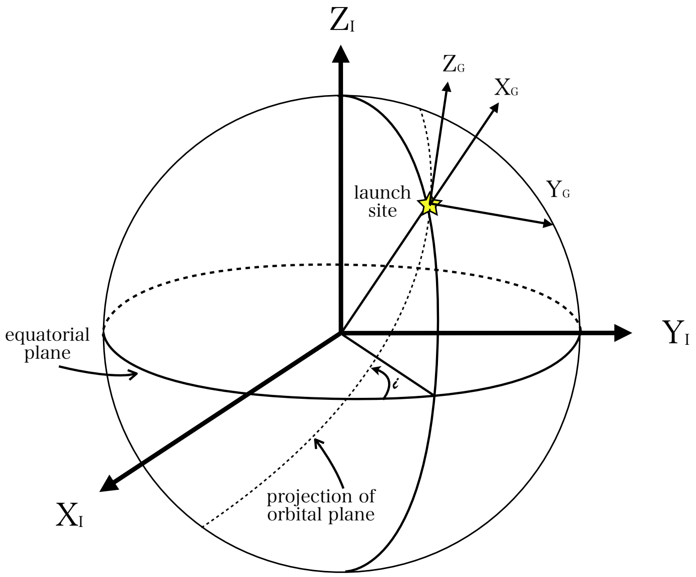

Figure 3.1 Earth Centered Inertial and Guidance Coordinate Systems

completes the right-hand system. The launch azimuth, A_z, is defined by

$$A_z = \sin^{-1}\left(\frac{\cos i}{\cos\Phi}\right), \qquad \text{for ascending orbit} \tag{3.1}$$

$$A_z = \frac{\pi}{2} + \sin^{-1}\left(\frac{\cos i}{\cos\Phi}\right), \qquad \text{for descending orbit} \tag{3.2}$$

where the longitude and geocentric latitude of the launch site is defined by (Θ, Φ), and i is the target orbital inclination.

3.1.3 Vehicle Body Coordinate System

The Vehicle Body coordinate system has its origin at the center of the aircraft and is shown in Figure 3.2. The body X-axis, X_b, points out the nose of the aircraft. The body Y-axis, Y_b, points out the right wing. The body Z-axis, Z_b, completes the right hand rule. Additionally, the figure depicts the Euler angles ϕ, θ, ψ, representing roll, pitch, and yaw, respectively.

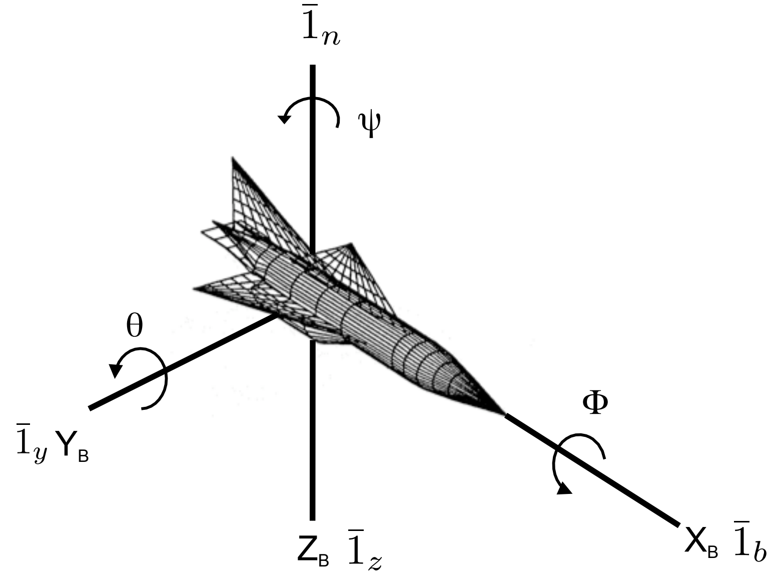

Figure 3.2 Vehicle Body Coordinate System Showing Euler Angles

3.1.4 Coordinate Transformations

The following transformation, T_{EP}, transforms coordinates from the ECI coordinate frame to the Guidance frame

$$T_{EP} = \begin{bmatrix} \cos\Theta\cos\Phi & \sin\Theta\cos\Phi & \sin\Phi \\ -\sin\Theta\cos A_z + \cos\Theta\sin\Phi\sin A_z & \cos\Theta\cos A_z + \sin\Theta\sin\Phi\sin A_z & -\cos\Phi\sin A_z \\ -\sin\Theta\sin A_z - \cos\Theta\sin\Phi\cos A_z & \cos\Theta\sin A_z - \sin\Theta\sin\Phi\cos A_z & \cos\Phi\cos A_z \end{bmatrix}. \tag{3.3}$$

The transformation from Vehicle Body frame to the Guidance frame is determine by the sequence of pitch-yaw-roll and is given by

$$T_{BP} = \begin{bmatrix} \cos\theta\cos\psi & \sin\theta\sin\phi - \cos\theta\sin\psi\cos\phi & \sin\theta\cos\phi + \cos\theta\sin\psi\sin\phi \\ \sin\psi & \cos\psi\cos\phi & -\cos\psi\sin\phi \\ -\sin\theta\cos\psi & \cos\theta\sin\phi + \sin\theta\sin\psi\cos\phi & \cos\theta\cos\phi - \sin\theta\sin\psi\sin\phi \end{bmatrix}. \tag{3.4}$$

From the transformation matrix, T_{BP}, the unit vectors of the body axes in the Guidance frame are simply the columns of the matrix. The unit vector of the body x-axis in the

Guidance frame is given by

$$\vec{\mathbf{1}}_b = \begin{bmatrix} \cos\theta\cos\psi \\ \sin\psi \\ -\sin\theta\cos\psi \end{bmatrix}. \tag{3.5}$$

The unit vector of the body y-axis in the Guidance frame is

$$\vec{\mathbf{1}}_y = \begin{bmatrix} \sin\theta\sin\phi - \cos\theta\sin\psi\cos\phi \\ \cos\psi\cos\theta \\ \cos\theta\sin\phi + \sin\theta\sin\psi\cos\phi \end{bmatrix}. \tag{3.6}$$

And finally, the unit vector of the body z-axis in the Guidance frame is

$$\vec{\mathbf{1}}_z = \begin{bmatrix} \sin\theta\cos\phi + \cos\theta\sin\psi\sin\phi \\ -\cos\psi\sin\phi \\ \cos\theta\cos\phi - \sin\theta\sin\psi\sin\phi \end{bmatrix}. \tag{3.7}$$

Also, the body z-axis can be found using

$$\vec{\mathbf{1}}_z = \vec{\mathbf{1}}_b \times \vec{\mathbf{1}}_y = -\vec{\mathbf{1}}_n \tag{3.8}$$

where $\vec{\mathbf{1}}_n$ is the body normal unit vector. Using the body axes in the Guidance frame, the Euler angles can be determined using the following equations

$$\begin{aligned} \theta &= -\tan^{-1}\left(\frac{1_{bz}}{1_{bx}}\right) && (3.9) \\ \psi &= \tan^{-1}\left(\frac{1_{by}}{1_{bx}\cos\theta - 1_{bz}\sin\theta}\right) && (3.10) \\ \phi &= -\tan^{-1}\left(\frac{1_{zy}}{1_{yy}}\right) && (3.11) \end{aligned}$$

where 1_{bx}, 1_{by}, and 1_{bz} are the components of the unit vector $\vec{\mathbf{1}}_b$, 1_{yy} is the y-component of the unit vector $\vec{\mathbf{1}}_y$, and 1_{zy} is the y-component of the unit vector $\vec{\mathbf{1}}_z$.

3.1.5 Vehicle body axis frame definitions

The vehicle body axis frame (x_b,y_b,z_b) is selected so that the vehicles flies at a zero sideslip angle(26), described as the zero-sideslip formulation. This formulation places the vehicles symmetric plane in the same plane formed by the body-axis, $\vec{\mathbf{1}}_b$, and the Earth relative velocity vector, $\vec{\mathbf{V}}_r$, resulting in the sideslip angle being zero. In the presence of any crosswinds, there is a required roll angle to null the sideslip angle. This is described as the "fly into the wind" maneuver. The unit vector for the body x-axis is the same as $\vec{\mathbf{1}}_b$. The unit vector for the body y-axis is then defined as

$$\vec{\mathbf{1}}_y = \frac{\vec{\mathbf{1}}_{V_r} \times \vec{\mathbf{1}}_b}{||\vec{\mathbf{1}}_{V_r} \times \vec{\mathbf{1}}_b||} \tag{3.12}$$

where $\vec{\mathbf{1}}_{V_r} = \vec{\mathbf{V}}_r / V_r$. The Earth relative velocity, $\vec{\mathbf{V}}_r$ is defined as

$$\vec{\mathbf{V}}_r = \vec{\mathbf{V}} - \vec{\omega}_E \times \vec{\mathbf{r}} \tag{3.13}$$

where $\vec{\omega}_E$ is the Earth rotation rate vector in the Guidance frame. The unit vector for the body z-axis is found by $\vec{\mathbf{1}}_z = \vec{\mathbf{1}}_b \times \vec{\mathbf{1}}_y$. Define the body normal unit vector by $\vec{\mathbf{1}}_n = -\vec{\mathbf{1}}_z$, then

$$\vec{\mathbf{1}}_n = \vec{\mathbf{1}}_b \times \frac{\vec{\mathbf{1}}_b \times \vec{\mathbf{V}}_r}{||\vec{\mathbf{1}}_b \times \vec{\mathbf{V}}_r||} \qquad (\ \alpha > 0\ ). \tag{3.14}$$

From Figure 3.3, it is obvious that

$$\cos\alpha = \vec{\mathbf{1}}_b^T \vec{\mathbf{1}}_{V_r} \text{ or } |\sin\alpha| = ||\vec{\mathbf{1}}_{V_r} \times \vec{\mathbf{1}}_b||. \tag{3.15}$$

Using the above definitions, when α crosses zero there is an instantaneous 180-degree rotation of $\vec{\mathbf{1}}_n$. To avoid this, $\vec{\mathbf{1}}_n$ should be defined as

$$\vec{\mathbf{1}}_n = \vec{\mathbf{1}}_b \times \frac{\vec{\mathbf{V}}_r \times \vec{\mathbf{1}}_b}{||\vec{\mathbf{1}}_b \times \vec{\mathbf{V}}_r||} \qquad (\ \alpha < 0\ ). \tag{3.16}$$

Equation (3.14) and Eq. (3.16) should be use together to determine $\vec{\mathbf{1}}_n$, depending on the sign of α. The same situation can arise for the body-y axis. The following equation

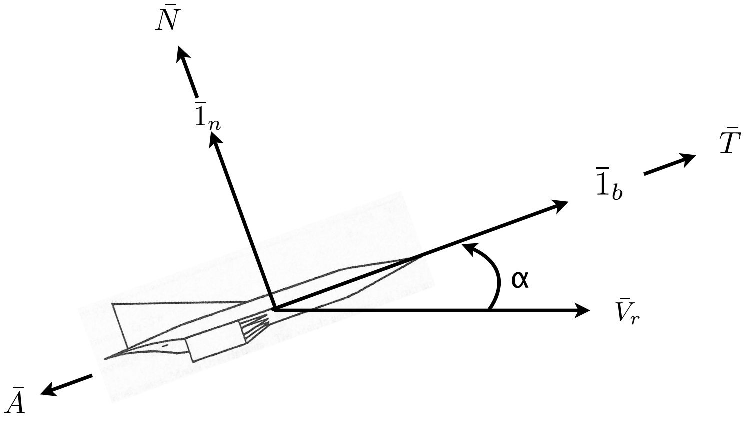

Figure 3.3 Vehicle Body Frame with Relative Velocity

for $\vec{\mathbf{1}}_y$ prevents an instantaneous 180-degree rotation

$$\vec{\mathbf{1}}_y = \vec{\mathbf{1}}_{V_r} \times \frac{\vec{\mathbf{1}}_b}{\sin\alpha}. \tag{3.17}$$

3.2 Equations of motion

The equations of motion for a vehicle in an inertial coordinate system are given as

$$\begin{aligned} \dot{\vec{\mathbf{r}}} &= \vec{\mathbf{V}} && (3.18) \\ \dot{\vec{\mathbf{V}}} &= \vec{\mathbf{g}}(\vec{\mathbf{r}}) + \frac{T\vec{\mathbf{1}}_b}{m(t)} + \frac{\vec{\mathbf{A}}}{m(t)} + \frac{\vec{\mathbf{N}}}{m(t)} && (3.19) \\ \dot{m} &= -\frac{T}{G_0 \mathrm{I}_{sp}} && (3.20) \end{aligned}$$

where $\vec{\mathbf{r}}$ and $\vec{\mathbf{V}} \in R^3$ are inertial position and velocity vectors, $\vec{\mathbf{g}}$ is acceleration due to gravity, T is vehicle thrust, $\vec{\mathbf{1}}_b$ is the unit vector defining the vehicles body axis, $\vec{\mathbf{A}}$ and $\vec{\mathbf{N}}$ are the aerodynamics forces along the body longitudinal and normal direction, respectively, $m(t)$ is the mass of the vehicle at time t, G_0 is is the gravitational acceleration magnitude at the surface of the Earth, and I_{sp} is the specific impulse of the engine.

The aerodynamic forces can be found using

$$A = \frac{1}{2}\rho V_r^2 S_{\text{ref}} C_A(Ma, \alpha) \tag{3.21}$$

$$N = \frac{1}{2}\rho V_r^2 S_{\text{ref}} C_N(Ma, \alpha) \tag{3.22}$$

where ρ is atmospheric density, and S_{ref} is the vehicle's reference area. C_A, C_N are the axial force coefficient and normal force coefficient, respectively, which are functions of Mach number, M_a, and angle-of-attack, α. Thrust can be generalized by

$$T = f(\mathrm{I}_{sp}, \phi_t, \alpha, M_a, \vec{\mathbf{x}}) \tag{3.23}$$

where ϕ_t is the engine throttle and $\vec{\mathbf{x}}$ is the state of the vehicle.

3.3 Non-dimensionalization

For better numerical conditioning, the equations of motion are nondimensionalized. Distance is normalized by R_0, the Earth's radius at the equator, time is normalized by $\sqrt{R_0/G_0}$, velocities are normalized by $\sqrt{R_0 G_0}$, and mass is normalized by m_0, the initial mass of the vehicle. The following are the normalized equations, where the prime denotes differentiation with respect to nondimensional time. Let all variable names remain the same as their dimensional counterpart.

$$\vec{\mathbf{r}}' = \vec{\mathbf{V}} \tag{3.24}$$

$$\vec{\mathbf{V}}' = -\frac{1}{r^3}\vec{\mathbf{r}} - A\vec{\mathbf{1}}_b + T\vec{\mathbf{1}}_b + N\vec{\mathbf{1}}_n \tag{3.25}$$

$$m' = -\sqrt{\frac{R_0}{G_0}}\frac{T \cdot m}{\mathrm{I}_{sp}} \tag{3.26}$$

where I_{sp} is dimenionsal. The thrust, T, and aerodynamic forces, A and N, are nondimensionalized and their magnitudes are in g's. A and N are given by the following equations,

$$\begin{aligned} A &= \frac{R_0}{2m_0m(t)}\rho(r)V_r^2 S_{\text{ref}} C_A(M_a, \alpha) && (3.27) \\ N &= \frac{R_0}{2m_0m(t)}\rho(r)V_r^2 S_{\text{ref}} C_N(M_a, \alpha) && (3.28) \end{aligned}$$

where ρ and S_{ref} remain dimensional. V_r is nondimensional relative velocity, given by

$$\vec{\mathbf{V}}_r = \vec{\mathbf{V}} - \vec{\omega}_E \times \vec{\mathbf{r}} - \vec{\mathbf{V}}_w \tag{3.29}$$

where $\vec{\omega}_E$ is the dimensionless angular rotation rate vector, and $\vec{\mathbf{V}}_w$ is the dimensionless wind velocity. The general formulation for non-dimenisonal thrust acceleration is given by

$$T = \frac{T_{\text{Dim}}}{m m_0 G_0} \tag{3.30}$$

where T_{Dim} is dimensional thrust given by Eq. (3.23). The equation would be specific to the engine model used.

CHAPTER 4. OPTIMAL CONTROL PROBLEM

The guidance problem for the Generic Hypersonic Vehicle (GHV) is to find the body-axis orientation, $\vec{\mathbf{1}}_b(t)$, for any given time. This determines the thrust direction and the aerodynamic forces during the atmospheric portion of the ascent. The engine throttle, ϕ_t, is a second control variable. However, for this research, ϕ_t is assumed to be given. The initial conditions, $\vec{\mathbf{r}}_0$ and $\vec{\mathbf{V}}_0$ are also assumed to be known. The final conditions (where $t = t_f$) will also be given, and can be written as k $(0 < k \leq 7)$ algebraic conditions

$$\vec{\boldsymbol{\Psi}}\left(\vec{\mathbf{r}}_f, \vec{\mathbf{V}}_f, m_f\right) = 0,\ \vec{\boldsymbol{\Psi}} \in R^k \tag{4.1}$$

where $\vec{\mathbf{r}}_f = \vec{\mathbf{r}}(t_f)$, $\vec{\mathbf{V}}_f = \vec{\mathbf{V}}(t_f)$, and $m_f = m(t_f)$.

4.1 Problem Formulation

4.1.1 Cost Function and Hamiltonian

In order to apply optimal control theory, a performance index is needed. For ascent trajectories, performance indices are typically chosen to minimized fuel consumption and thereby maximizing the payload. Denote the performance index by

$$J = \phi\left(\vec{\mathbf{r}}_f, \vec{\mathbf{V}}_f, m_f, t_f\right) \tag{4.2}$$

where only final weighting function, ϕ is used and no weight function, L, is used as in Eq. (2.2). For this research, the cost function is maximize final weight or

$$J = -m_f. \tag{4.3}$$

Using the equations of motion, the Hamiltonian function can be denoted as

$$H = \vec{\mathbf{P}}_r^T \vec{\mathbf{V}} + \vec{\mathbf{P}}_V^T \left[-\frac{1}{r^3}\vec{\mathbf{r}} + (T-A)\vec{\mathbf{1}}_b + N\vec{\mathbf{1}}_n \right] + P_m \left(-\sqrt{\frac{R_0}{G_0}} \frac{T \cdot m}{\text{Isp}} \right) \tag{4.4}$$

where $\vec{\mathbf{P}}_r$ and $\vec{\mathbf{P}}_V \in R^3$ are the costate vectors associated with the position and velocity states, and $P_m \in R$ is the costate scaler associate with mass. Unlike the rocket formulation in Ref. (26), the costate for mass is included. In the rocket formulation, the engine throttle was given, which is the same for the rocket. However, for rockets in general, mass rate is only a function of the throttle, therefore, the variation of mass is a prescribed function of time. In regards to the GHV, mass rate is a function of the throttle, the state of the vehicle, and α, thus a function $\vec{\mathbf{1}}_b$. Therefore it is included in the Hamiltonian function.

The necessary conditions for the optimal solution can be represented as (28)

$$\vec{\mathbf{P}}_r' = -\frac{\partial H}{\partial \vec{\mathbf{r}}} \tag{4.5}$$

$$\vec{\mathbf{P}}_V' = -\frac{\partial H}{\partial \vec{\mathbf{V}}} \tag{4.6}$$

$$P_m' = -\frac{\partial H}{\partial m} \tag{4.7}$$

$$0 = \frac{\partial H}{\partial \vec{\mathbf{1}}_b} \tag{4.8}$$

In addition to the terminal constraints given by Eq. (4.1), the optimal solution must meet the following transversality conditions

$$\vec{\mathbf{P}}_r(t_f) = -\frac{\partial \phi(\vec{\mathbf{r}}_f, \vec{\mathbf{V}}_f, m_f, t_f)}{\partial \vec{\mathbf{r}}_f} + \left(\frac{\partial \vec{\mathbf{\Psi}}}{\partial \vec{\mathbf{r}}_f} \right)^T \vec{\nu} \tag{4.9}$$

$$\vec{\mathbf{P}}_V(t_f) = -\frac{\partial \phi(\vec{\mathbf{r}}_f, \vec{\mathbf{V}}_f, m_f, t_f)}{\partial \vec{\mathbf{V}}_f} + \left(\frac{\partial \vec{\mathbf{\Psi}}}{\partial \vec{\mathbf{V}}_f} \right)^T \vec{\nu} \tag{4.10}$$

$$P_m(t_f) = -\frac{\partial \phi(\vec{\mathbf{r}}_f, \vec{\mathbf{V}}_f, m_f, t_f)}{\partial m_f} + \left(\frac{\partial \vec{\mathbf{\Psi}}}{\partial m_f} \right)^T \vec{\nu} \tag{4.11}$$

$$H\left(\vec{\mathbf{P}}_r, \vec{\mathbf{P}}_V, P_m, \vec{\mathbf{r}}^*, \vec{\mathbf{V}}^*, m^*, \vec{\mathbf{1}}_b^*, t \right)\Big|_{t_f} = \frac{\partial \phi}{\partial t_f} \tag{4.12}$$

where $\vec{\nu} \in R^k$ is a constant multiplier vector and the asterisk means the optimal values of the relevant variables. The final condition, Eq. (4.12), is used when the final time, t_f, is not specified. The first three transversality conditions can be combined to eliminate ν, leaving $7-k$ independent conditions involving only the final states, $\vec{\mathbf{x}}_f = \left(\vec{\mathbf{r}}_f^T \;\; \vec{\mathbf{V}}_f^T \;\; m_f\right)^T$ and costates, $\vec{\mathbf{P}}_f = \left(\vec{\mathbf{P}}_{r_f}^T \;\; \vec{\mathbf{P}}_{V_f}^T \;\; P_{m_f}\right)^T$.

4.1.2 Costate Equations

The costate equations can be derived from the first order necessary conditions given by Eqs. (4.5), (4.6), and (4.7).

$$\begin{aligned}
\vec{\mathbf{P}}_r' &= \frac{1}{r^3}\vec{\mathbf{P}}_v - \frac{3\left(\vec{\mathbf{P}}_V^T\vec{\mathbf{r}}\right)}{r^5}\vec{\mathbf{r}} - \vec{\mathbf{P}}_V^T\vec{\mathbf{1}}_b\left(\frac{\partial T}{\partial\vec{\mathbf{r}}} - \frac{\partial A}{\partial\vec{\mathbf{r}}}\right) - \vec{\mathbf{P}}_V^T\vec{\mathbf{1}}_n\left(\frac{\partial N}{\partial\vec{\mathbf{r}}}\right) - N\left(\frac{\partial\vec{\mathbf{1}}_n}{\partial\vec{\mathbf{r}}}\right)^T\vec{\mathbf{P}}_V \\
&\quad + m\sqrt{\frac{R_0}{G_0}}P_m\left[\frac{\partial T}{\partial\vec{\mathbf{r}}}\frac{1}{\mathrm{I}_{sp}} + T\frac{\partial}{\partial\vec{\mathbf{r}}}\left(\mathrm{I}_{sp}^{-1}\right)\right] \qquad (4.13) \\
\vec{\mathbf{P}}_v' &= -\vec{\mathbf{P}}_r - \vec{\mathbf{P}}_V^T\vec{\mathbf{1}}_b\left(\frac{\partial T}{\partial\vec{\mathbf{V}}} - \frac{\partial A}{\partial\vec{\mathbf{V}}}\right) - \vec{\mathbf{P}}_V^T\vec{\mathbf{1}}_n\frac{\partial N}{\partial\vec{\mathbf{V}}} - N\left(\frac{\partial\vec{\mathbf{1}}_n}{\partial\vec{\mathbf{V}}}\right)^T\vec{\mathbf{P}}_v \\
&\quad + P_m\sqrt{\frac{R_0}{G_0}}m\left[\frac{\partial T}{\partial\vec{\mathbf{V}}}\frac{1}{\mathrm{I}_{sp}} + T\frac{\partial}{\partial\vec{\mathbf{V}}}\left(\mathrm{I}_{sp}^{-1}\right)\right] \qquad (4.14) \\
P_m' &= -\vec{\mathbf{P}}_V^T\vec{\mathbf{1}}_b\left(\frac{\partial T}{\partial m} - \frac{\partial A}{\partial m}\right) - \vec{\mathbf{P}}_V^T\vec{\mathbf{1}}_n\frac{\partial N}{\partial m} + P_m\sqrt{\frac{R_0}{G_0}}\left(\mathrm{I}_{sp}^{-1}\right)\cdot\left(m\frac{\partial T}{\partial m} + T\right) \qquad (4.15)
\end{aligned}$$

These equations are similar to the costate equations in the rocket problem formulation(26), however, since mass rate is included in the Hamiltonian, those terms are present in the costate equations for position and velocity. Additionally, an extra costate equation is present, Eq. (4.15). The deviation in Eqs. (4.13) and (4.14) from the rocket costates come from the evaluation of $\partial T/\partial\vec{\mathbf{r}}$ and $\partial T/\partial\vec{\mathbf{V}}$. The dependency of thrust on the state of the vehicle require those terms in the GHV formulation, whereas, in the rocket formulation, the dependence on position is due to thrust loss from back pressure and there is no dependency on velocity.

Using the following relationships

$$\begin{aligned}
\frac{\partial \rho}{\partial \vec{\mathbf{r}}} &= \frac{\partial \rho}{\partial r}\frac{\vec{\mathbf{r}}}{r} && (4.16)\\
\frac{\partial V_r^2}{\partial \vec{\mathbf{r}}} &= 2\vec{\omega}_E \times \vec{\mathbf{V}}_r \Rightarrow \frac{\partial V_r}{\partial \vec{\mathbf{r}}} = \frac{1}{V_r}(\vec{\omega}_E \times \vec{\mathbf{V}}_r) && (4.17)\\
\frac{\partial \alpha}{\partial \vec{\mathbf{r}}} &= \vec{\omega}_E \times \frac{\partial \alpha}{\partial \vec{\mathbf{V}}} && (4.18)\\
\frac{\partial \alpha}{\partial \vec{\mathbf{V}}} &= \frac{1}{V_r \sin\alpha}(\vec{\mathbf{1}}_{V_r}\cos\alpha - \vec{\mathbf{1}}_b) && (4.19)
\end{aligned}$$

the following expansions can be determined for $\partial A/\partial \vec{\mathbf{r}}$ and $\partial N/\partial \vec{\mathbf{r}}$

$$\begin{aligned}
\frac{\partial A}{\partial \vec{\mathbf{r}}} &= \frac{R_0}{2m_0 m}\mathrm{S}_{\mathrm{ref}}\Bigg[V_r^2 C_A \frac{\partial \rho}{\partial r}\frac{\vec{\mathbf{r}}}{r} + 2\rho C_A\left(\vec{\omega}_E \times \vec{\mathbf{V}}_r\right)\\
&\qquad + \rho V_r\left(\frac{\partial C_A}{\partial M_a}\frac{\partial M_a}{\partial V_r}\frac{\partial V_r}{\partial \vec{\mathbf{r}}} + \frac{\partial C_A}{\partial M_a}\frac{\partial M_a}{\partial V_s}\frac{\partial V_s}{\partial \vec{\mathbf{r}}} + \frac{\partial C_A}{\partial \alpha}\frac{\partial \alpha}{\partial \vec{\mathbf{r}}}\right)\Bigg] && (4.20)\\
&= \frac{R_0}{2m_0 m}S_{\mathrm{ref}}\Bigg[\left(V_r^2 C_A\frac{\partial \rho}{\partial r} - \rho V_r M_a^2 \frac{\partial C_A}{\partial M_a}\frac{\partial V_s}{\partial r}\right)\frac{\vec{\mathbf{r}}}{r}\\
&\qquad + \left(2\rho C_A + \rho M_a \frac{\partial C_A}{\partial M_a}\right)\left(\vec{\omega}_E \times \vec{\mathbf{V}}_r\right) + \rho V_r^2 \frac{\partial C_A}{\partial \alpha}\left(\vec{\omega}_E \times \frac{\partial \alpha}{\partial \vec{\mathbf{V}}}\right)\Bigg] && (4.21)
\end{aligned}$$

$$\begin{aligned}
\frac{\partial N}{\partial \vec{\mathbf{r}}} &= \frac{R_0}{2m_0 m}\mathrm{S}_{\mathrm{ref}}\Bigg[V_r^2 C_N \frac{\partial \rho}{\partial r}\frac{\vec{\mathbf{r}}}{r} + 2\rho C_N\left(\vec{\omega}_E \times \vec{\mathbf{V}}_r\right)\\
&\qquad + \rho V_r\left(\frac{\partial C_N}{\partial M_a}\frac{\partial M_a}{\partial V_r}\frac{\partial V_r}{\partial \vec{\mathbf{r}}} + \frac{\partial C_N}{\partial M_a}\frac{\partial M_a}{\partial V_s}\frac{\partial V_s}{\partial \vec{\mathbf{r}}} + \frac{\partial C_N}{\partial \alpha}\frac{\partial \alpha}{\partial \vec{\mathbf{r}}}\right)\Bigg] && (4.22)\\
&= \frac{R_0}{2m_0 m}S_{\mathrm{ref}}\Bigg[\left(V_r^2 C_N\frac{\partial \rho}{\partial r} - \rho V_r M_a^2 \frac{\partial C_N}{\partial M_a}\frac{\partial V_s}{\partial r}\right)\frac{\vec{\mathbf{r}}}{r}\\
&\qquad + \left(2\rho C_N + \rho M_a \frac{\partial C_N}{\partial M_a}\right)\left(\vec{\omega}_E \times \vec{\mathbf{V}}_r\right) + \rho V_r^2 \frac{\partial C_N}{\partial \alpha}\left(\vec{\omega}_E \times \frac{\partial \alpha}{\partial \vec{\mathbf{V}}}\right)\Bigg] && (4.23)
\end{aligned}$$

where $V_s(r)$ is nondimensional speed of sound. The following are the expansions for $\partial A/\partial \vec{\mathbf{V}}$ and $\partial N/\partial \vec{\mathbf{V}}$

$$\begin{aligned}
\frac{\partial A}{\partial \vec{\mathbf{V}}} &= \frac{R_0}{2m_0 m}\rho S_{\mathrm{ref}}\left[\left(2V_r\frac{\partial V_r}{\partial \vec{\mathbf{V}}}\right)C_A + V_r^2\left(\frac{\partial C_A}{\partial \alpha}\frac{\partial \alpha}{\partial \vec{\mathbf{V}}} + \frac{\partial C_A}{\partial M_a}\frac{\partial M_a}{\partial V_r}\frac{\partial V_r}{\partial \vec{\mathbf{V}}}\right)\right] && (4.24)\\
&= \frac{R_0}{m_0 m}\rho S_{\mathrm{ref}}\left[\left(C_A + \frac{1}{2}M_a\frac{\partial C_A}{\partial M_a}\right)\vec{\mathbf{V}}_r + \frac{1}{2}V_r^2\frac{\partial C_A}{\partial \alpha}\frac{\partial \alpha}{\partial \vec{\mathbf{V}}}\right] && (4.25)
\end{aligned}$$

$$\begin{aligned} \frac{\partial N}{\partial \vec{\mathbf{V}}} &= \frac{R_0}{2m_0 m}\rho S_{\text{ref}} \left[\left(2V_r \frac{\partial V_r}{\partial \vec{\mathbf{V}}} \right) C_N + V_r^2 \left(\frac{\partial C_N}{\partial \alpha}\frac{\partial \alpha}{\partial \vec{\mathbf{V}}} + \frac{\partial C_N}{\partial M_a}\frac{\partial M_a}{\partial V_r}\frac{\partial V_r}{\partial \vec{\mathbf{V}}} \right) \right] \quad (4.26) \\ &= \frac{R_0}{m_0 m}\rho S_{\text{ref}} \left[\left(C_N + \frac{1}{2}M_a \frac{\partial C_N}{\partial M_a} \right) \vec{\mathbf{V}}_r + \frac{1}{2}V_r^2 \frac{\partial C_N}{\partial \alpha}\frac{\partial \alpha}{\partial \vec{\mathbf{V}}} \right]. \quad (4.27) \end{aligned}$$

The following are the expansions for $\partial A/\partial m$ and $\partial N/\partial m$

$$\begin{aligned} \frac{\partial A}{\partial m} &= \frac{R_0}{2m_0}\rho V_r^2 S_{\text{ref}} C_A \left(-\frac{1}{m^2} \right) \quad (4.28) \\ \frac{\partial N}{\partial m} &= \frac{R_0}{2m_0}\rho V_r^2 S_{\text{ref}} C_N \left(-\frac{1}{m^2} \right). \quad (4.29) \end{aligned}$$

In the costate equations, Eqs. (4.13) to (4.15), the terms associated with the differential of $\vec{\mathbf{1}}_n$ with respect to position and velocity can be shown to be zero. When $\alpha > 0$, use Eq. (3.14) to get

$$\begin{aligned} \left(\frac{\partial \vec{\mathbf{1}}_n}{\partial \vec{\mathbf{V}}} \right) &= \frac{1}{||\vec{\mathbf{1}}_b \times \vec{\mathbf{V}}_r||}(\vec{\mathbf{1}}_b \vec{\mathbf{1}}_b^T - I_{3\times3}) - \frac{(\vec{\mathbf{1}}_b \vec{\mathbf{V}}_r)\vec{\mathbf{1}}_b - \vec{\mathbf{V}}_r}{||\vec{\mathbf{1}}_b \times \vec{\mathbf{V}}_r||^2} \left(\frac{\partial ||\vec{\mathbf{1}}_b \times \vec{\mathbf{V}}_r||}{\partial \vec{\mathbf{V}}} \right)^T \\ &= \frac{1}{||\vec{\mathbf{1}}_b \times \vec{\mathbf{V}}_r||}(\vec{\mathbf{1}}_b \vec{\mathbf{1}}_b^T - I_{3\times3}) - \frac{\vec{\mathbf{1}}_n}{||\vec{\mathbf{1}}_b \times \vec{\mathbf{V}}_r||} \frac{(\vec{\mathbf{1}}_b \times (\vec{\mathbf{V}}_r \times \vec{\mathbf{1}}_b))^T}{||\vec{\mathbf{1}}_b \times \vec{\mathbf{V}}_r||} \\ &= \frac{1}{||\vec{\mathbf{1}}_b \times \vec{\mathbf{V}}_r||}(\vec{\mathbf{1}}_b \vec{\mathbf{1}}_b^T + \vec{\mathbf{1}}_n \vec{\mathbf{1}}_n^T - I_{3\times3}) \\ &= \frac{1}{V_r \sin\alpha}(\vec{\mathbf{1}}_b \vec{\mathbf{1}}_b^T + \vec{\mathbf{1}}_n \vec{\mathbf{1}}_n^T - I_{3\times3}) \quad (4.30) \end{aligned}$$

$$\begin{aligned} \left(\frac{\partial \vec{\mathbf{1}}_n}{\partial r} \right) &= \frac{1}{||\vec{\mathbf{1}}_b \times \vec{\mathbf{V}}_r||} \left\{ \vec{\mathbf{1}}_b \left[(-\tilde{\omega}_E)^T \vec{\mathbf{1}}_b \right]^T + \tilde{\omega}_E \right\} - \frac{(\vec{\mathbf{1}}_b^T \vec{\mathbf{V}}_r)\vec{\mathbf{1}}_b - \vec{\mathbf{V}}_r}{||\vec{\mathbf{1}}_b \times \vec{\mathbf{V}}_r||^2} \left(\frac{\partial ||\vec{\mathbf{1}}_b \times \vec{\mathbf{V}}_r||}{\partial \vec{\mathbf{r}}} \right)^T \\ &= \frac{1}{V_r \sin\alpha} \left[\vec{\mathbf{1}}_b (\vec{\omega}_E \times \vec{\mathbf{1}}_b)^T \vec{\mathbf{1}}_n (\vec{\omega} \times \vec{\mathbf{1}}_n)^T + \tilde{\omega}_E \right] \quad (4.31) \end{aligned}$$

where $\tilde{\omega}_E = -\partial \vec{\mathbf{V}}_r / \partial \vec{\mathbf{r}}$ is the skew symmetric matrix formed by $\vec{\omega}_E$ and $I_{3\times3}$ is a 3×3 identity matrix. When $\alpha < 0$ and using Eq. (3.16) results in the terms

$$\begin{aligned} \left(\frac{\partial \vec{\mathbf{1}}_n}{\partial \vec{\mathbf{V}}} \right) &= -\frac{1}{||\vec{\mathbf{1}}_b \times \vec{\mathbf{V}}_r||}(\vec{\mathbf{1}}_b \vec{\mathbf{1}}_b^T + \vec{\mathbf{1}}_n \vec{\mathbf{1}}_n^T - I_{3\times3}) \\ &= \frac{1}{V_r \sin\alpha}(\vec{\mathbf{1}}_b \vec{\mathbf{1}}_b^T + \vec{\mathbf{1}}_n \vec{\mathbf{1}}_n^T - I_{3\times3}) \quad (4.32) \end{aligned}$$

$$\left(\frac{\partial \vec{\mathbf{1}}_n}{\partial \vec{\mathbf{r}}}\right) = \frac{1}{V_r \sin\alpha}\left[\vec{\mathbf{1}}_b(\vec{\omega}_E \times \vec{\mathbf{1}}_b)^T \vec{\mathbf{1}}_n(\vec{\omega}_E \times \vec{\mathbf{1}}_n)^T + \tilde{\omega}_E\right]. \tag{4.33}$$

Using the following

$$\begin{aligned}
\vec{\omega}_E \times \vec{\mathbf{1}}_b &= \tilde{\omega}_E \vec{\mathbf{1}}_b && (4.34)\\
\tilde{\omega}_E^T &= -\tilde{\omega}_E && (4.35)\\
\vec{\mathbf{1}}_b(\vec{\omega}_E \times \vec{\mathbf{1}}_b)^T &= \vec{\mathbf{1}}_b(\tilde{\omega}_E \vec{\mathbf{1}}_b)^T = \vec{\mathbf{1}}_b \vec{\mathbf{1}}_b^T \tilde{\omega}_E^T && (4.36)\\
\vec{\mathbf{1}}_n(\vec{\omega}_E \times \vec{\mathbf{1}}_n)^T &= \vec{\mathbf{1}}_n \vec{\mathbf{1}}_n^T \tilde{\omega}_E^T && (4.37)
\end{aligned}$$

the term associated with the differential of $\vec{\mathbf{1}}_n$ with respect to position, $\partial\vec{\mathbf{1}}_n/\partial\vec{\mathbf{r}}$ then becomes

$$\begin{aligned}
\left(\frac{\partial \vec{\mathbf{1}}_n}{\partial \vec{\mathbf{r}}}\right)^T \vec{\mathbf{P}}_V &= \frac{1}{V_r \sin\alpha}\left[\vec{\mathbf{1}}_b(\vec{\omega}_E \times \vec{\mathbf{1}}_b)^T + \vec{\mathbf{1}}_n(\vec{\omega}_E \times \vec{\mathbf{1}}_n)^T + \tilde{\omega}_E\right]^T \vec{\mathbf{P}}_V\\
&= \frac{1}{V_r \sin\alpha}\tilde{\omega}_E[\vec{\mathbf{1}}_b\vec{\mathbf{1}}_b^T + \vec{\mathbf{1}}_n\vec{\mathbf{1}}_n^T - I_{3\times3}]\vec{\mathbf{P}}_V && (4.38)
\end{aligned}$$

The bracketed term in the above equation can then be show to be zero

$$\begin{aligned}
[\vec{\mathbf{1}}_b\vec{\mathbf{1}}_b^T + \vec{\mathbf{1}}_n\vec{\mathbf{1}}_n^T - I_{3\times3}]\vec{\mathbf{P}}_V &= (\vec{\mathbf{1}}_b\vec{\mathbf{P}}_V)\vec{\mathbf{1}}_b + (\vec{\mathbf{1}}_n\vec{\mathbf{P}}_V)\vec{\mathbf{1}}_n - \vec{\mathbf{P}}_V\\
&= P_V\cos(\Phi-\alpha)\vec{\mathbf{1}}_b + P_V\sin(\Phi-\alpha)\vec{\mathbf{1}}_n - \vec{\mathbf{P}}_V\\
&= 0. && (4.39)
\end{aligned}$$

This simplification is a result of $\vec{\mathbf{1}}_b$, $\vec{\mathbf{1}}_n$, and $\vec{\mathbf{P}}_V$ being contained in the same plane in the optimal solution and that the unit vectors, $\vec{\mathbf{1}}_b$ and $\vec{\mathbf{1}}_n$ being orthogonal to each other. See Section 4.1.3 for details.

The differentiation of thrust with respect to the states, $\partial T/\partial\vec{\mathbf{r}}$, $\partial T/\partial\vec{\mathbf{V}}$, and $\partial T/\partial m$, are dependent on the engine model used. In Chapter 5, the engine model is presented and those terms are given. The expanded costate equations, Eqs. (4.13) to (4.15), are given in detail in Appendix B.

4.1.3 Optimality Condition

The final necessary condition, Eq. (4.8), is used to determine the optimal control. In carrying out the differentiation, it must be noted that the aerodynamic forces, A and N, and the thrust, T, are functions of $\vec{\mathbf{1}}_b$ through their dependence on α. To evaluate the differential, the following relationships are established,

$$\begin{aligned} \frac{\partial \alpha}{\partial \vec{\mathbf{1}}_b} &= \frac{\cos\alpha}{\sin\alpha}\vec{\mathbf{1}}_b - \frac{1}{\sin\alpha}\vec{\mathbf{1}}_{V_r} && (4.40)\\ \frac{\partial \vec{\mathbf{1}}_n}{\partial \vec{\mathbf{1}}_b} &= \frac{1}{||\vec{\mathbf{1}}_b \times \vec{\mathbf{1}}_{V_r}||}\left[\left(\vec{\mathbf{1}}_b^T\vec{\mathbf{1}}_{V_r}\right)\mathrm{I}_{3\times 3} + \vec{\mathbf{1}}_b\vec{\mathbf{1}}_{V_r}^T\right] \\ &+\frac{1}{||\vec{\mathbf{1}}_b \times \vec{\mathbf{1}}_{V_r}||^3}\left[\left(\vec{\mathbf{1}}_b^T\vec{\mathbf{1}}_{V_r}\right)\vec{\mathbf{1}}_b - \vec{\mathbf{1}}_{V_r}\right]\left[\left(\vec{\mathbf{1}}_b\vec{\mathbf{1}}_{V_r}^T\right)\vec{\mathbf{1}}_{V_r} - \vec{\mathbf{1}}_b\right]^T. && (4.41) \end{aligned}$$

Define the following

$$\begin{aligned} s &= ||\vec{\mathbf{1}}_b \times \vec{\mathbf{1}}_{V_r}|| && (4.42)\\ a &= \left[\left(\vec{\mathbf{1}}_{V_r}^T\vec{\mathbf{1}}_b\right)\left(\vec{\mathbf{P}}_V^T\vec{\mathbf{1}}_b\right) - \left(\vec{\mathbf{P}}_V^T\vec{\mathbf{1}}_{V_r}\right)\right] && (4.43)\\ b &= \left[-\left(\vec{\mathbf{P}}_V^T\vec{\mathbf{1}}_b\right)\frac{\partial A}{\partial \alpha} + \frac{\partial N}{\partial \alpha}\left(\vec{\mathbf{P}}_V^T\vec{\mathbf{1}}_n\right)\right] && (4.44)\\ c &= \left[\vec{\mathbf{P}}_V^T\vec{\mathbf{1}}_b - P_m\sqrt{\frac{R_0}{G_0}\frac{m}{\mathrm{I}_{sp}}}\right]\frac{\partial T}{\partial \alpha}. && (4.45) \end{aligned}$$

The differential, Eq. (4.8), is evaluated and like terms are collected giving the following optimal control vector

$$\begin{aligned} \vec{\mathbf{1}}_b^* &= -\frac{1}{\frac{b+c}{\tan\alpha} - \frac{aN}{s^3}}\left\{\left[T - A + \frac{N}{s}\left(\vec{\mathbf{1}}_b^T\vec{\mathbf{1}}_{V_r}\right)\right]\vec{\mathbf{P}}_V\right. \\ &+ \left.\left[\frac{N}{s}\left(\vec{\mathbf{P}}_V^T\vec{\mathbf{1}}_b\right) + \frac{aN}{s^3}\left(\vec{\mathbf{1}}_{V_r}^T\vec{\mathbf{1}}_b\right) - \frac{b+c}{\sin\alpha}\right]\vec{\mathbf{1}}_{V_r}\right\} \\ &\triangleq c_1\left(\vec{\mathbf{x}}, \vec{\mathbf{P}}, \vec{\mathbf{1}}_b^*\right)\vec{\mathbf{P}}_V + c_2\left(\vec{\mathbf{x}}, \vec{\mathbf{P}}, \vec{\mathbf{1}}_b^*\right)\vec{\mathbf{V}}_r && (4.46) \end{aligned}$$

where c_1 and c_2 are scalar functions of the state, $\vec{\mathbf{x}}$, costate, $\vec{\mathbf{P}}$, and the optimal control, $\vec{\mathbf{1}}_b^*$. When compared to the rocket formulation(26), the optimal control has an included term, c, resulting from thrust dependance on angle-of-attack. However, the same conclusion can be made, that the optimal control, $\vec{\mathbf{1}}_b^*$, lies in a plane formed by $\vec{\mathbf{P}}_V$ and $\vec{\mathbf{V}}_r$ and the search for the optimal body axis orientation can be reduced to a one-dimensional search in such a plane. Let

$$\cos\Phi = \vec{\mathbf{1}}_{P_V}^T \vec{\mathbf{1}}_{V_r} \tag{4.47}$$

where $\vec{\mathbf{1}}_{P_V}$ and $\vec{\mathbf{1}}_{V_r}$ are unit vectors in the direction of $\vec{\mathbf{P}}_V$ and $\vec{\mathbf{V}}_r$, respectively, and Φ is the angle between $\vec{\mathbf{P}}_V$ and $\vec{\mathbf{V}}_r$. Figure 4.1 illustrates the plane. The following relationships can be determined from the figure

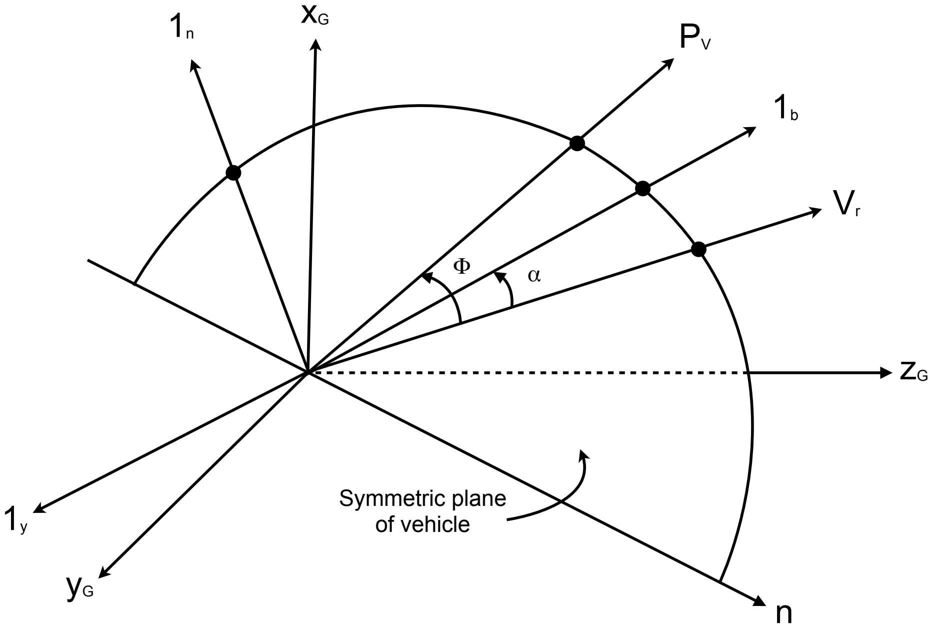

Figure 4.1 Body axes, $\vec{\mathbf{P}}_V$, and $\vec{\mathbf{V}}_r$ in Guidance System(26)

$$\vec{\mathbf{1}}_b^T \vec{\mathbf{P}}_V = P_v \cos(\Phi - \alpha) \tag{4.48}$$

$$\vec{\mathbf{1}}_n^T \vec{\mathbf{P}}_V = P_v \sin(\Phi - \alpha)\,. \tag{4.49}$$

These relationships allow the Hamiltonian to be rewritten as

$$\begin{aligned} H &= \vec{\mathbf{P}}_r^T\vec{\mathbf{V}} - \frac{1}{r^3}\vec{\mathbf{P}}_V^T\vec{\mathbf{r}} + (T-A)\,\vec{\mathbf{P}}_V^T\vec{\mathbf{1}}_b + N\vec{\mathbf{P}}_V^T\vec{\mathbf{1}}_n - P_m\frac{mT}{\mathrm{I}_{sp}}\sqrt{\frac{R_0}{G_0}} \\ &= \vec{\mathbf{P}}_r^T\vec{\mathbf{V}} - \frac{1}{r^3}\vec{\mathbf{P}}_V^T\vec{\mathbf{r}} + (T-A)\,P_v\cos\left(\Phi-\alpha\right) + NP_v\sin\left(\Phi-\alpha\right) \\ &\quad -P_m\frac{mT}{\mathrm{I}_{sp}}\sqrt{\frac{R_0}{G_0}} \end{aligned} \tag{4.50}$$

and the necessary condition can be rewritten as

$$\frac{\partial H}{\partial \alpha} = 0 \tag{4.51}$$

Evaluating the differential gives the following results

$$\begin{aligned} &\left(\frac{\partial T}{\partial \alpha} - \frac{\partial A}{\partial \alpha}\right) P_v\cos\left(\Phi-\alpha\right) + (T-A)\,P_v\sin\left(\Phi-\alpha\right) \\ &+\frac{\partial N}{\partial \alpha}P_v\sin\left(\Phi-\alpha\right) - NP_v\cos\left(\Phi-\alpha\right) - P_m\frac{m}{\mathrm{I}_{sp}}\sqrt{\frac{R_0}{G_0}}\frac{\partial T}{\partial \alpha} = 0. \end{aligned} \tag{4.52}$$

This equation is more complex than found in Ref. (26), but nevertheless, it is still a root finding problem. With known costate values and relative velocity, and given that A, N, T, $\partial A/\partial\alpha$, $\partial N/\partial\alpha$, and $\partial T/\partial\alpha$, are functions of angle-of-attack, the above equation can be solved numerically.

Once α is determined, $\vec{\mathbf{1}}_b^*$ can be determined from the following equation

$$\vec{\mathbf{1}}_b^* = \frac{\sin\alpha}{\sin\Phi}\vec{\mathbf{1}}_{P_V} + \frac{\sin(\Phi-\alpha)}{\sin\Phi}\vec{\mathbf{1}}_{V_r} \tag{4.53}$$

where the constants c_1 and c_2 in Eq. (4.46) are determined by taking the dot product of Eq. (4.46) with $\vec{\mathbf{1}}_{P_V}$ and $\vec{\mathbf{1}}_{V_r}$ and using the relationships from Eqs. (4.48) and (4.49).

4.1.4 Transversality Conditions

The end boundary conditions for the optimal control problem are given by the transversality conditions, Eqs. (4.9)-(4.11), and the final conditions given by Eq. (4.1). The additional constant vector, $\vec{\nu}$, can be eliminated using the transversality conditions.

In this research, the given final conditions for the guidance problem are final altitude (r_f^*), final velocity (V_f^*), final orbital inclination (i^*), and final flight path angle(γ_f^*). Note that in this formulation, γ_f^* does not have to be zero. For a fixed final time, these conditions can be written as functions of the states in the following way

$$\Psi_1 = \frac{1}{2}\vec{\mathbf{r}}_f^T\vec{\mathbf{r}}_f - \frac{1}{2}r_f^{*^2} = 0 \tag{4.54}$$

$$\Psi_2 = \frac{1}{2}\vec{\mathbf{V}}_f^T\vec{\mathbf{V}}_f - \frac{1}{2}V_f^{*^2} = 0 \tag{4.55}$$

$$\Psi_3 = \vec{\mathbf{1}}_N^T\left(\vec{\mathbf{r}}_f \times \vec{\mathbf{V}}_f\right) - \left|\left|\vec{\mathbf{r}}_f \times \vec{\mathbf{V}}_f\right|\right| \cos i^* = 0 \tag{4.56}$$

$$\Psi_4 = \vec{\mathbf{r}}_f^T\vec{\mathbf{V}}_f - r_f^* V_f^* \sin\gamma_f^* = 0 \tag{4.57}$$

where $\vec{\mathbf{1}}_N^T$ is the unit vector parallel to the polar axis of the Earth and pointing to the North. These equations give four of the seven required terminal constraints. Note the difference with the approach in Ref. (26), where final velocity is included as a terminal constraint, rather than iterated to determine the time of flight. Substituting the above equations and the final cost function, Eq. (4.3), into the transversality conditions gives

$$\vec{\mathbf{P}}_r(t_f) = \nu_1\vec{\mathbf{r}}_f + \nu_3\left[\vec{\mathbf{V}}_f \times \vec{\mathbf{1}}_n - \frac{\vec{\mathbf{V}}_f \times \vec{\mathbf{h}}_f}{\left|\left|\vec{\mathbf{r}}_f \times \vec{\mathbf{V}}_f\right|\right|}\cos i^*\right] + \nu_4\vec{\mathbf{V}}_f \tag{4.58}$$

$$\vec{\mathbf{P}}_V(t_f) = \nu_2\vec{\mathbf{V}}_f + \nu_3\left[\vec{\mathbf{1}}_n \times \vec{\mathbf{r}}_f - \frac{\vec{\mathbf{r}}_f \times \vec{\mathbf{h}}_f}{\left|\left|\vec{\mathbf{r}}_f \times \vec{\mathbf{V}}_f\right|\right|}\cos i^*\right] + \nu_4\vec{\mathbf{r}}_f \tag{4.59}$$

$$P_m(t_f) = 1 \tag{4.60}$$

In order to remove the constant vector $\vec{\nu}$, the following manipulations are done. The dot product of $\vec{\mathbf{r}}_f$ and Eq. (4.58) and (4.59) are combined with the dot product of $\vec{\mathbf{V}}_f$ and Eq. (4.58) and (4.59) to give Eq. (4.61). Next, the angular momentum vector, $\vec{\mathbf{h}}_f = \vec{\mathbf{r}}_f \times \vec{\mathbf{V}}_F$, is dotted with Eq. (4.58) and (4.59) and combined to give Eq. (4.62).

The final condition is the same as Eq. (4.60).

$$\begin{aligned}
\left(\vec{\mathbf{V}}_f^T\vec{\mathbf{V}}_f\right)\left(\vec{\mathbf{r}}_f^T\vec{\mathbf{P}}_{V_f}\right) - \left(\vec{\mathbf{r}}_f^T\vec{\mathbf{r}}_f\right)\left(\vec{\mathbf{V}}_f^T\vec{\mathbf{P}}_{r_f}\right) - \left(\vec{\mathbf{V}}_f^T\vec{\mathbf{r}}_f\right)\left[\vec{\mathbf{r}}_f^T\vec{\mathbf{P}}_{r_f} - \vec{\mathbf{V}}_f^T\vec{\mathbf{P}}_{V_f}\right] &= 0 \quad (4.61)\\
-\vec{\mathbf{h}}_f^T\vec{\mathbf{P}}_{r_f}\left[\vec{\mathbf{h}}_f^T\left(\vec{\mathbf{1}}_n \times \vec{\mathbf{r}}_f\right)\right] + \vec{\mathbf{h}}_f^T\vec{\mathbf{P}}_{V_f}\left[\vec{\mathbf{h}}_f^T\left(\vec{\mathbf{V}}_f \times \vec{\mathbf{1}}_n\right)\right] &= 0 \quad (4.62)\\
P_{m_f} - 1 &= 0 \quad (4.63)
\end{aligned}$$

Equations (4.54) to (4.57) combined with Eqs. (4.61) to (4.63) give the seven terminal boundary conditions.

4.1.5 Ascent Guidance Path Constraints

4.1.5.1 Dynamic Pressure Constraint

Dynamic pressure is a concern because in excess it can cause large structural loading as well as excessive heating on the vehicle. For these reasons, the dynamic pressure is regulated below a maximum value. Dynamic pressure is defined as

$$\bar{q} = \frac{1}{2}\rho V_r^2. \tag{4.64}$$

The constraint can be written as

$$S_1 = \bar{q} - \bar{q}_{\max} \leq 0. \tag{4.65}$$

Since S_1 is function of the state only, the derivative of S_1 is taken until an explicit function of both state and control is obtained. The derivative is given by

$$\dot{S}_1 = \frac{1}{2r}\frac{\partial\rho}{\partial r}V_r^2\vec{\mathbf{r}}^T\vec{\mathbf{V}} + \rho\vec{\mathbf{V}}_r^T\dot{\vec{\mathbf{V}}}_r \tag{4.66}$$

where

$$\dot{\vec{\mathbf{V}}}_r = \dot{\vec{\mathbf{V}}} - \vec{\omega}_E \times \vec{\mathbf{V}} - \dot{\vec{\mathbf{V}}}_W. \tag{4.67}$$

The dynamic pressure constraint is a first order constraint since the control, $\vec{\mathbf{1}}_b$, appears in the first derivative of the constraint (through $\dot{\vec{\mathbf{V}}}$, Eq. (3.25)).

The addition of the constraint to the optimal control problem modifies the costate equation to give

$$\dot{\vec{\mathbf{P}}} = -\frac{\partial H}{\partial \vec{\mathbf{X}}} - \lambda_q \frac{\partial \dot{S}_1}{\partial \vec{\mathbf{X}}} \tag{4.68}$$

where λ_q is a constant multiplier. When the constraint is not active (i.e. $S_1 < 0$), $\lambda_q = 0$ and the costate is determine as if no constraint is present. If the constraint is active for some finite time interval, $[t_1, t_2]$, then $S_2 = 0$, and λ_q satisfies the modified optimality condition

$$\frac{\partial H}{\partial \vec{\mathbf{1}}_b} + \lambda_q \frac{\partial \dot{S}_1}{\partial \vec{\mathbf{1}}_b} = 0. \tag{4.69}$$

Additionally, since the costate equation will be determined by two different conditions, the costate will have a jump at t_1

$$\vec{\mathbf{P}}(t_1^+) = \vec{\mathbf{P}}(t_1^-) + k \frac{\partial S_1}{\partial \vec{\mathbf{X}}} \tag{4.70}$$

where k is a constant multiplier. The second term in the modified optimality condition, Eq. (4.69), can be shown to be in the form

$$\frac{\partial \dot{S}_1}{\partial \vec{\mathbf{1}}_b} = d_1 \left(\vec{\mathbf{X}}, \vec{\mathbf{1}}_b \right) \vec{\mathbf{V}}_r + d_2 \left(\vec{\mathbf{X}}, \vec{\mathbf{1}}_b \right) \vec{\mathbf{1}}_b \tag{4.71}$$

where d_1 and d_2 are scalar functions of the state vector ($\vec{\mathbf{X}}$) and control vector ($\vec{\mathbf{1}}_b$). Equation (4.69) can then be used to show that the optimal control, $\vec{\mathbf{1}}_b^*$ lies in the plane of $\vec{\mathbf{P}}_v$ and $\vec{\mathbf{V}}_r$. As before, the modified optimality condition can be rewritten as

$$\frac{\partial H}{\partial \alpha} + \lambda_q \frac{\partial \dot{S}_1}{\partial \alpha} = 0. \tag{4.72}$$

Because $S_1 = 0$ during the specified time interval, this requires $\dot{S}_1 = 0$. Using this and Equation (4.72), the optimal solution can be found numerically.

However, the necessity for determining the time t_1 can pose an implementation issue. An accurate guess can lead to the solution process converging quickly, while a arbitrary guess can lead to slow convergence. To keep the guidance algorithm simple, the following implementation is used. It is known that the engine throttle is more effective in regulating the dynamic pressure by slowing down the increase in velocity. To throttle the engine, first, the optimal body axis ($\vec{\mathbf{1}}_b$) is determined where no constraint on the dynamic pressure is considered. Consider the time derivative of dynamic pressure at time t

$$\begin{aligned}
\dot{\bar{q}}(t) &= \frac{1}{2}V_r^2\frac{\partial\rho}{\partial r}\frac{\vec{\mathbf{r}}^T\vec{\mathbf{V}}}{r} + \rho\vec{\mathbf{V}}_r^T\dot{\vec{\mathbf{V}}} &\quad (4.73)\\
&\triangleq d_1 + d_2\eta(t) &\quad (4.74)\\
T_t &= \eta(t)T, \qquad 0 \le \eta(t) \le 1 &\quad (4.75)
\end{aligned}$$

where $\eta(t)$ is a scalar value to scale the thrust, T_t is the thrust produced by the engine, and d_1 and d_2 are scalar functions of state and and the optimal control, α^*. T in Eq. (4.75) can be defined differently depending on the engine model. If the engine is linearly dependant on throttle, than T is the portion of the thrust equation not a function of the throttle. However, if the engine model is a nonlinear function of throttle, then η scales the total thrust produce by the engine and T is the thrust produced assuming full throttle. The values for scalar functions can be shown to be

$$\begin{aligned}
d_1 &= \frac{1}{2}V_r^2\frac{\partial\rho}{\partial r}\frac{\vec{\mathbf{r}}^T\vec{\mathbf{V}}}{r} - \rho\left[\frac{\vec{\mathbf{r}}^T\vec{\mathbf{V}}_r}{r^3} + AV_r\cos\alpha + NV_r\sin\alpha\right] &\quad (4.76)\\
d_2 &= \rho V_r T\cos\alpha &\quad (4.77)
\end{aligned}$$

where $\dot{\vec{\mathbf{V}}}$ in Eq. (4.73) is found from Eq. (3.25) and T is replaced by T_t. Using the above equations, and by letting $\delta > 0$ be a small time increment, the first order approximation of dynamic pressure at time $t + \delta$ is given by

$$\begin{aligned}
\bar{q}(t+\delta) &\approx \bar{q}(t) + \dot{\bar{q}}(t)\delta &\quad (4.78)\\
&= \bar{q}(t) + [d_1 + d_2\eta(t)]\,\delta. &\quad (4.79)
\end{aligned}$$

An on-board guidance algorithm would determine the entire ascent trajectory ($\vec{\mathbf{X}}$) and the control vector ($\vec{\mathbf{1}}_b$) from the current condition to the targeted final condition for each guidance cycle. The attitude command used is the first data point in the guidance solution. The scalar value, η, throttles the engine linearly. This throttle command is determined at the current time t so that $\bar{q}(t+\delta) \leq \bar{q}_{\max}$. Using the first order approximation for dynamic pressure at time $t+\delta$ gives

$$\eta(t) \leq \frac{\bar{q}_{\max} - \bar{q}(t) - d_1\delta}{d_2\delta} \triangleq \eta_q. \tag{4.80}$$

In all likelihood, a minimum throttle setting, $\eta_{min} > 0$, will need to be observed. The command throttle η is given by

$$\eta = \begin{cases} \eta_q, & \text{if } \eta_{\min} \leq \eta_q \leq 1 \\ \eta_{\min}, & \text{if } \eta_q < \eta_{\min} \end{cases} . \tag{4.81}$$

An important thing to note is when the thrust is not a linear function of throttle. In this case, η is used to scale the thrust, T, to obtained a desired thrust, T_t. The dynamic pressure controller would need to implement a way of finding the throttle necessary to command the desired thrust. This could be done by using a root finding algorithm. The value of η would be determined by Eq. (4.81), which would determine T_t from Eq. (4.75). The thrust, T, is found from Eq. (3.23), and assumes full throttle. However, the root finding algorithm would find the throttle, ϕ_t, required to obtain the desired thrust, or

$$\phi_t = f^{-1}(T_t, \mathrm{I}_{sp}, \alpha, M_a, \vec{\mathbf{x}}). \tag{4.82}$$

4.1.5.2 Angle-of-Attack Constraint

The necessity to regulate angle-of-attack may be needed during the ascent of the vehicle. Two more constraints are used to bound α,

$$S_2 = \alpha - \alpha_{\max} \leq 0 \tag{4.83}$$

$$S_3 = -\alpha + \alpha_{\min} \leq 0. \tag{4.84}$$

Only the first constraint, Eq. (4.83), is discussed, since both equations are of similar form. Because the control appears explicitly in Eq. (4.83), the constraint is a zeroth-order constraint. The modified costate equation is given by

$$\dot{\vec{\mathbf{P}}} = -\frac{\partial H}{\partial \vec{\mathbf{X}}} - \lambda_\alpha \frac{\partial S_2}{\partial \vec{\mathbf{X}}}. \tag{4.85}$$

When S_2 is not active ($S_2 < 0$), then the multiplier $\lambda_\alpha = 0$ and the optimal control problem is treated as in the unconstrained case. When the constraint is active, $S_2 = 0$, then the constant multiplier needs to satisfy the new optimally condition

$$\frac{\partial H}{\partial \vec{\mathbf{1}}_b} + \lambda_\alpha \frac{\partial S_2}{\partial \vec{\mathbf{1}}_b} = 0. \tag{4.86}$$

Using Eq. (4.40) then

$$\frac{\partial S_2}{\partial \vec{\mathbf{1}}_b} = \frac{\partial \alpha}{\partial \vec{\mathbf{1}}_b} = \frac{\cos\alpha}{\sin\alpha}\vec{\mathbf{1}}_b - \frac{1}{\sin\alpha}\vec{\mathbf{1}}_{V_r}. \tag{4.87}$$

Using the above result and following the same steps as done previously, it can be shown that the optimal control, $\vec{\mathbf{1}}_b^*$, lies in the plane formed by $\vec{\mathbf{P}}_v$ and $\vec{\mathbf{V}}_r$. Because of this, the optimality condition can be rewritten

$$\frac{\partial H}{\partial \alpha} + \lambda_\alpha \frac{\partial S_2}{\partial \alpha} = 0. \tag{4.88}$$

Solving for λ_α gives

$$\lambda_\alpha = -\frac{\partial H/\partial \alpha}{\partial S_2/\partial \alpha} = -\frac{\partial H}{\partial \alpha} \tag{4.89}$$

where $\partial H/\partial \alpha$ is given by Eq. (4.52). In the time segement when $S_2 = 0$, the angle-of-attack is determined by the constraint

$$\alpha = \alpha_{\max}. \tag{4.90}$$

The control, $\vec{\mathbf{1}}_b$, is then determined as before (using Eq. (4.53)). The constant λ_α is then determined from Eq. (4.89) and used to calculate the costates.

CHAPTER 5. VEHICLE CHARACTERISTICS

The hypersonic vehicle model used was taken from White et al. (30). The Generic Hypersonic Aerodynamics Model Example (GHAME) represents a single stage to orbit vehicle that can take off horizontally from conventional runways, accelerate to orbital velocities, and either insert into low Earth orbit or return to Earth for horizontal landing.

The vehicle geometry is based off a cylinder 20 feet in diameter and 120 feet in length. Attached to the cylinder are two 10 ° half angle cones to represent the nose and the tail of the aircraft. Finally, the wing and tail are modeled as thin triangular plates. The referece area, S_{ref}, is 6000 ft^2, the reference cord, $\bar{c}$, is 75 ft, and the reference span, b, is 80 ft. The overall length of the vehicle is 234.4 ft. The vehicle is estimated to have a gross take off weight of 300,000 pounds. The configuration of the vehicle is shown in Figure 5.1.

5.1 GHAME Aerodynamic Data

The GHAME aerodynamic model is based loosely on empirical data. Included in the data were aerodynamic anomalies, coming from the space shuttle, lifting body type vehicles, a swept double-delta configuration vehicle, and 6 ° half-angle cones using modified Newtonian impact flow theory. Lift and drag, L and D respectively, for the GHAME model are given as

$$L = C_L \bar{q} S_{\text{ref}} \tag{5.1}$$

$$D = C_D \bar{q} S_{\text{ref}} \tag{5.2}$$

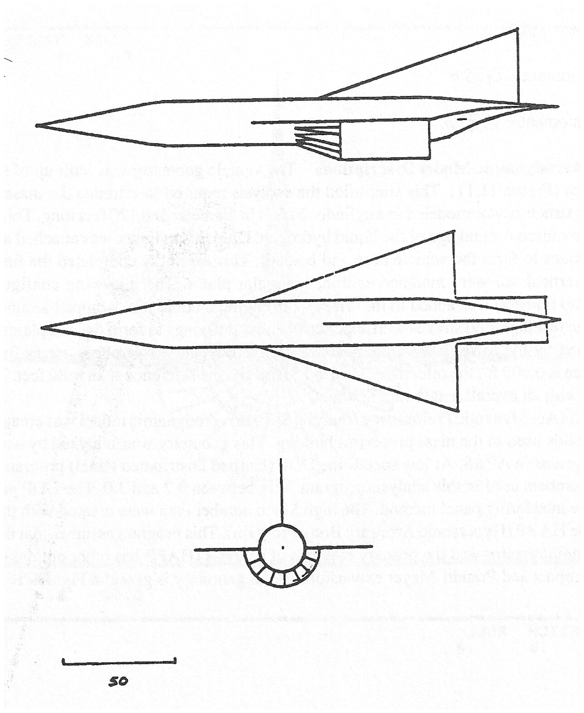

Figure 5.1 GHAME Aircraft Configuration (30)

where $\bar{q}$ is the dynamic pressure. The lift and drag coeffients, C_L and C_D respectively, are given by

$$C_L = C_{L_0}(M_a, \alpha) + C_{L_\alpha}(M_a, \alpha)\alpha + C_{L_{\delta e}}(M_a, \alpha)\delta e \tag{5.3}$$

$$C_D = C_{D_0}(M_a, \alpha) + C_{D_\alpha}(M_a, \alpha)\alpha \tag{5.4}$$

where α is angle of attack, M_a is Mach number, δe is the elevon deflection, and the other coefficients were determined by look up table, where the range for Mach is $0 < M_a < 24$, and for angle-of-attack is $-3^\circ < \alpha < 21^\circ$. The data tables for GHAME are provided in Appendix A. To increase computation efficiency, curve fits of the data were used. The curve fit equations are also provided in Appendix A. For this research, elevons were not used, i.e. $\delta e = 0$.

In the non-dimensional equations of motion (Eqs. (3.24) and (3.25)) both axial and normal force are needed, but the GHAME model provides lift and drag coefficients. Therefore, the following conversions are used to find the axial and normal force coefficient in Eqs. (3.27) and (3.28)

$$\begin{aligned} C_A &= -C_L \sin\alpha + C_D \cos\alpha & (5.5) \\ C_N &= C_D \cos\alpha + C_D \sin\alpha. & (5.6) \end{aligned}$$

5.2 GHAME Engine Model

The engine model was develop to represent the full flight envelope of the vehicle. For the range of flight of the GHAME vehicle, multiple engine cycles would be needed. This would include a turbojet cycle, ramjet cycle, and scramjet cycle. It was assumed that the engine would automatically change from one cycle to the next and that the engine had a variable inlet. The breakpoints for the cycles were: turbojet, $0 < M_a < 2$; ramjet, $2 < M_a < 6$; scramjet, $6 < M_a$.

The development of the engine model begins with the following thrust equation(31)

$$T = \dot{m} G_0 \mathrm{I}_{sp} \tag{5.7}$$

where I_{sp} is the specific impulse, $\dot{m}$ is the mass rate, and G_0 is the gravitational acceleration magnitude at the surface of the Earth. Assume the weight flow rate, $\dot{m}G_0$, to be the air that passes through the intake of the engine, with an area $A_c = 300\ ft^2$. The weight flow rate is then given

$$\dot{m}G_0 = G_0 \rho V_r A_c \tag{5.8}$$

where ρ is atmospheric density and V_r is Earth relative velocity. The above equation assumes that air enters the cowl uniformly. However, this is not true for scramjet engines, so the authors of GHAME introduced a capture-area coefficient, C_T. The coefficient depends on both angle-of-attack and Mach number, $C_T = f(\alpha, M_a)$. Then, the effective weight flow can be written as

$$\dot{m}G_0 = G_0 \rho V_r C_T(\alpha, M_a) A_c. \tag{5.9}$$

Fuel flow is handled by a throttle command, ϕ_t and varies from 0 to 2. The fuel/air ratio of the engine is adjusted to stoichiometric ratio, which is $0.029\phi_t$. Lastly, I_{sp} is a function of the throttle setting and Mach number. Combining all of the above into Eq. (5.7) results in the following thrust model

$$T = 0.029\phi_t \mathrm{I}_{sp}(M_a, \phi_t)\rho G_0 V_r C_T(\alpha, M_a) A_c. \tag{5.10}$$

The specific impulse, I_{sp}, and capture-area coefficient, C_T, are found using lookup tables. Again, in this research, a curve fit was used to represent both values. The data tables and curve fits are provided in Appendix A. An important note is that thrust for this vehicle, and air-breathing hypersonic vehicles in general, are functions of the state but this is not true for rockets. The thrust model from Eq. (5.10) was nondimensionalized for use in the optimal control formulation, giving

$$T = 0.029\sqrt{\frac{G_0}{R_0}}\phi_t \mathrm{I}_{sp}(M_a, \phi_t)\frac{R_0}{m_0 m(\tau)}\rho(r) V_r A_c C_T(\alpha, M_a) \tag{5.11}$$

where I_{sp}, ρ, and A_c remain dimensional, τ is nondimensional time, r is nondimensional position magnitude, R_0 is the Earth's radius at the equator, m is nondimensional mass, m_0 is the initial mass of the vehicle, and V_r is nondimensional Earth relative velocity magnitude.

5.3 Costate Equations Continued

The costate equation derivation in the previous chapter required the terms $\partial T/\partial \vec{\mathbf{r}}$, $\partial T/\partial \vec{\mathbf{V}}$, and $\partial T/\partial m$. Using Eq. (5.10) and the simplifications from Section 4.1.2, the following are the expanded terms

$$
\begin{aligned}
\frac{\partial T}{\partial \vec{\mathbf{r}}} &= \sqrt{\frac{G_0}{R_o}}(0.029\phi_t)\frac{R_0}{m_0 m}A_c \cdot \\
&\left[\rho V_r C_T \left(\frac{\partial \mathrm{I}_{sp}}{\partial M_a}\frac{\partial M_a}{\partial V_r}\frac{\partial V_r}{\partial \vec{\mathbf{r}}} + \frac{\partial \mathrm{I}_{sp}}{\partial M_a}\frac{\partial M_a}{\partial V_s}\frac{\partial V_s}{\partial \vec{\mathbf{r}}}\right) + \mathrm{I}_{sp}V_r C_T \frac{\partial \rho}{\partial \vec{\mathbf{r}}} + \rho C_T \mathrm{I}_{sp}\frac{\partial V_r}{\partial \vec{\mathbf{r}}}\right. \\
&\left. +\rho V_r \mathrm{I}_{sp}\left(\frac{\partial C_T}{\partial M_a}\frac{\partial M_a}{\partial V_r}\frac{\partial V_r}{\partial \vec{\mathbf{r}}} + \frac{\partial C_T}{\partial M_a}\frac{\partial M_a}{\partial V_s}\frac{\partial V_s}{\partial \vec{\mathbf{r}}} + \frac{\partial C_T}{\partial \alpha}\frac{\partial \alpha}{\partial \vec{\mathbf{r}}}\right)\right] \\
&= \left\{\sqrt{\frac{G_0}{R_0}}(0.029\phi_t)\frac{R_0}{m_0 m}A_c\right\} \cdot \\
&\left[\left(-\rho M_a^2 C_T \frac{\partial \mathrm{I}_{sp}}{\partial M_a}\frac{\partial V_s}{\partial r} + \mathrm{I}_{sp}V_r C_T \frac{\partial \rho}{\partial r} - \rho \mathrm{I}_{sp} M_a^2 \frac{\partial C_T}{\partial M_a}\frac{\partial V_s}{\partial r}\right)\frac{\vec{\mathbf{r}}}{r} + \rho \mathrm{I}_{sp} V_r \frac{\partial C_T}{\partial \alpha}\left(\vec{\omega}_E \times \frac{\partial \alpha}{\partial \vec{\mathbf{V}}}\right)\right. \\
&\left. + \left(\frac{\rho}{V_r}M_a C_T \frac{\partial \mathrm{I}_{sp}}{\partial M_a} + \frac{\rho}{V_r}\mathrm{I}_{sp}C_T + \frac{\rho}{V_s}\mathrm{I}_{sp}\frac{\partial C_T}{\partial M_a}\right)\left(\vec{\omega}_E \times \vec{\mathbf{V}}_r\right)\right] \qquad (5.12)
\end{aligned}
$$

$$
\begin{aligned}
\frac{\partial T}{\partial \vec{\mathbf{V}}} &= \sqrt{\frac{G_0}{R_0}}(0.029\phi_t)\rho\frac{R_0}{m_0 m}A_c \left[V_r C_T \frac{\partial \mathrm{I}_{sp}}{\partial M_a}\frac{\partial M_a}{\partial V_r}\frac{\partial V_r}{\partial \vec{\mathbf{V}}} + \mathrm{I}_{sp}C_T \frac{\vec{\mathbf{V}}_r}{V_r}\right. \\
&\left. +\mathrm{I}_{sp}V_r \left(\frac{\partial C_T}{\partial \alpha}\frac{\partial \alpha}{\partial \vec{\mathbf{V}}} + \frac{\partial C_T}{\partial M_a}\frac{\partial M_a}{\partial V_r}\frac{\partial V_r}{\partial \vec{\mathbf{V}}}\right)\right] \\
&= \sqrt{\frac{G_0}{R_0}}(0.029\phi_t)\rho\frac{R_0}{m_0 m}A_c \left[\left(M_a C_T \frac{\partial \mathrm{I}_{sp}}{\partial M_a} + \mathrm{I}_{sp}C_T + \mathrm{I}_{sp}M_a \frac{\partial C_T}{\partial M_a}\right)\frac{\vec{\mathbf{V}}_r}{V_r}\right. \\
&\left. +\mathrm{I}_{sp}V_r \frac{\partial C_T}{\partial \alpha}\frac{\partial \alpha}{\partial \vec{\mathbf{V}}}\right] \qquad (5.13)
\end{aligned}
$$

$$
\frac{\partial T}{\partial m} = 0.029\phi_t \sqrt{\frac{G_0}{R_0}}\mathrm{I}_{sp}\rho\frac{R_0}{m_0}V_r C_T A_c \left(-\frac{1}{m^2}\right) \qquad (5.14)
$$

where $\vec{\mathbf{r}}$ and $\vec{\mathbf{V}}$ are nondimensional position and velocity, respectively, $\vec{\mathbf{V}}_r$ is nondimensional Earth relative velocity, $\vec{\omega}_E$ is nondimensional Earth rotation rate vector, and V_s is nondimensional speed of sound.

CHAPTER 6. NUMERICAL METHOD

The optimal control problem can be summarized with the following equations

$$\text{Hamiltonian:} \quad H(x,u,P,t) \triangleq L(x,u,t) + P^T f(x,u,t) \tag{6.1}$$

$$\text{Dynamics:} \quad \dot{x} = f(x,u,t) = \left(\frac{\partial H}{\partial P}\right)^T \tag{6.2}$$

$$\text{Costate Equations:} \quad \dot{P} = -\left(\frac{\partial L}{\partial x}\right)^T - \left(\frac{\partial f}{\partial x}\right)^T P = -\left(\frac{\partial H}{\partial x}\right)^T \tag{6.3}$$

$$\text{Optimality Condition:} \quad \left(\frac{\partial H}{\partial u}\right)^T = \left(\frac{\partial L}{\partial u}\right)^T + \left(\frac{\partial f}{\partial u}\right)^T P = 0 \tag{6.4}$$

$$\text{Terminal Constraints:} \quad \phi_f(x_f, t_f) = 0 \tag{6.5}$$

$$\text{Path Constraints:} \quad S(x,u,t) \leq 0 \tag{6.6}$$

where H, the Hamiltonian, is a function of the states, x, the costates, P, the control, u, and time, t. The weighting function or performance index is denoted as L, and is a function of the state, control, and time. The terminal constraints, Eq. (6.5) are functions of final time, t_f, and the state at final time, $x_f = x(t_f)$. Finally, the path constraints, Eq. (6.6), are a function of the state, control, and time.

The solution to the above problem can be determined by restating the optimal control problem as a two point boundary value problem (TPBVP). First, substitute the optimal control determined from Eq. (6.4) into the state and costate equations, Eqs. (6.2) and (6.3). Let $\vec{\mathbf{y}} = (\vec{\mathbf{x}}^T\ \vec{\mathbf{P}}^T)^T \in R^{2n}$ with $n = 7$, then the complete TPBVP is given by

$$\frac{d\vec{\mathbf{y}}}{dt} = \vec{\mathbf{f}}(t, \vec{\mathbf{y}}) \tag{6.7}$$

$$\vec{\mathbf{B}}_0(\vec{\mathbf{y}}_0) = 0 \tag{6.8}$$

$$\vec{\mathbf{B}}_f(\vec{\mathbf{y}}_f) = 0 \tag{6.9}$$

where t is time, $\vec{\mathbf{B}}_0(\vec{\mathbf{y}}_0) = 0$ are the given initial conditions, and $\vec{\mathbf{B}}_f(\vec{\mathbf{y}}_f) = 0$ are the final conditions (Eq. (6.5)).

6.1 Finite Difference Method

A numerical solution to the TPBVP can be obtained using a finite difference method (32). Let t_f be a specified final time. As recommend by Keller(32) and Press(34), the first order ordinary differential equations (ODEs) in Eqs. (6.7) to (6.9) are replaced by approximate finite difference equations (FDEs) on a grid of points over the given time domain. Divide the time domain into M subintervals of equal length,

$$t_k = t_0 + kh, \qquad k = 0, 1, ..., M; \qquad h = \frac{t_f - t_0}{M} \tag{6.10}$$

where t_k is a given time node, t_0 is the initial time, and t_f is a specified final time. A central difference scheme is used to represent the differential, resulting in the FDE equivalent of Eq. (6.7)

$$\vec{\mathbf{y}}_k - \vec{\mathbf{y}}_{k-1} = h\vec{\mathbf{f}}\left(t_{k-1/2}, \frac{\vec{\mathbf{y}}_k - \vec{\mathbf{y}}_{k-1}}{2}\right), \qquad k = 1, 2, ..., M \tag{6.11}$$

where $\vec{\mathbf{y}}_k = \vec{\mathbf{y}}(t_0 + kh)$ is the value of the solution at node t_k. Rewriting Eq. (6.11) and the boundary conditions gives the following

$$\begin{aligned}
\vec{\mathbf{E}}_k &= \vec{\mathbf{y}}_k - \vec{\mathbf{y}}_{k-1} - h\vec{\mathbf{f}}\left(t_{k-1/2}, \frac{\vec{\mathbf{y}}_k - \vec{\mathbf{y}}_{k-1}}{2}\right) = 0 && (6.12)\\
\vec{\mathbf{E}}_0 &= \vec{\mathbf{B}}_0(\vec{\mathbf{y}}_0) = 0 && (6.13)\\
\vec{\mathbf{E}}_M &= \vec{\mathbf{B}}_f(\vec{\mathbf{y}}_f) = 0. && (6.14)
\end{aligned}$$

Let $\vec{\mathbf{Y}} = (\vec{\mathbf{y}}_0^T \;\; \vec{\mathbf{y}}_1^T \;\; \ldots \;\; \vec{\mathbf{y}}_M^T)^T \in R^{2n(M+1)}$ refer to the set of unknown variables. Equation (6.12) represents $2n$ equations for each node coupling $4n$ $(2 \times 2n)$ variables at nodes k and $k-1$. Also, Eq. (6.12) is valid on M points of the grid, giving $2nM$ equations for the $2n(M+1)$ variables. The boundary conditions, Eqs. (6.13) and (6.14), are the remaining $2n$ equations. Equations (6.12) to (6.14) can be summarized by

$$\vec{\mathbf{E}}(\vec{\mathbf{Y}}) = 0. \tag{6.15}$$

The problem is a root finding problem for a system of $2n(M+1)$ nonlinear algebraic equations. It has been shown that under certain conditions of smoothness and boundary conditions(32):

- Both the original TPBVP and the finite difference problem have a unique solution;
- The solution to the finite difference problem, $\vec{\mathbf{Y}}_k$, is a second-order approximation to the solution of the TPBVP at time t_k, $\vec{\mathbf{Y}}^*(t_k)$, i.e.,

$$||\vec{\mathbf{Y}}^*(t_k) - \vec{\mathbf{Y}}_k|| = O(h^2), \quad K = 0, 1, \ldots, M. \tag{6.16}$$

6.2 FDE Solution Algorithm

The Modified Newton Method has been show to work well in solving the FDE problem, Eq. (6.15) (33). The algorithm begins with an initial guess, $\vec{\mathbf{Y}}_{j,k}$, which are the values of the $2n$ variables, Y_j, at $M+1$ points t_k. The initial guess is adjusted by a value $\Delta\vec{\mathbf{Y}}_{j,k}$ so that the updated value, $\vec{\mathbf{Y}}_{j,k} + \Delta\vec{\mathbf{Y}}_{j,k}$, is a closer approximation to the solution. To determine the equation for the increments, the FDE's are expanded in first order Taylor series with respect to small changes, $\Delta\vec{\mathbf{Y}}_k$,

$$\begin{aligned}\vec{\mathbf{E}}_k(\vec{\mathbf{Y}}_k + \Delta\vec{\mathbf{Y}}_k, \vec{\mathbf{Y}}_{k-1} + \Delta\vec{\mathbf{Y}}_{k-1}) \approx \vec{\mathbf{E}}_k(\vec{\mathbf{Y}}_k, \vec{\mathbf{Y}}_{k-1}) +& \\ \sum_{n=1}^{2n} \frac{\partial \vec{\mathbf{E}}_k}{\partial Y_{n,k-1}} \Delta Y_{n,k-1} + \sum_{n=1}^{2n} \frac{\partial \vec{\mathbf{E}}_k}{\partial Y_{n,k}} \Delta Y_{n,k}.&\end{aligned} \tag{6.17}$$

The solution is found when Eq. (6.15) is met, (i.e. the updated value $\vec{\mathbf{E}}(\vec{\mathbf{Y}} + \Delta\vec{\mathbf{Y}})$ is zero). Let

$$S_{j,n} = \frac{\partial E_{j,k}}{\partial Y_{n,k-1}}, \quad S_{j,n+2N}\frac{\partial E_{j,k}}{\partial Y_{n,k}}, \quad n = 1, 2, \ldots, 2N \tag{6.18}$$

then the set of equations at an interior point can be written as

$$\sum_{n=1}^{2N} S_{j,n}\Delta Y_{n,k-1} + \sum_{n=2N+1}^{4N} S_{j,n}\Delta Y_{n-2N,k} = -E_{j,k}, \quad j = 1, 2, \ldots, 2N. \tag{6.19}$$

Additionally, the endpoints can be expanded in a first order Taylor series. With

$$S_{j,n} = \frac{\partial E_{j,1}}{\partial Y_{n,1}}, \quad n = 1, 2, \ldots, 2N \tag{6.20}$$

the first boundary can be expanded to

$$\sum_{n=1}^{2N} S_{j,n}\Delta Y_{n,1} = -E_{j,1}, \quad n = N+1, N+2, \ldots, 2N. \tag{6.21}$$

Similarly, with

$$S_{j,n} = \frac{\partial E_{j,M+1}}{\partial Y_{n,M}}, \quad n = 1, 2, \ldots, 2N \tag{6.22}$$

the second boundary can be written as

$$\sum_{n=1}^{2N} S_{j,n}\Delta Y_{n,M} = -E_{j,M+1}, \quad n = 1, 2, \ldots, N. \tag{6.23}$$

Equations (6.19), (6.21), and (6.23) represent a set of linear equations to be solved for the correction term $\Delta\vec{\mathbf{Y}}$, and are iterated until the corrections are sufficiently small. Because each $S_{j,n}$ couples only points k and $k-1$, these equations have a special structure. Figure 6.1 shows the structure for the case of five variables, four grid points, three initial boundary conditions, and two end conditions. The coefficients of the FDEs are represented by “x”, “V” represents a component of the unknown solution vector, “B” is a component of the known right-hand side, and the empty space represent zeros. This “block diagonal” structure allows the equations to be solved using a special form of

$$\begin{array}{cccccccccccccccccccccc}
x&x&x&x&x&&&&&&&&&&&&&&&&V&B\\
x&x&x&x&x&&&&&&&&&&&&&&&&V&B\\
x&x&x&x&x&&&&&&&&&&&&&&&&V&B\\
x&x&x&x&x&x&x&x&x&x&&&&&&&&&&&V&B\\
x&x&x&x&x&x&x&x&x&x&&&&&&&&&&&V&B\\
x&x&x&x&x&x&x&x&x&x&&&&&&&&&&&V&B\\
x&x&x&x&x&x&x&x&x&x&&&&&&&&&&&V&B\\
x&x&x&x&x&x&x&x&x&x&&&&&&&&&&&V&B\\
&&&&&x&x&x&x&x&x&x&x&x&x&&&&&&V&B\\
&&&&&x&x&x&x&x&x&x&x&x&x&&&&&&V&B\\
&&&&&x&x&x&x&x&x&x&x&x&x&&&&&&V&B\\
&&&&&x&x&x&x&x&x&x&x&x&x&&&&&&V&B\\
&&&&&x&x&x&x&x&x&x&x&x&x&&&&&&V&B\\
&&&&&&&&&&x&x&x&x&x&x&x&x&x&x&V&B\\
&&&&&&&&&&x&x&x&x&x&x&x&x&x&x&V&B\\
&&&&&&&&&&x&x&x&x&x&x&x&x&x&x&V&B\\
&&&&&&&&&&x&x&x&x&x&x&x&x&x&x&V&B\\
&&&&&&&&&&x&x&x&x&x&x&x&x&x&x&V&B\\
&&&&&&&&&&&&&&&x&x&x&x&x&V&B\\
&&&&&&&&&&&&&&&x&x&x&x&x&V&B
\end{array}$$

Figure 6.1 Matrix Structure of a Set of Linear FDEs

Gaussian elimination which minimizes the number of operations. Standard Gaussian elimination uses elementary operations to manipulate the algebraic linear equations to produce unity in the diagonal elements and zeros below the diagonal. The block structure of this problem allows the linear equations to be reduce more than the standard from. An added benefit of this structure is that it minimizes storage of matrix coefficients. Figure 6.2 represents the final from after the Gaussian elimination, which allows the solution to be determined by a back-substituting procedure.

The update to the solution is then given by

$$\vec{\mathbf{Y}}_j = \vec{\mathbf{Y}}_{j-1} + \sigma_j \Delta\vec{\mathbf{Y}}_j, \quad 0 < \sigma_j \leq 1 \tag{6.24}$$

where j denotes the j-th iteration, and the step size parameter, σ, begins with a value of 1 and is halved until the following condition is met

$$\sigma_j = \max_{0\leq i}\left\{\frac{1}{2^i}\middle|\vec{\mathbf{E}}^T\left[\vec{\mathbf{Y}}_{j-1} + \frac{\Delta\vec{\mathbf{Y}}_j}{2^i}\right]\vec{\mathbf{E}}\left[\vec{\mathbf{Y}}_{j-1} + \frac{\Delta\vec{\mathbf{Y}}_j}{2^i}\right] < \vec{\mathbf{E}}^T(\vec{\mathbf{Y}}_{j-1})\vec{\mathbf{E}}(\vec{\mathbf{Y}}_{j-1})\right\}. \tag{6.25}$$

$$\begin{array}{cccccccccccccccccccccc}
1&&&x&x&&&&&&&&&&&&&&&&V&B \\
&1&&x&x&&&&&&&&&&&&&&&&V&B \\
&&1&x&x&&&&&&&&&&&&&&&&V&B \\
&&&1&&&&&x&x&&&&&&&&&&&V&B \\
&&&&1&&&&x&x&&&&&&&&&&&V&B \\
&&&&&1&&&x&x&&&&&&&&&&&V&B \\
&&&&&&1&&x&x&&&&&&&&&&&V&B \\
&&&&&&&1&x&x&&&&&&&&&&&V&B \\
&&&&&&&&1&&&&&x&x&&&&&&V&B \\
&&&&&&&&&1&&&&x&x&&&&&&V&B \\
&&&&&&&&&&1&&&x&x&&&&&&V&B \\
&&&&&&&&&&&1&&x&x&&&&&&V&B \\
&&&&&&&&&&&&1&x&x&&&&&&V&B \\
&&&&&&&&&&&&&1&&&&&x&x&V&B \\
&&&&&&&&&&&&&&1&&&&x&x&V&B \\
&&&&&&&&&&&&&&&1&&&x&x&V&B \\
&&&&&&&&&&&&&&&&1&&x&x&V&B \\
&&&&&&&&&&&&&&&&&1&x&x&V&B \\
&&&&&&&&&&&&&&&&&&1&&V&B \\
&&&&&&&&&&&&&&&&&&&1&V&B
\end{array}$$

Figure 6.2 Target Structure of the Gaussian Elimination

By choosing this step size, the sequence $\left\{||\vec{\mathbf{E}}(\vec{\mathbf{Y}})||\right\}$ is guaranteed to be monotonically decreasing. Convergence is achieved when $||\vec{\mathbf{E}}(\vec{\mathbf{Y}}_j)||$ is less than some prescribed tolerance. Although the step size selection in Eq. (6.25) requires additional function evaluations, the result is a more robust algorithm, especially when the initial guess is not close to the final solution. The step size selection is a critical element in the success of the finite difference approach in solving the given optimal ascent problem.

6.3 Jacobian ($\partial\vec{\mathbf{E}}/\partial\vec{\mathbf{Y}}$) Calculation

The Jacobian $\partial\vec{\mathbf{E}}/\partial\vec{\mathbf{Y}}$ required by the Modified Newton Method, is evaluated by a finite difference approximation because of the complexity of an analytical evaluation. The complexity is due to the needed second-order partial derivatives on the right hand side of the state equations. Additionally, if a path constraint is active, the added Lagrange multiple from the constraint (i.e. the angle-of-attack constraint) further adds complexity. Finite difference evaluation are fast because the functions evaluations are algebraic. Also, it was shown previously (27) that numerical Jacobians and analytical Jacobians are numerically the same when comparing values between the 6th and 8th digit. Lastly, the generic nature of the finite difference method requires no change in code when different vehicle configurations are used. The analytical method would require time-intensive derivation of the Jacobian for any vehicle change.

For the boundary conditions, Eqs. (6.13) and (6.14), the Jacobian can be easily be determined analytically. Since the starting boundary condition is $\vec{\mathbf{E}}_0(\vec{\mathbf{Y}}_0) = \vec{\mathbf{B}}_0(\vec{\mathbf{Y}}_0) = \vec{\mathbf{X}}(t_0) - \vec{\mathbf{X}}_0 = 0$, the Jacobian is given by the following matrices.

$$\frac{\partial \vec{\mathbf{E}}_0}{\partial \vec{\mathbf{X}}_0} = \begin{bmatrix} 1 & 0 & 0 & 0 & 0 & 0 & 0 \\ 0 & 1 & 0 & 0 & 0 & 0 & 0 \\ 0 & 0 & 1 & 0 & 0 & 0 & 0 \\ 0 & 0 & 0 & 1 & 0 & 0 & 0 \\ 0 & 0 & 0 & 0 & 1 & 0 & 0 \\ 0 & 0 & 0 & 0 & 0 & 1 & 0 \\ 0 & 0 & 0 & 0 & 0 & 0 & 1 \end{bmatrix} \tag{6.26}$$

$$\frac{\partial \vec{\mathbf{E}}_0}{\partial \vec{\mathbf{P}}_0} = \begin{bmatrix} 0 & 0 & 0 & 0 & 0 & 0 & 0 \\ 0 & 0 & 0 & 0 & 0 & 0 & 0 \\ 0 & 0 & 0 & 0 & 0 & 0 & 0 \\ 0 & 0 & 0 & 0 & 0 & 0 & 0 \\ 0 & 0 & 0 & 0 & 0 & 0 & 0 \\ 0 & 0 & 0 & 0 & 0 & 0 & 0 \end{bmatrix}. \tag{6.27}$$

At the final boundary condition, $\vec{\mathbf{E}}_M(\vec{\mathbf{Y}}_M) = \vec{\mathbf{B}}_f(\vec{\mathbf{Y}}_f) = 0$, the Jacobian is given by the following matrices

$$\frac{\partial \vec{\mathbf{E}}_M}{\partial \vec{\mathbf{X}}_M} = \begin{bmatrix} \vec{\mathbf{r}}_f & 0 & 0 \\ 0 & \vec{\mathbf{V}}_f & 0 \\ \vec{\mathbf{V}}_f \times \vec{\mathbf{1}}_N - \frac{\vec{\mathbf{V}}_f \times \vec{\mathbf{h}}_f}{h_f}\cos(i) & -\vec{\mathbf{r}}_f \times \vec{\mathbf{1}}_N + \frac{\vec{\mathbf{r}}_f \times \vec{\mathbf{h}}_f}{h_f}\cos(i) & 0 \\ \vec{\mathbf{V}}_f & \vec{\mathbf{r}}_f & 0 \\ V_f^2\vec{\mathbf{P}}_{v_f} + \vec{\mathbf{V}}_f(\vec{\mathbf{r}}_f^T\vec{\mathbf{P}}_{r_f}) + & -r_f^2\vec{\mathbf{P}}_{r_f} + \vec{\mathbf{r}}_f(\vec{\mathbf{r}}_f^T\vec{\mathbf{P}}_{r_f}) - & 0 \\ \vec{\mathbf{P}}_{r_f}(\vec{\mathbf{V}}_f^T\vec{\mathbf{r}}_f) - \vec{\mathbf{V}}_f(\vec{\mathbf{V}}_f^T\vec{\mathbf{P}}_{v_f}) & \vec{\mathbf{r}}_f(\vec{\mathbf{V}}_f^T\vec{\mathbf{P}}_{v_f}) - \vec{\mathbf{P}}_{v_f}(\vec{\mathbf{V}}_f^T\vec{\mathbf{r}}_f) & \\ \bar{C}_1 & \bar{C}_2 & 0 \\ 0 & 0 & 0 \end{bmatrix} \tag{6.28}$$

$$\frac{\partial \vec{\mathbf{E}}_M}{\partial \vec{\mathbf{P}}_M} = \begin{bmatrix} 0 & 0 & 0 \\ 0 & 0 & 0 \\ 0 & 0 & 0 \\ 0 & 0 & 0 \\ -r_f^2\vec{\mathbf{V}}_f + \vec{\mathbf{r}}_f(\vec{\mathbf{V}}_f^T\vec{\mathbf{r}}_f) & V_f^2\vec{\mathbf{r}}_f - \vec{\mathbf{V}}_f(\vec{\mathbf{V}}_f^T\vec{\mathbf{r}}_f) & 0 \\ (\vec{\mathbf{h}}_f^T\vec{\mathbf{R}}_N)h_f & (\vec{\mathbf{h}}_f^T\vec{\mathbf{V}}_N)\vec{\mathbf{h}}_f & 0 \\ 0 & 0 & 1 \end{bmatrix} \tag{6.29}$$

where $\vec{\mathbf{R}}_N$, $\vec{\mathbf{V}}_N$, $\bar{C}_1$, $\bar{C}_2$ are defined as

$$\vec{\mathbf{R}}_N = \vec{\mathbf{r}}_f \times \vec{\mathbf{1}}_N \tag{6.30}$$

$$\vec{\mathbf{V}}_N = \vec{\mathbf{V}}_f \times \vec{\mathbf{1}}_N \tag{6.31}$$

$$\begin{aligned} \bar{C}_1 = {} & (\vec{\mathbf{h}}_f^T\vec{\mathbf{P}}_{r_f})(\vec{\mathbf{1}}_N \times \vec{\mathbf{h}}_f + \vec{\mathbf{V}}_f \times \vec{\mathbf{R}}_N) + (\vec{\mathbf{h}}_f^T\vec{\mathbf{R}}_N)(\vec{\mathbf{V}}_f \times \vec{\mathbf{P}}_{r_f}) \\ & +(\vec{\mathbf{h}}_f^T\vec{\mathbf{P}}_{v_f})(\vec{\mathbf{V}}_f \times \vec{\mathbf{V}}_N) + (\vec{\mathbf{h}}_f^T\vec{\mathbf{V}}_N)(\vec{\mathbf{V}}_f \times \vec{\mathbf{P}}_{v_f}) \end{aligned} \tag{6.32}$$

$$\begin{aligned} \bar{C}_2 = {} & (\vec{\mathbf{h}}_f^T\vec{\mathbf{P}}_{v_f})(\vec{\mathbf{1}}_N \times \vec{\mathbf{h}}_f + \vec{\mathbf{V}}_N \times \vec{\mathbf{r}}_f) + (\vec{\mathbf{h}}_f^T\vec{\mathbf{V}}_N)(\vec{\mathbf{P}}_{v_f} \times \vec{\mathbf{r}}_f) \\ & (\vec{\mathbf{h}}_f^T\vec{\mathbf{P}}_{r_f})(\vec{\mathbf{R}}_N \times \vec{\mathbf{r}}_f) + (\vec{\mathbf{h}}_f^T\vec{\mathbf{R}}_N)(\vec{\mathbf{P}}_{r_f} \times \vec{\mathbf{r}}_f). \end{aligned} \tag{6.33}$$

In some instances, the approximations $r_f \approx r_f^*$ and $\gamma_f \approx \gamma_f^*$ are used to simplify the Jacobian.

6.4 Final Time Adjustment

In order to solved the boundary value problem, the finite difference scheme assumes a fixed final time. However, the ascent guidance problem is a free final time problem. The following algorithm is used to adjust the final time and satisfy the final transversality condition, Eq. (4.12). First, a solution to the fixed final time problem is solved. The Hamiltonian is then evaluated at the final time, giving $H(t_{f_1})$. The final time is then perturbed by some value, δ, so $t_{f_2} = t_{f_1} + \delta$. A new trajectory is generated and the Hamiltonian evaluated at the new final time, $H(t_{f_2})$. The objective is to find a final time to satisfy the terminal constraint, so an updated value is calculated using the secant method

$$t_{f_3} = t_{f_2} - \frac{t_{f_2} - t_{f_1}}{H(t_{f_2}) - H(t_{f_1})} H(t_{f_2}). \tag{6.34}$$

This process is repeated until $|H(t_f)| < \epsilon$. The above equation can be generalized as

$$t_{f_{k+1}} = t_{f_k} - \frac{t_{f_k} - t_{f_{k-1}}}{H(t_{f_k}) - H(t_{f_{k-1}})} H(t_{f_k}). \tag{6.35}$$

6.5 Initial Guess

The finite difference method needs an initial guess, $\vec{\mathbf{Y}}_{j,k}$. The initial guess used begins with a vacuum solution for a rocket using constant thrust, as described in Ref. (27). The resulting vacuum trajectory is a single burn trajectory with constant mass rate. The algorithm provides state, costate, and final time information. However, since the algorithm uses a constant mass rate, the mass is treated as an explicit function of time and the mass costate is not needed. The solution does not provide either the mass state or the associated mass costate, P_m. In order to remedy the lack of information, the vacuum solution is appended the values using the following process. For the mass state, the initial mass is known and the time vector is given by the rocket vacuum solution.

The dimensionless mass rate is

$$m' = -\sqrt{\frac{r_0}{g_0}}\frac{mT}{\mathrm{I}_{sp}}. \tag{6.36}$$

This allows the mass state to be determined by integrating the above equation forward in time.

The mass costate is determined by Eq. (4.15) with some simplification. Since the guess is a vacuum solution, both aerodynamic forces, A and N, can be removed. Second, it is a well known result for optimal rocket flight in a vacuum, that the optimal body x-axis aligns with the costate vector $\vec{\mathbf{P}}_v$ (27). The equation can then be rewritten as

$$P'_m = -\vec{\mathbf{P}}_v^T \vec{\mathbf{P}}_v \left(\frac{\partial T}{\partial m} \right). \tag{6.37}$$

The costate vector $\vec{\mathbf{P}}_v$ is provide by rocket vacuum solution. Finally, the transversality condition, Eq. (4.60), gives the end condition $P_m(t_f) = 1$. This allows the mass costate to be determined by integrating the above equation backwards in time.

In order to develop a full atmospheric solution, a homotopy method is applied to gradually introduce the aerodynamic terms. Only the atmospheric density is modified,

$$\hat{\rho} = \kappa\rho, \quad 0 \leq \kappa \leq 1 \tag{6.38}$$

where the modified density, $\hat{\rho}$, is placed everywhere ρ appears in the state, costate, and path constraint equations. The homotopy parameter, κ, begins at 0 and solves the vacuum solution for the hypersonic vehicle, using the initial guess described. The term is then increased and the previous solution is used as the initial guess until $\kappa = 1$. In this research, once the atmospheric solution was found, all other variations of initial and final conditions could be solved using the original atmospheric solution.

6.6 Algorithm Modification for Changes in Vehicle

The desired algorithm to find an optimal solution would be independent of vehicle used. Much effort was done to minimize any changes needed to the overall algorithm if the vehicle model was changed. This section outlines what items need to be changed when either the vehicle model is changed or the final conditions.

The optimal control problem is defined for a vehicle in an inertial coordinate system where the aerodynamic forces, A and N, act in the body longitudinal and normal direction respectively, and thrust acts in the body longitudinal direction. The derivation of the necessary conditions remain the same for all vehicles described by those equations of motion.

The expansion of the costates is where any changes to algorithm and therefore the code need to be made. In general, the aerodynamic forces can be found using Eqs. (3.21) and (3.22), however both the normal and axial force coefficients, C_N and C_A respectively, are unique to a vehicle. The expanded costates need these terms as well as their partial with respect to Mach and angle-of-attack.

In general, hypersonic vehicles have an engine that are functions state and attitude of the vehicle. But, the engine model used in this research was unique to the GHAME model. The costate equation took this into account, however, the differentiation of thrust with respect to the states, $\partial T/\partial \vec{\mathbf{r}}$, $\partial T/\partial \vec{\mathbf{V}}$, and $\partial T/\partial m$, would change with the engine model used. Therefore, the expansion of the costate terms that involved those differentiations would need to be updated. Additionally, the engine model would need to supply the effect of thrust due to changes in Mach and angle-of-attack.

Lastly, the transversality conditions are dependent on the final conditions specified by the user. If a different set of final conditions are desired, the user would need to find the seven terminal boundary conditions as a function solely of states and costates. The algorithm would then need to be adjusted where the Jacobian $(\partial \vec{\mathbf{E}}/\partial \vec{\mathbf{Y}})$ calculation is made.

CHAPTER 7. ANALYSIS AND RESULTS

7.1 Open-Loop Solutions

7.1.1 Verification and Validation

To check the validity of the finite difference method, open-loop results are compared to results from a commercial optimization software based on a pseudospectral method, Direct and Indirect Dynamic Optimization (DIDO). DIDO is a MATLAB$^{\text{TM}}$ program that solves optimal control problems using the optimization engine Sparse Nonlinear Optimizer (SNOPT). The software approximates the problem by pseudospectral techniques into a finite dimensional problem and obtains a solution numerically (35). The ascent trajectory optimization problem solved in DIDO is modeling the dynamics of a 2-dimensional point mass over a non-rotating Earth. The DIDO solution uses 50 nodes and the cost function is to minimize final mass. The finite difference method uses 100 nodes. Additionally, winds are not included and the rotation of the Earth is removed. Both methods use the same initial conditions and final target conditions. The same aerodynamic and engine model are used for both methods.

Figures 7.1 to 7.4 show the comparison of two trajectories generated using DIDO and the finite difference method. The following initial conditions are used: initial altitude of 76,000 feet; initial velocity of 5,500 ft/s; initial weight of 280,000 pounds. The throttle command is assumed to be set at the maximum value, $\phi_t = 2$. From various DIDO runs it was determined that the optimal value is always the upper bound. The final conditions were: final altitude of 130,000 feet; final velocity of 14,000 ft/s; final inclination angle of 51.6 °; final flight path angle of 0 °.

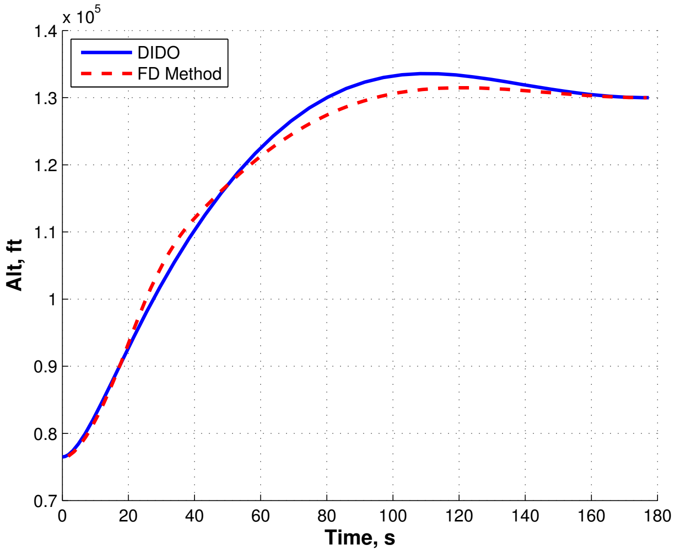

Figure 7.1 Altitude Comparison of Finite Difference Method with Optimization Software

Both methods are solving the free final time problem. The final time for the finite difference method is 176.8 seconds, while DIDO results in a final time of 177.4 seconds. Final weight for the finite difference method is 228,100 pounds and 228,500 pounds for the DIDO solution. Although the final conditions are close, the trajectory profiles show some differences. The DIDO solution overshoots the final altitude much more than the finite difference method. This is reflected in the angle-of-attack comparisons. The difference can be attributed to the lack of dynamics in the 2D model. The comparison supports the validity of the finite difference approach.

7.1.2 Unconstrained Open-loop Solutions and Trajectory Trends

This section provides several open-loop solutions to illustrate the characteristics of trajectories for a hypersonic vehicle. Various initial and final conditions were selected and the resulting trajectories are presented. The first set of solutions shown have fixed final

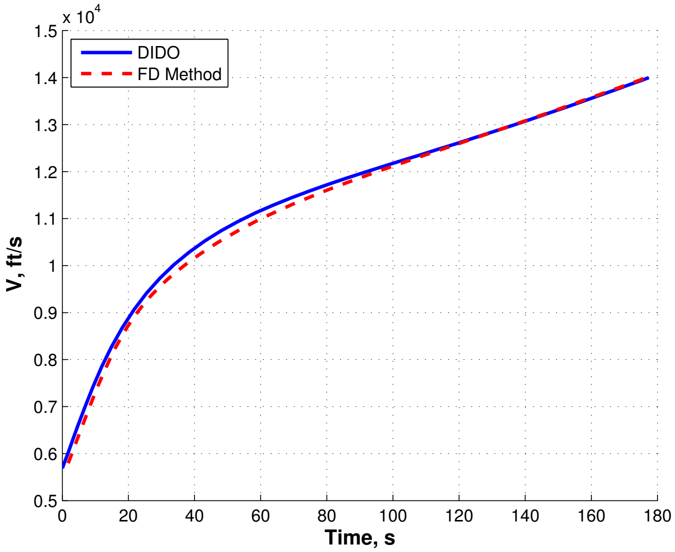

Figure 7.2 Velocity Comparison of Finite Difference Method with Optimization Software

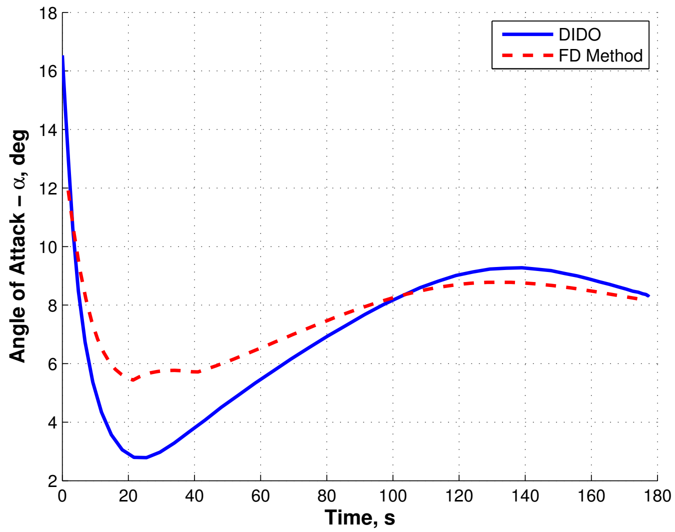

Figure 7.3 Angle-of-Attack Comparison of Finite Difference Method with Optimization Software

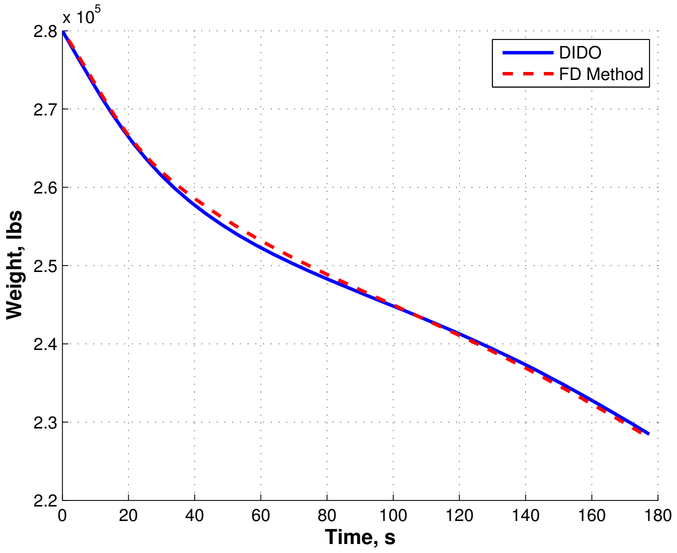

Figure 7.4 Weight Comparison of Finite Difference Method with Optimization Software

conditions, while the initial altitude is varied. The final conditions are: final inclination (i_f^*), 51.6 °; final flight path (γ_f^*), 0 °; final altitude ($r_f^* - R_0$), $130,000 ft$; final velocity (v_f^*), $14,000 ft/s$. Initial velocity is 5,500 ft/s and initial mass is 280,000 lbs. Table 7.1 lists the variations in initial altitude for each trajectory, as well as the resulting final time and final weight. Figures 7.5 to 7.9 show the trajectory profiles.

Table 7.1 Open-Loop Comparison - Alt$_f$ $130,000ft$, V$_f$ $14,000ft/s$

Initial Altitude, ft	Final Time, s	Final Weight, lbs
55,000	101.3	233,138
60,000	129.3	233,744
65,000	144.4	234,113
70,000	155.8	234,344
75,000	165.0	234,501
80,000	173.2	234,617
85,000	180.5	234,711
90,000	185.4	234,769
95,000	190.2	234,795

Both Table 7.1 and Figure 7.5 show that as the vehicles initial altitude increases,

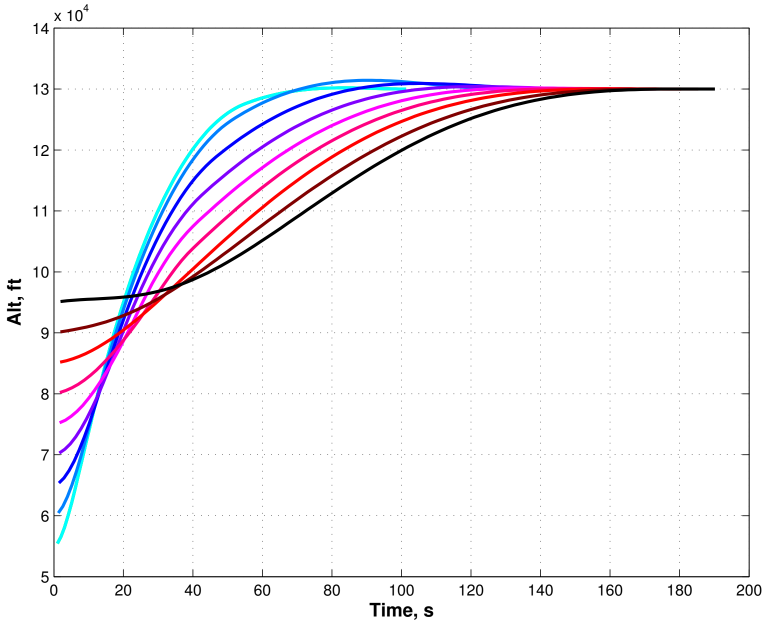

Figure 7.5 Altitude Comparison - Alt$_f$ $130,000ft$, V$_f$ $14,000ft/s$

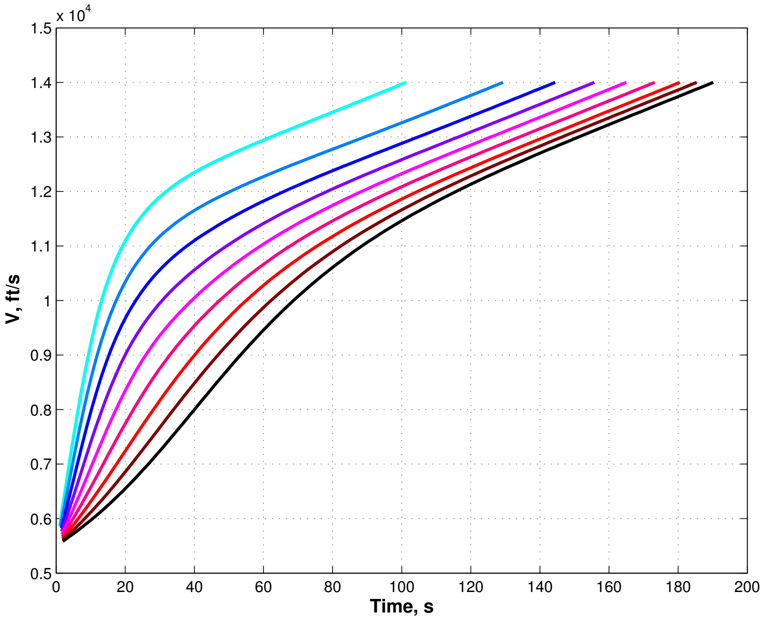

Figure 7.6 Velocity Comparison - Alt$_f$ $130,000ft$, V$_f$ $14,000ft/s$

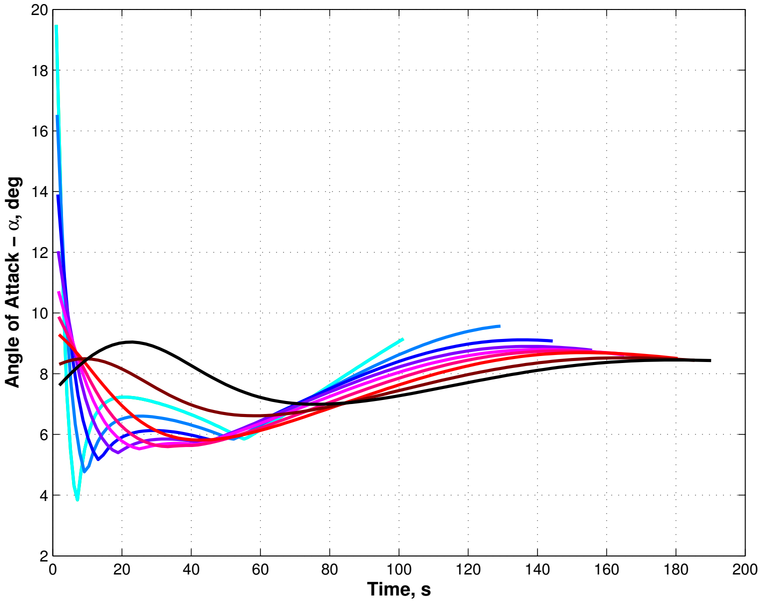

Figure 7.7 Angle-of-Attack Comparison - Alt$_f$ $130,000ft$, V$_f$ $14,000ft/s$

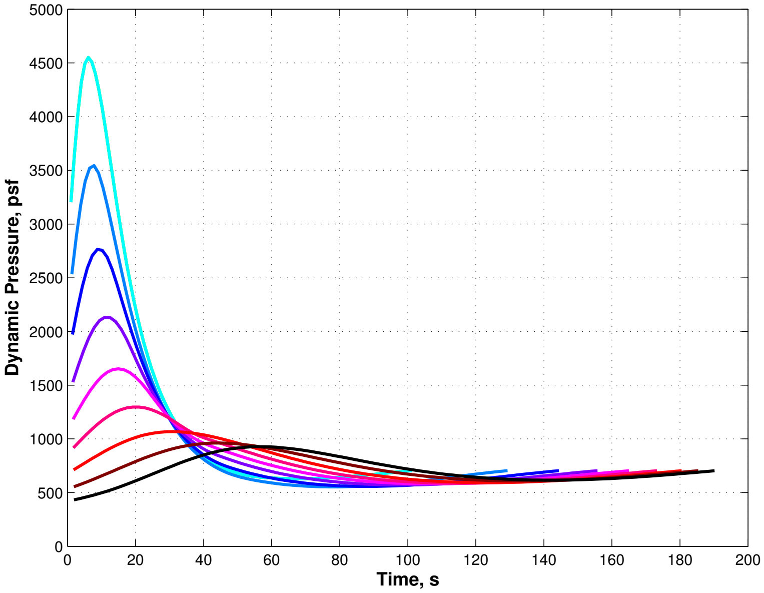

Figure 7.8 Dynamic Pressure Comparison - Alt$_f$ $130,000ft$, V$_f$ $14,000ft/s$

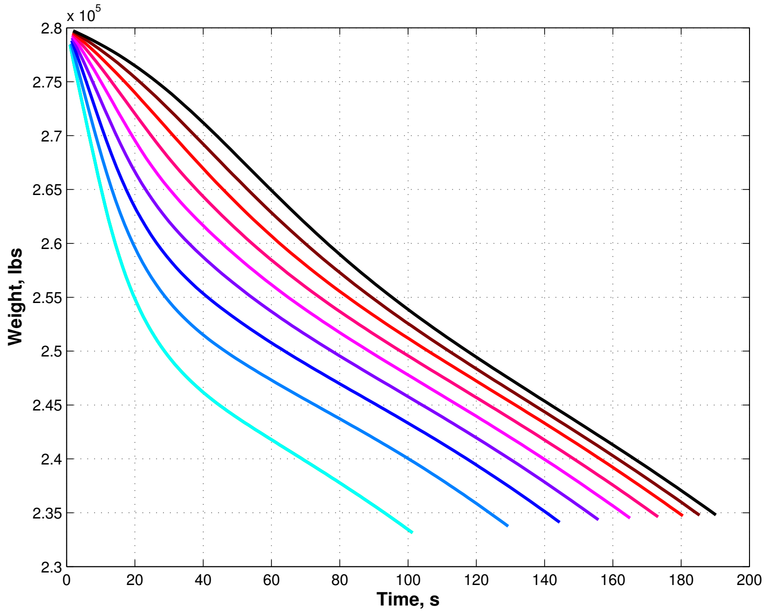

Figure 7.9 Weight Comparison - Alt$_f$ $130,000ft$, V$_f$ $14,000ft/s$

total time increases yet final weight decreases. The behavior is counterintuitive. Since the vehicle is traveling a greater distance it would be expected that travel would require additional time. The response can be explained from the engine model, restated below

$$T = (0.029\phi_t)\rho \mathrm{I}_{sp} G_0 V C_T A_c. \tag{7.1}$$

As altitude increases, density (ρ) decreases, causing thrust to decrease. Therefore, at lower altitudes the vehicle has a larger acceleration than at higher altitudes. This allows the vehicle to achieve the target velocity in a shorter amount of time and as a consequence, meet the final altitude in the same short time frame. Additionally, since thrust directly effects mass rate, as seen in Eq. (7.2), the increase in thrust at lower altitudes also increases mass rate, resulting in more fuel being consumed.

$$\dot{m} = -\frac{T}{G_0 \mathrm{I}_{sp}} \tag{7.2}$$

The small flight path angle (and small angle-of-attack seen in Figure 7.7) in the high initial altitude cases can also be explained by the above reasoning. Since the atmosphere is thin, the engine is unable to produce adequate thrust to reach the desired velocity. The optimal solution requires the altitude to initially stay near constant to achieve the targeted velocity.

In the next set of solutions, the initial conditions are held constant, and the final altitude is varied. Initial altitude is 90,000 ft, initial velocity is 5,500 ft/s, final velocity is 14,000 ft/s, final inclination is 51.6 °, and final flight path is 0 °. Final altitude is varied from 130,000 ft to 200,000 ft, and the results are summarized in Table 7.2 and Figures 7.10 to 7.14 show the various trajectories comparisons.

Table 7.2 Open-Loop Comparison - Alt$_I$ $90,000ft$, V$_f$ $14,000ft/s$

Final Altitude, ft	Final Time, s	Final Weight, lbs
130,000	185.4	234,770
140,000	178.3	234,570
150,000	172.7	232,800
160,000	169.3	233,930
170,000	167.2	233,530
180,000	165.6	233,130
190,000	165.3	232,730
200,000	166.0	232,350

Once again, the data shows a counterintuitive behavior, as the final altitude increases the final time decreases. However, fuel consumption increases even though the time of flight is shorter. A closer look at the profiles reveals why this occurs. In order for the vehicle to attain higher altitudes, the optimal trajectory keeps the vehicle at lower altitudes initially to quickly increase the speed. This can be seen in the velocity comparison plot, Fig. 7.11, and the angle-of-attack plot, Fig. 7.12. This is even more pronounced for the $alt_f = 180,000ft$, $alt_f = 190,000ft$, and $alt_f = 200,000ft$ cases, where the vehicle initially has a negative flight path angle and the altitude decreases in the early moments of the trajectory. The lower altitude results in higher thrust and therefore faster rate of fuel consumption, resulting in the lower final weight, similar to the previous set of cases.

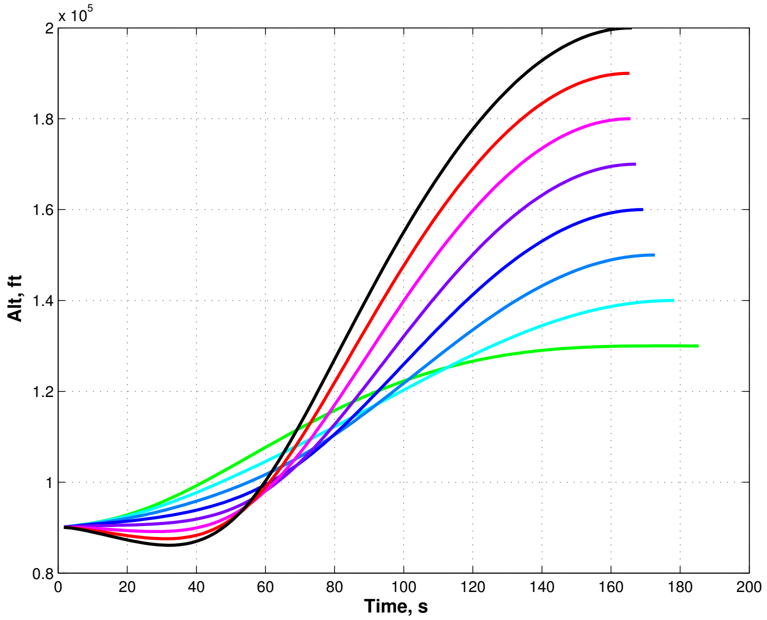

Figure 7.10 Altitude Comparison - Alt$_I$ $90,000ft$, V$_f$ $14,000ft/s$

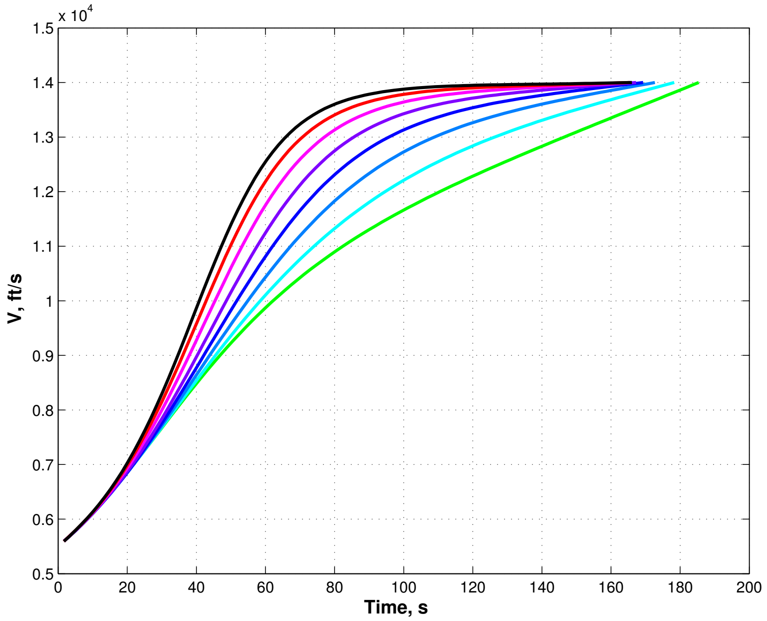

Figure 7.11 Velocity Comparison - Alt$_I$ $90,000ft$, V$_f$ $14,000ft/s$

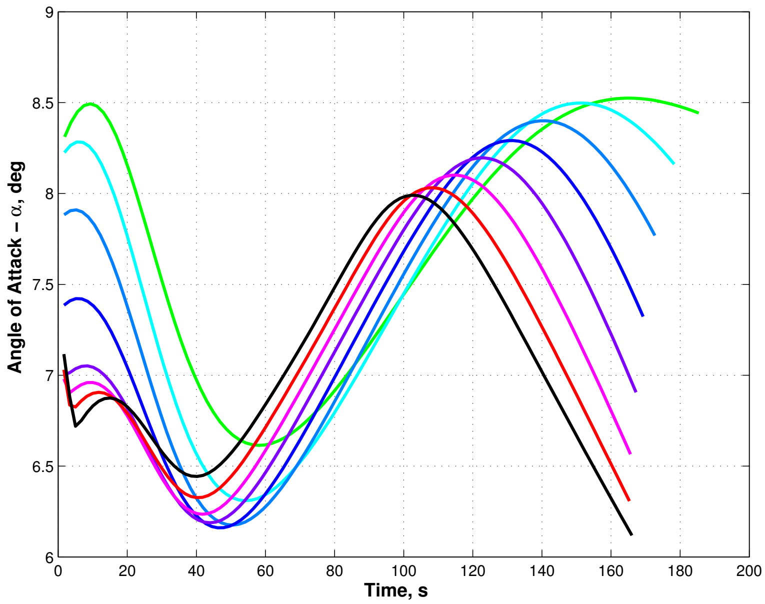

Figure 7.12 Angle-of-Attack Comparison - Alt$_I$ 90, 000ft, V$_f$ 14, 000ft/s

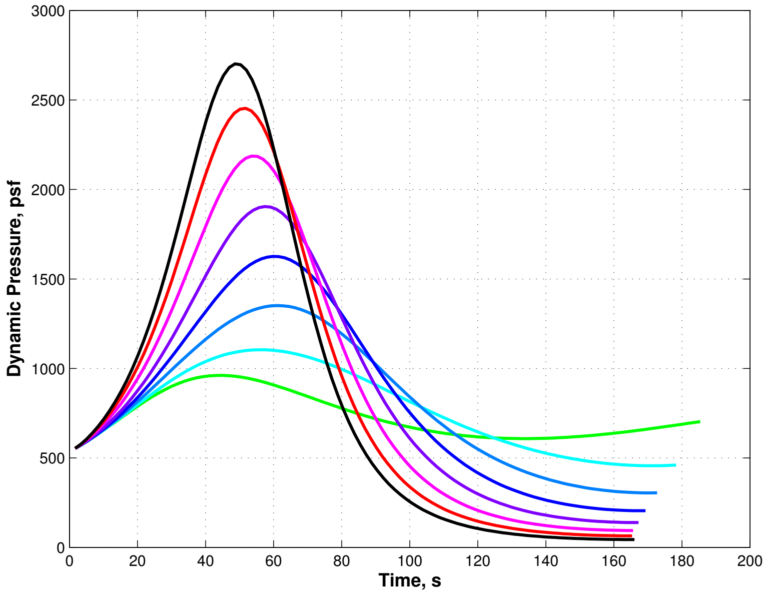

Figure 7.13 Dynamic Pressure Comparison - Alt$_I$ 90, 000ft, V$_f$ 14, 000ft/s

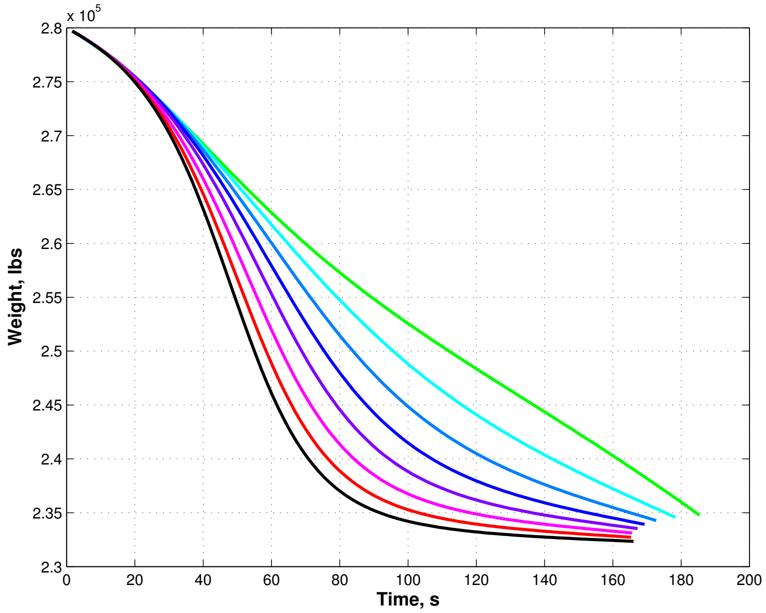

Figure 7.14 Weight Comparison - Alt$_I$ $90,000ft$, V$_f$ $14,000ft/s$

The next set of trajectories have the same conditions as previous, with the exception of final velocity, which is set at 16,000 ft/s. Table 7.3 has the summary of results and Figures 7.15 to 7.19 are the plots of the different trajectories.

Table 7.3 Open-Loop Comparison - Alt$_I$ $90,000ft$, V$_f$ $16,000ft/s$

Final Altitude, ft	Final Time, s	Final Weight, lbs
130,000	274.0	214,900
140,000	280.8	214,710
150,000	288.3	214,380
160,000	295.2	213,950
170,000	300.9	213,450
180,000	305.8	212,920
190,000	310.0	212,400
200,000	313.5	211,900

Unlike the previous set of solutions, the increase in final velocity causes an increase in final time and decrease in final weight when the final altitude is increased. The lowest final altitude, $alt_f = 130,000ft/s$ overshoots the final altitude and the latter portion of the trajectory has a negative flight path angle before leveling out. This dive is needed to

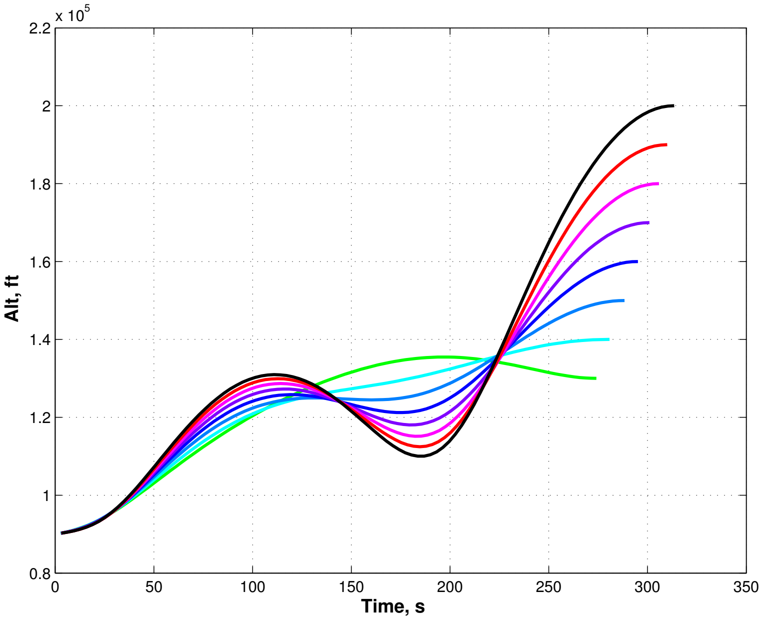

Figure 7.15 Altitude Comparison - Alt$_I$ $90,000ft$, V$_f$ $16,000ft/s$

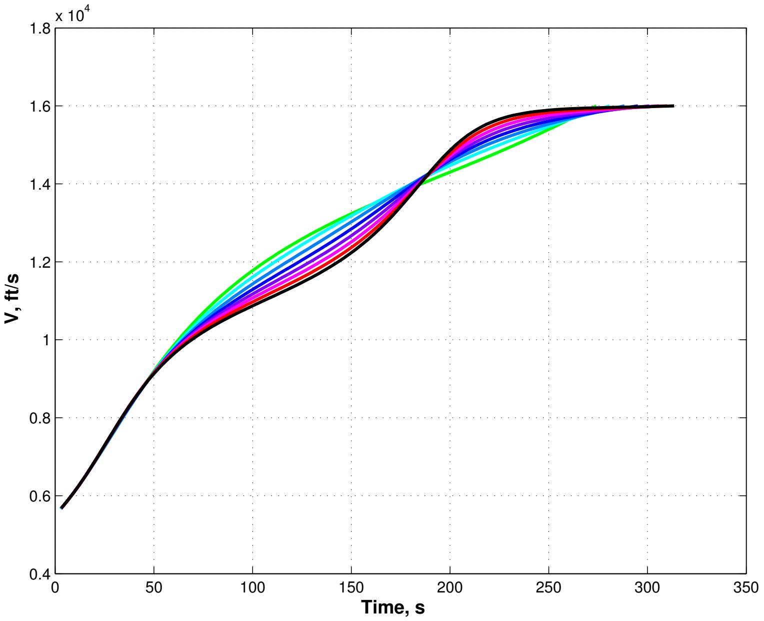

Figure 7.16 Velocity Comparison - Alt$_I$ $90,000ft$, V$_f$ $16,000ft/s$

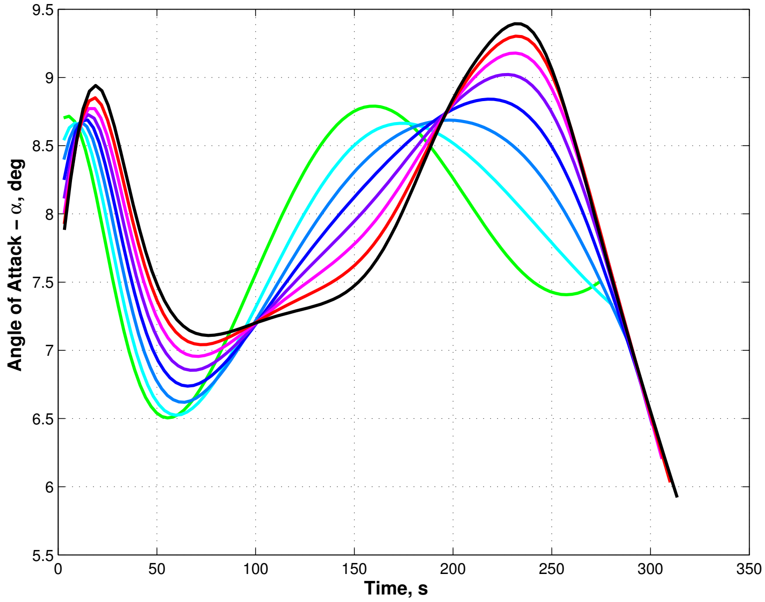

Figure 7.17 Angle-of-Attack Comparison - Alt$_I$ 90, 000ft, V$_f$ 16, 000ft/s

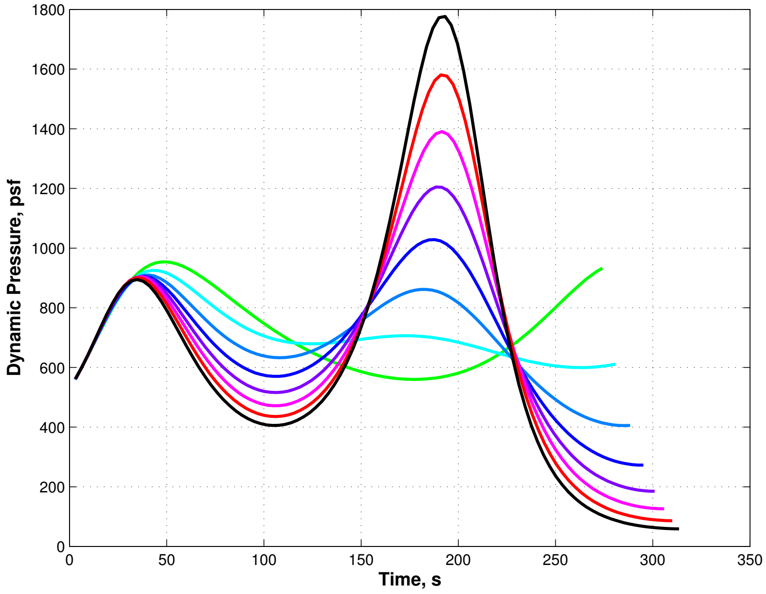

Figure 7.18 Dynamic Pressure Comparison - Alt$_I$ 90, 000ft, V$_f$ 16, 000ft/s

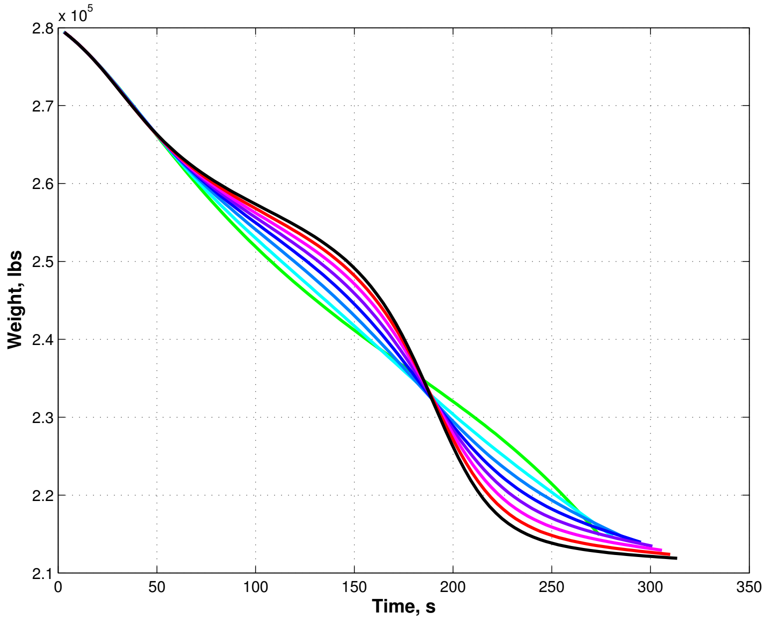

Figure 7.19 Weight Comparison - Alt$_I$ $90,000ft$, V$_f$ $16,000ft/s$

increase the speed to meet the final velocity requirement. The optimal solution is using the potential energy and the increasing density to help increase the vehicles acceleration. Another observation, as the final altitude condition increases, there are occurrences of “two-peak” trajectories. These two-peak trajectories are also taking advantage of the potential to kinetic energy conversion and the thrust increase from the drop in altitude. These trajectories resulting for the optimal control problem finds that the solution keeps fuel consumption minimized rather than maintaining lower altitudes for a longer duration to increase thrust and therefore velocity.

Table 7.4 and Figures 7.20 to 7.24 are resulting data and trajectory profiles for solutions with the same initial and final conditions as the previous set of trajectories, however, the initial altitude is lowered to 75,000 ft.

When compared to the previous set of trajectories, the same characteristics are present. The increase in final altitude results in longer flight time and lower final weight. In comparison, the lower altitude results in 20 additional seconds of final time and only

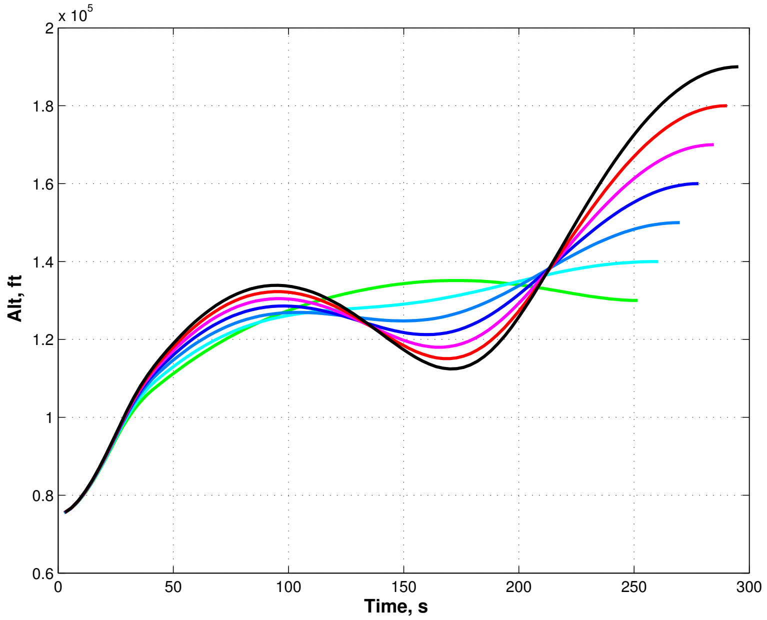

Figure 7.20 Altitude Comparison - Alt$_I$ $75,000ft$, V$_f$ $16,000ft/s$

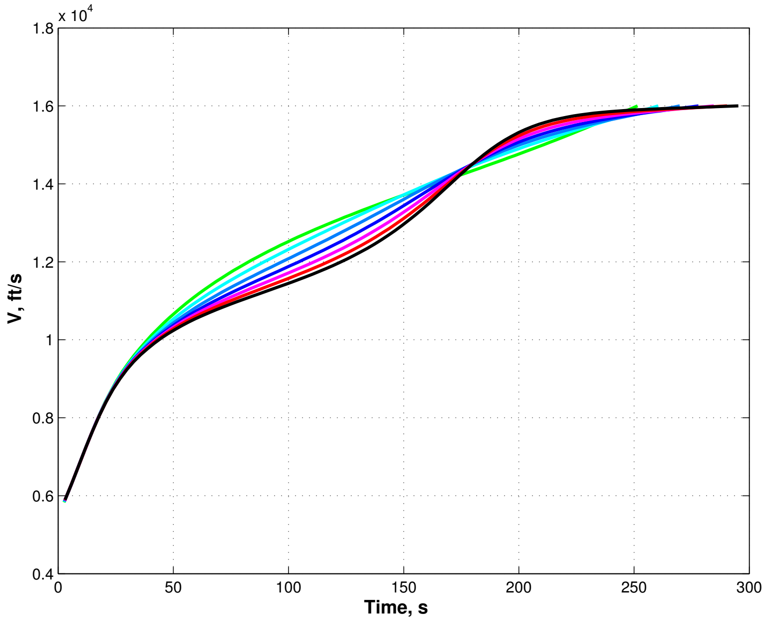

Figure 7.21 Velocity Comparison - Alt$_I$ $75,000ft$, V$_f$ $16,000ft/s$

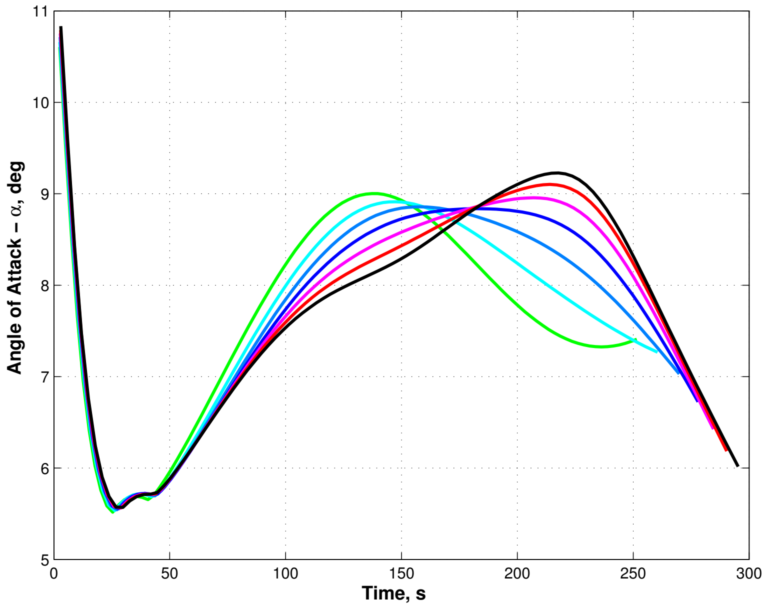

Figure 7.22 Angle-of-Attack Comparison - Alt$_I$ $75,000ft$, V$_f$ $16,000ft/s$

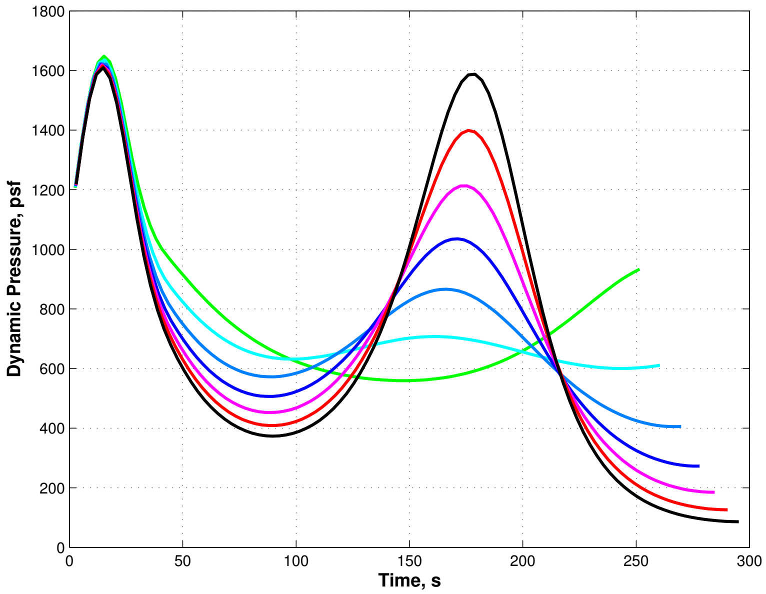

Figure 7.23 Dynamic Pressure Comparison - Alt$_I$ $75,000ft$, V$_f$ $16,000ft/s$

Table 7.4 Open-Loop Comparison - Alt$_I$ $75,000ft$, V$_f$ $16,000ft/s$

Final Altitude, ft	Final Time, s	Final Weight, lbs
130,000	251.5	214,650
140,000	260.5	214,460
150,000	269.8	214,140
160,000	277.9	213,720
170,000	284.6	212,230
180,000	290.3	212,710
190,000	295.3	212,190

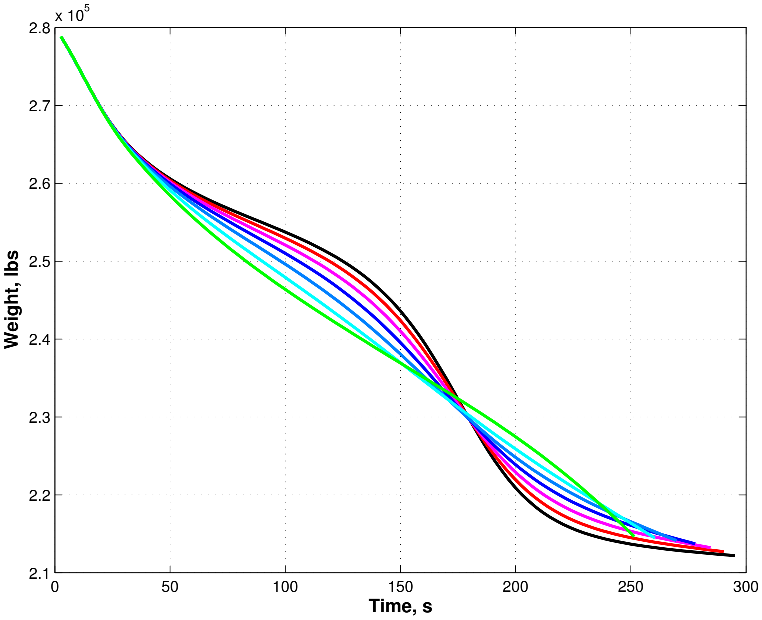

Figure 7.24 Weight Comparison - Alt$_I$ $75,000ft$, V$_f$ $16,000ft/s$

200 to 500 pounds of additional fuel usuage. Also note the requirement of the two-peak trajectories.

7.1.3 Constrained Open-loop Solutions

Two constraints were considered in this research, however the dynamic pressure constraint is only being enforced during closed-loop simulations (see Section 4.1.5.1). The angle-of-attack constraint was implemented in the open-loop trajectory generation. Four solutions are presented to show the effect of the constraint on the trajectory. Initial altitude is 85,000 ft and initial velocity is 5,500 ft/s. Final flight path angle is 0 °, and final inclination is 51.6 °. The final altitude and velocity conditions are varied. Although angle-of-attack was small for many of the previous solutions, a limit of 8.5 ° was selected to demonstrate the finite difference method's capability in enforcing the constraint. Table 7.5 list the various final conditions and the resulting flight time and final weight. Figures 7.25 to 7.29 are plots the resulting trajectory profiles. For comparison, trajectories with the same initial and final conditions without the constraint are included. A dashed line in the plots are used to signify the unconstrained solutions.

Table 7.5 Open-Loop Comparison with α Constraint - Alt$_I$ $85,000ft$

Final Alt, ft	Final V, ft/s	Final Time, s	Final Weight, lbs	
130,000	14,000	178.0	234,710.9	Constrained
130,000	14,000	180.5	234,711.0	Unconstrained
130,000	16,000	262.9	214,842.4	Constrained
130,000	16,000	268.5	214,840.0	Unconstrained
150,000	16,000	280.0	214,331.2	Constrained
150,000	16,000	284.4	214,336.5	Unconstrained
170,000	16,000	293.0	213,402.1	Constrained
170,000	16,000	297.0	213,414.2	Unconstrained

Figure 7.27 clearly shows that for various initial and final conditions, the constraint on angle-of-attack is enforced. The table shows the constrained solutions requiring slightly more fuel than the unconstrained trajectories. However, when comparing the

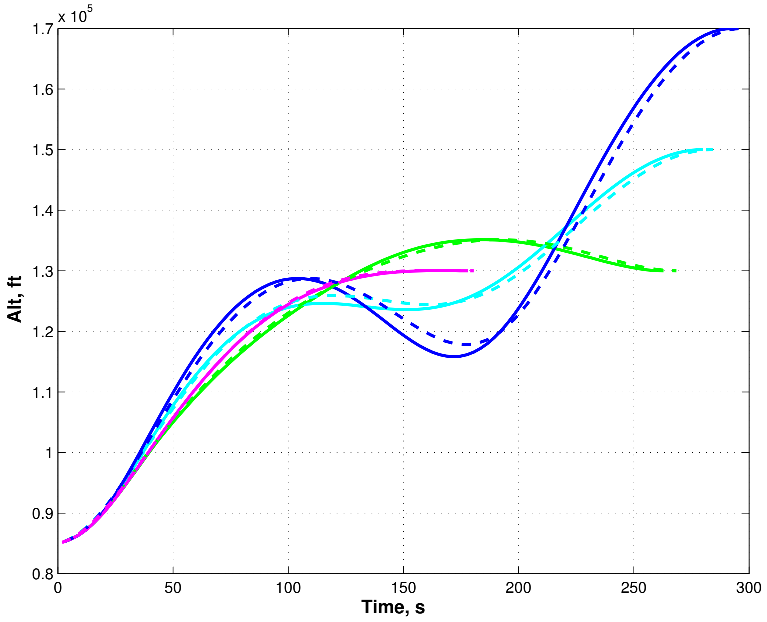

Figure 7.25 Altitude Comparison with α Constraint

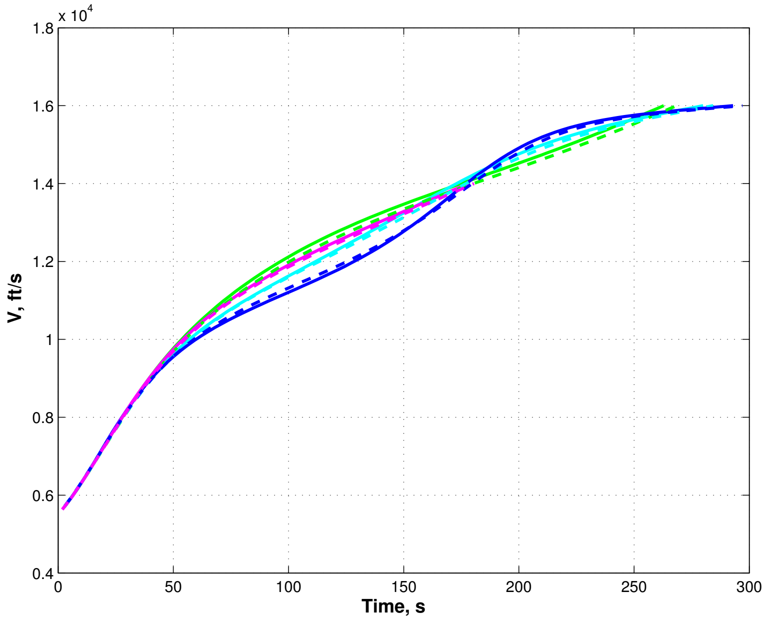

Figure 7.26 Velocity Comparison with α Constraint

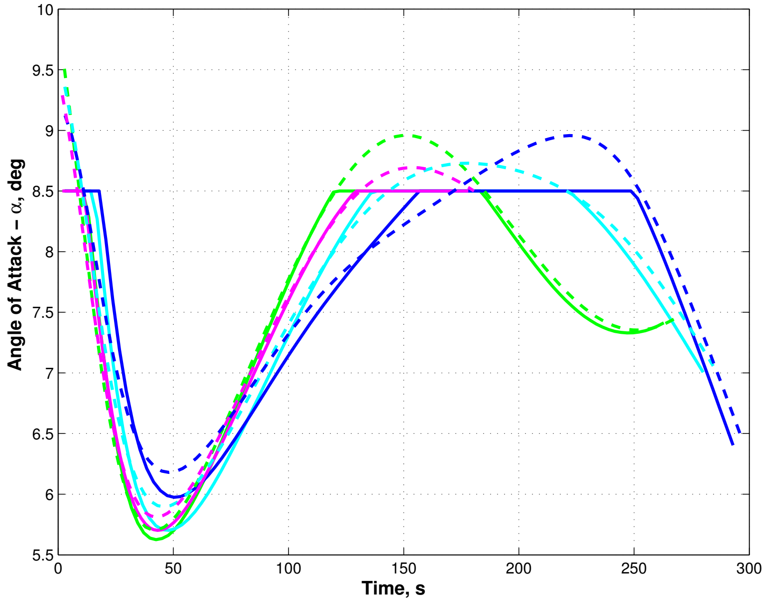

Figure 7.27 Angle-of-Attack Comparison with α Constraint

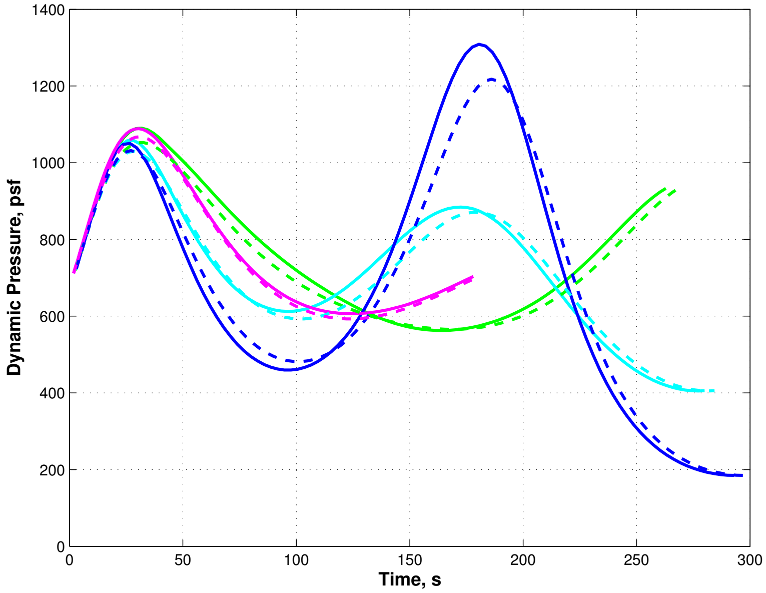

Figure 7.28 Dynamic Pressure Comparison with α Constraint

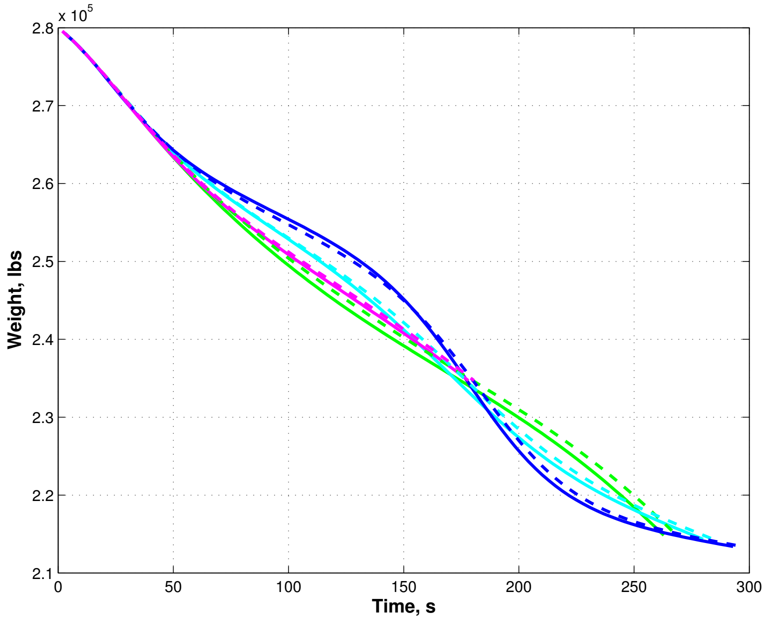

Figure 7.29 Weight Comparison with α Constraint

final times, these trajectories require a shorter flight time when the constraint is active than the unconstrained solutions. The longer time can be associated with the increased angle of attack allowing for an increase altitude and therefore a decrease in thrust. However, the trajectories for final altitude of 130,000 ft and final velocity of 16,000 ft/s this not true, with the constrained solution requiring less time and less fuel than the unconstrained solution.

7.2 Closed-Loop Simulations

Closed-loop simulation is done to test the feasibility of using the finite difference method as a guidance algorithm with a flight control system. The guidance algorithm is required to issue a command each guidance cycle. In this research, the update rate is 1 Hz. For the finite difference method to be a viable option as a guidance algorithm, it is required that a converged solution to the optimal control problem be found within the guidance cycle (i.e. within one second). The current state of the vehicle (time, position, velocity, etc) is passed to the algorithm and used to calculate an updated optimal trajectory and the first body vector in the resulting trajectory calculation is passed as the guidance command. Simulations were ran with various initial and final conditions, as done with the open-loop solutions. Also, angle-of-attack and dynamic pressure constraints are used for a subset of the closed-loop simulations.

Unlike the open-loop trajectories, winds are included in the both trajectory calculation and the closed-loop simulations. The wind profiles are based from measured wind velocities at various altitudes at NASA Kennedy Space Center. Smoothing was done on the data for guidance purposes. The east and north velocity components, u and v respectively, are obtained each guidance cycle using the current altitude and interpolating the data. The wind magnitude is given by

$$V_w = \sqrt{u^2 + v^2}. \tag{7.3}$$

One set of winds was used for guidance calculations while another was used in simulations. This was done to illustrate the difference between actual winds and measured winds, since it is common for measured wind data to be greater than three hours old.

Since the finite difference method solves the free final time problem, the guidance algorithm could adjust the final time each guidance cycle. To speed up the guidance algorithm and assist with convergence of the optimal trajectory, when the guidance system determined there were 50 seconds left in the ascent, no additional adjustments were made to the final time. However, a trajectory is still calculated using the fixed final time approach. With only 20 seconds remaining in the simulation, no additional trajectories are calculated and the previous solution is iterated and used to issue the guidance commands. Stopping the calculation for final time was justified because with little time left there was little to effect the final time. Altitude would be sufficiently high so that dynamic pressure would not cause that constraint to become active. Also, the angle-of-attack constraint would already be incorporated in the fixed final time solution. Finally, using the open-loop solution with only 20 seconds left was justified for the same reasons. Finally, any changes in the dynamics from using these simplifications would minimally effect the final mass.

7.2.1 Unconstrained Closed-loop Simulations

The first set of plots, Figures 7.30 to 7.35, show a comparison of an open-loop solution and closed-loop simulations. The initial conditions are: initial altitude 85,000 ft; initial velocity 5,500 ft; initial weight 280,000 lbs. Final conditions are: final altitude 130,000 ft; final velocity 14,000 ft/s; final inclination 51.6 °; final flight path angle 0 °. No constraints are enforced, but as mentioned before, winds are included in the guidance calculations and simulations.

From the altitude and velocity comparison, there is little differences that can be seen between the open-loop guidance calculation and the closed-loop simulation. Table 7.6

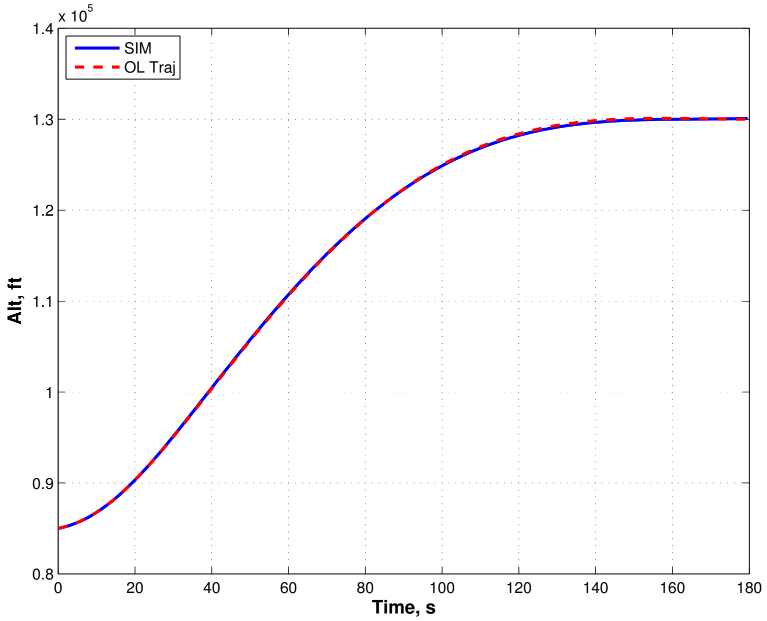

Figure 7.30 Closed-Loop vs. Open-Loop - Altitude Comparison

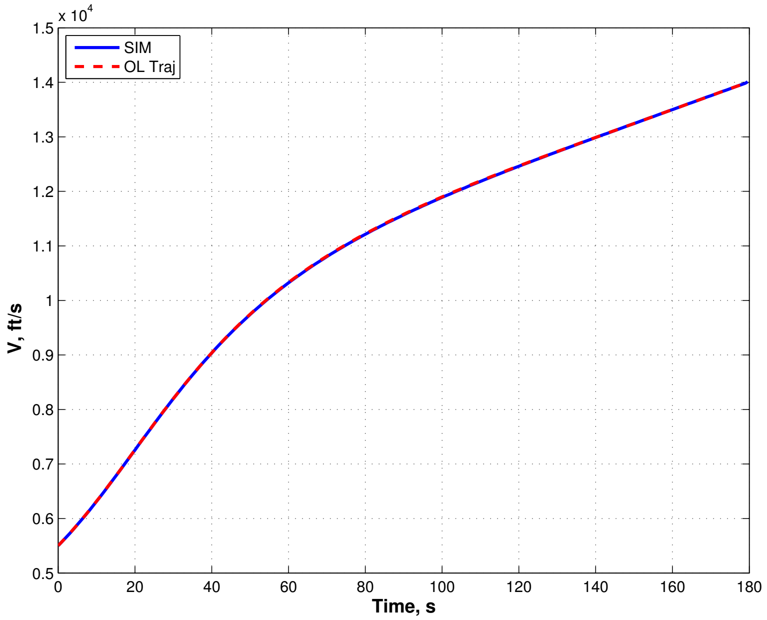

Figure 7.31 Closed-Loop vs. Open-Loop - Velocity Comparison

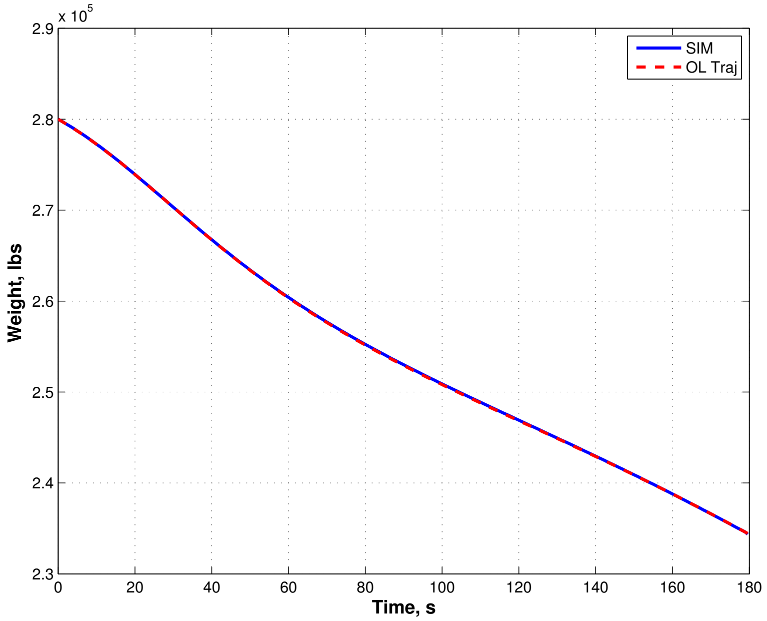

Figure 7.32 Closed-Loop vs. Open-Loop - Weight Comparison

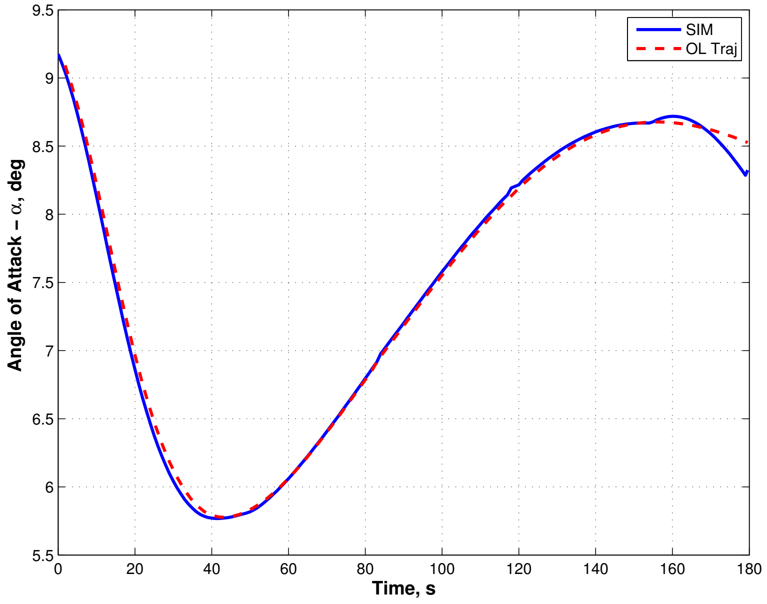

Figure 7.33 Closed-Loop vs. Open-Loop - Angle-of-Attack Comparison

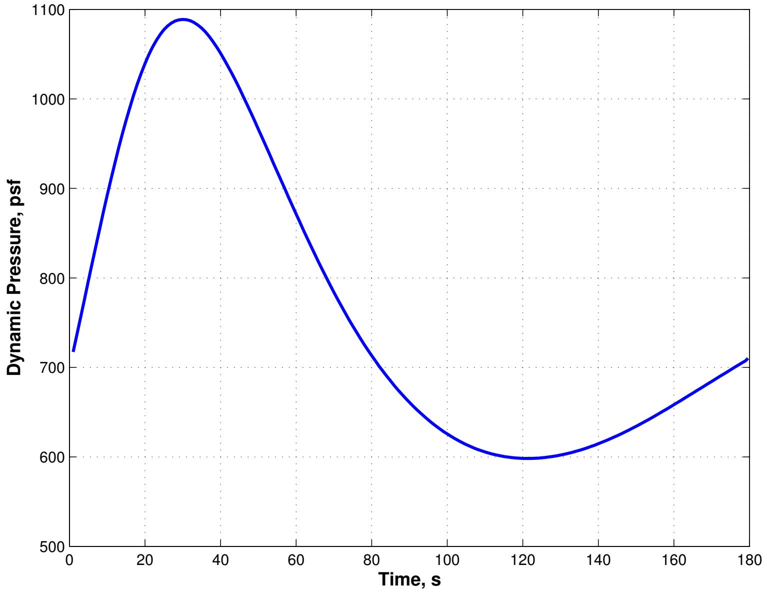

Figure 7.34 Closed-Loop vs. Open-Loop - Dynamic Pressure Comparison

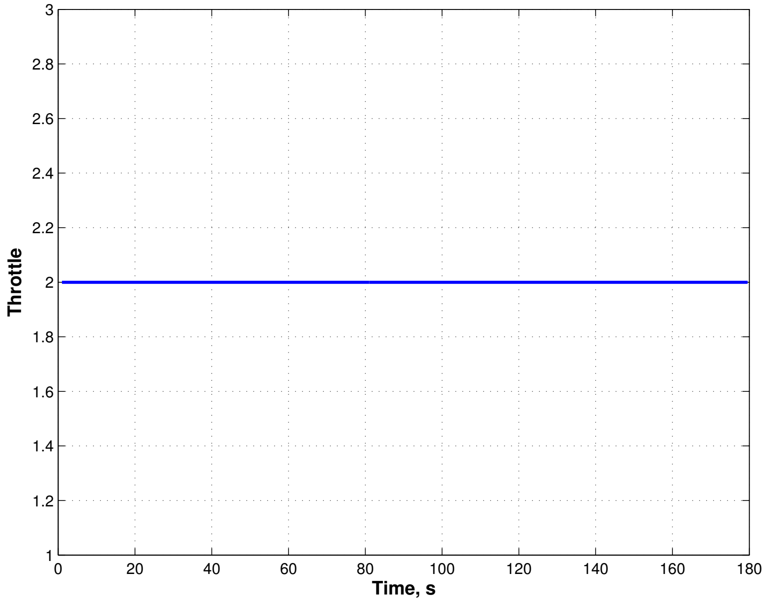

Figure 7.35 Closed-Loop vs. Open-Loop - Throttle Comparison

show the numerical differences for the final altitude, velocity, time, and weight. The angle-of-attack comparison, Figure 7.33, show a very small difference of commanded angle-of-attack throughout the fight, up until the last 20 seconds. That time frame is the portion of the algorithm where the last open-loop solution is used and commands are interpolated from that solution. Any difference here is attributed to the interpolation scheme. Additionally, this short duration accounts for part of the differences in final altitude, velocity, and weight. Finally, since dynamic pressure was not a constraint, there is no portion that shows an "activation period" in Figures 7.34 and 7.35.

Table 7.6 Closed-loop Simulation with No Constraints

Final Altitude, ft	Final Velocity, ft/s	Final Time, s	Final Weight, lbs
130,000	14,000	179.6	234,450
130,072	14,010	179.6	234,356

7.2.2 Constrained Closed-loop Simulations

When incorporating the dynamic pressure constraint, one needs to be careful how the throttle is determined. In Section 4.1.5.1, it is shown that dynamic pressure is regulated by a throttle command, η. However, this is assuming that thrust is linear with throttle, $T_{new} = \eta(t)T_0$, where T_{new} is the desired thrust after the constraint is enforced, and T_0 is the thrust portion not associated with the throttle. When compared to the GHAME engine model, the thrust is not linear with throttle, ϕ_t, since I$_{sp}$ is a function of ϕ_t. For closed-loop simulations, the GHAME engine throttle is determined by employing a root finding algorithm. First the desired thrust is found using the dynamic pressure regulator and the root finding code finds the necessary throttle, ϕ_t, to match the desired thrust.

The following table and figures depict several runs with various constraints activated. Initial altitude is 85,000 feet, initial velocity is 5,500 ft/s, while final altitude is 130,000 ft, final velocity is 16,000 ft/s, final inclination is 51.6 °, and final flight path angle is 0 °.

Table 7.7 Closed-loop Simulation with Constraints

Final Time, s	Final Weight, lbs	Constraint
267.3	214,250	None
258.9	214,400	$\alpha = 8.25\,^\circ$
266.0	214,150	$\alpha = 8.75\,^\circ$
258.9	213,040	$\alpha = 8.25\,^\circ$, $\bar{q} < 1000$ psf
267.3	213,840	$\bar{q} < 1000$ psf

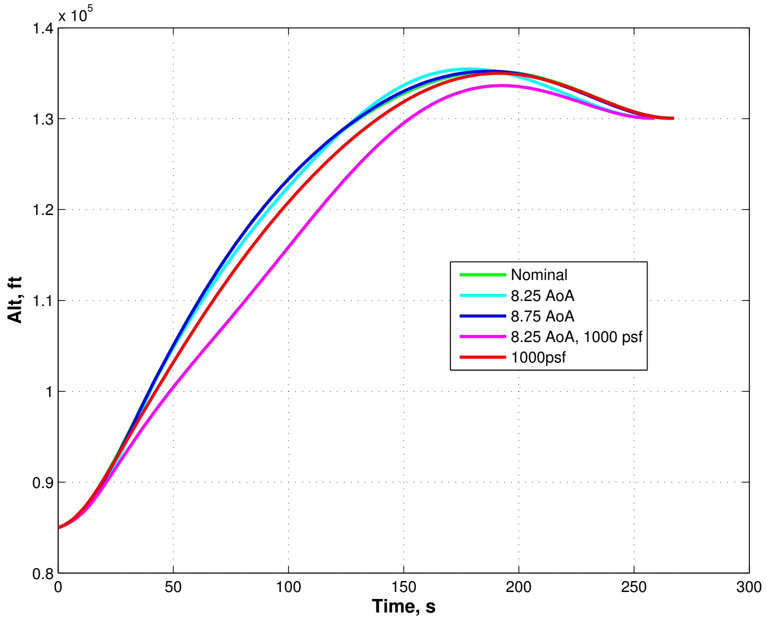

Figure 7.36 Closed-loop Simulation with Constraints - Altitude Comparison

The figures show that all constraints are met for the various simulations. From the altitude and velocity comparisons, Figures 7.36 and 7.37, the profiles with the largest difference are the one that include the dynamic pressure constraint. The adjustment to throttle early in flight prevents the vehicle form gaining speed and altitude when compared to the other simulations. From the data in Table 7.7, the final weight is effected by the dynamic pressure constraint while the final time is effected by the angle-of-attack constraint. The angle-of-attack effecting the final time was seen in the open-

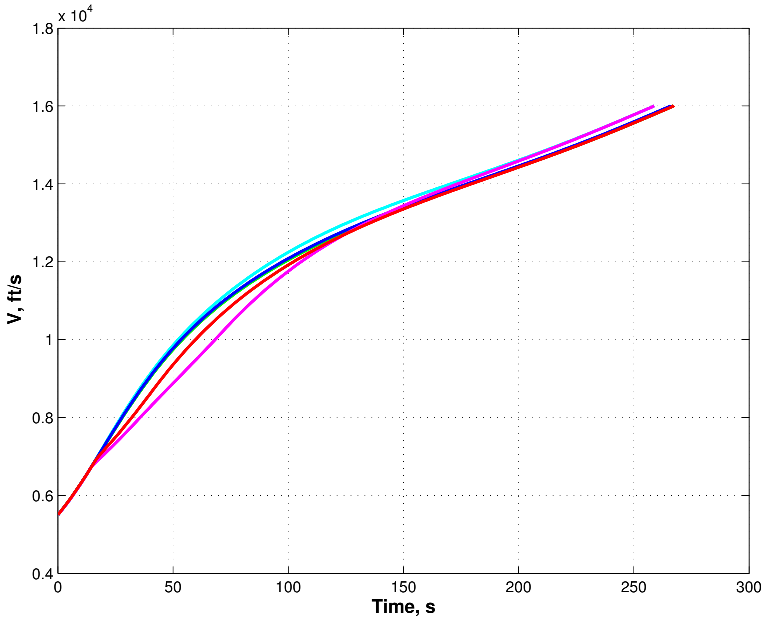

Figure 7.37 Closed-loop Simulation with Constraints - Velocity Comparison

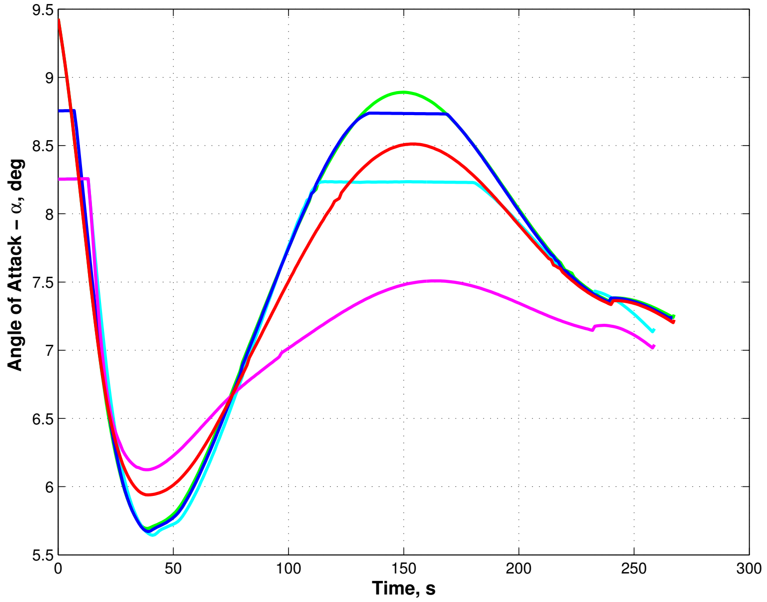

Figure 7.38 Closed-loop Simulation with Constraints - Angle-of-Attack Comparison

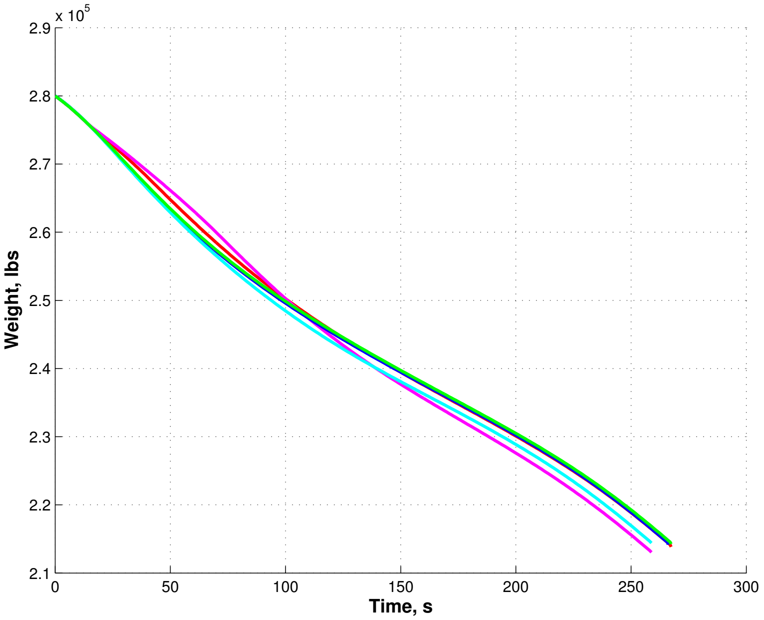

Figure 7.39 Closed-loop Simulation with Constraints - Weight Comparison

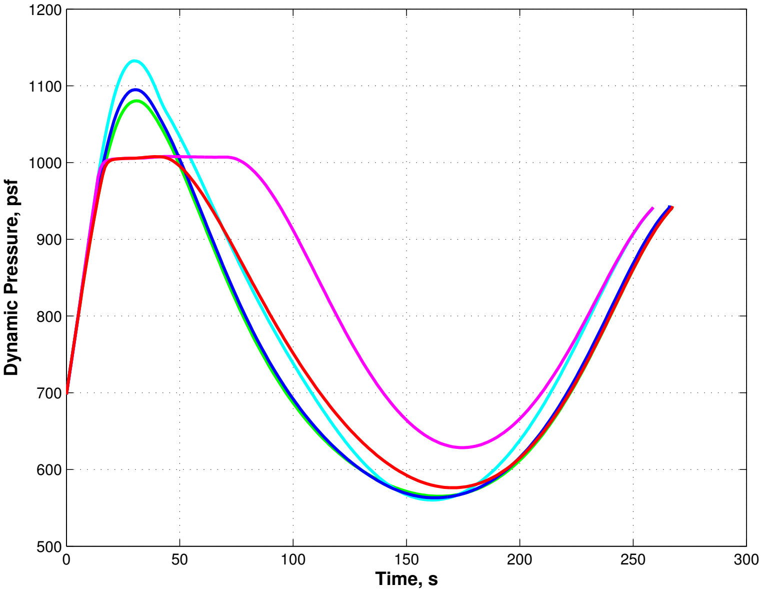

Figure 7.40 Closed-loop Simulation with Constraints - Dynamic Pressure Comparison

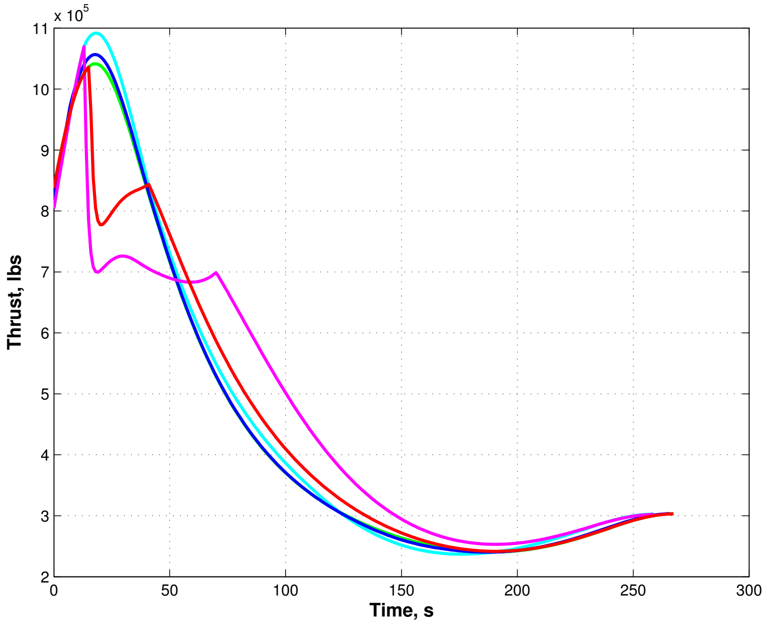

Figure 7.41 Closed-loop Simulation with Constraints - Thrust Comparison

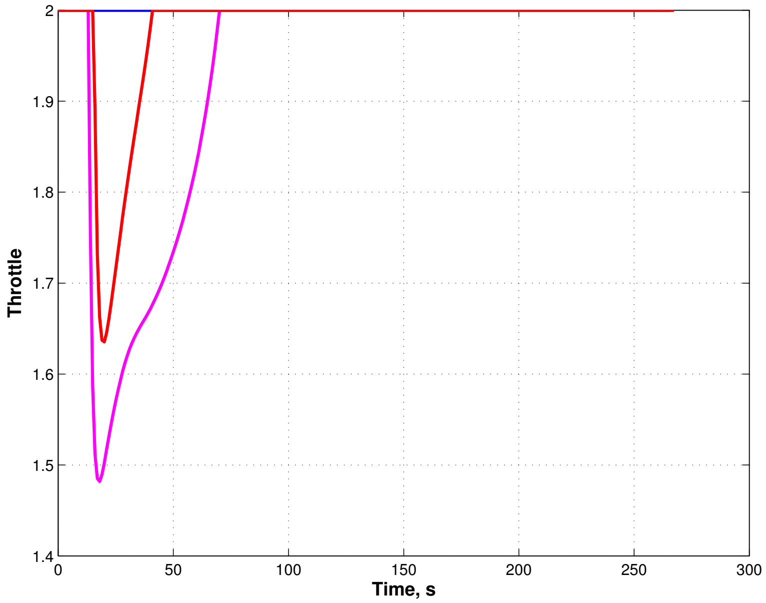

Figure 7.42 Closed-loop Simulation with Constraints - Throttle Comparison

loop results. The dynamic pressure constraint effecting final mass can be explained by the lowered throttle setting. The reduced throttle prevented the vehicle from gaining the altitude as quickly, as seen in Figure 7.36. Since the vehicle is at lower altitudes during most of the flight, density is higher, and therefore thrust is higher during the portion of flight when throttle is set to the maximum value. The result is an increased mass rate and lower final weight.

An additional comment is needed in regards to the dynamic pressure constraint. The throttle command, η, in Eq. (4.80) contains a user selected parameter, δ. From various simulations, it was noted that a value too small would cause the throttle command to jitter. When considering the throttle bandwidth, it would be safe to assume that rapid changing commands would be unattainable by the engine. Too large of a value would result in over control of the throttle and extending the time of flight as well as increased fuel usage. It was observed that dimensional values for δ between 1.5s and 20s allowed the throttle to be adjusted properly. The value of δ used in Eq. (4.80) is nondimensional, so the values $1.5s < \delta < 20s$ need to be nondimensionalized.

7.2.3 Atmospheric and Vehicle Model Perturbed Solutions

7.2.3.1 Atmospheric Model Perturbations

In any given launch there are a multitude of disturbances that cannot be modeled exactly. The ability for a guidance algorithm to handle these disturbance is critical to the success of the algorithm. To test the robustness, atmospheric, engine, and aerodynamic model perturbations are done. The same initial and final conditions are used for each run. For the first set of solutions, only the atmospheric density is varied. Initial altitude is 85,000 ft, initial velocity is 5,500 ft/s, initial weight is 280,000 lbs, final altitude is 130,000 ft, final velocity is 14,000 ft/s, final inclination is 51.6 °, and final flight path angle is 0 °.

Table 7.8 Closed-loop Simulation with Density Perturbations

Final Time, s	Final Weight, lbs	Atmosphere
179.6	234,360	No Variation
195.4	235,480	10% decrease
185.4	234,960	5% decrease
181.2	234,530	2% decrease
178.9	234,140	2% increase
179.6	233,620	5% increase
186.2	232,700	10% increase

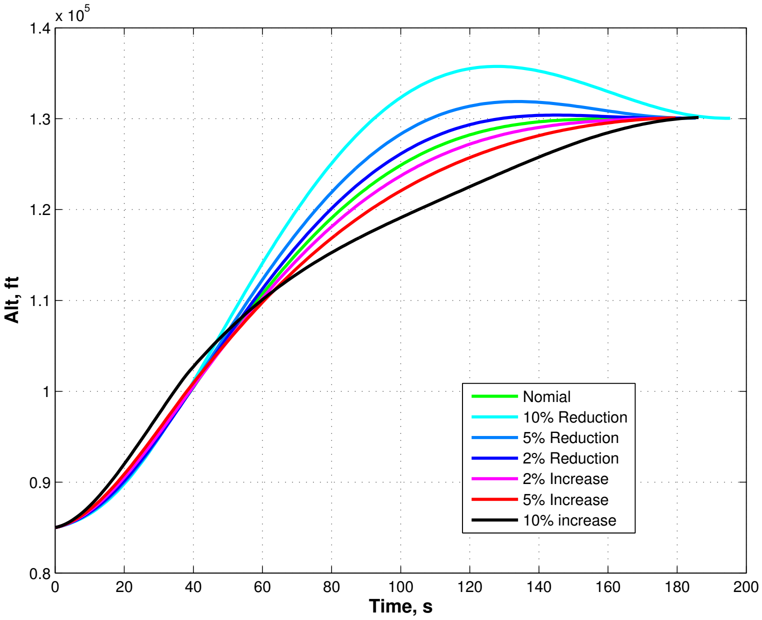

Figure 7.43 Closed-loop Simulation with Density Perturbations - Altitude Comparison

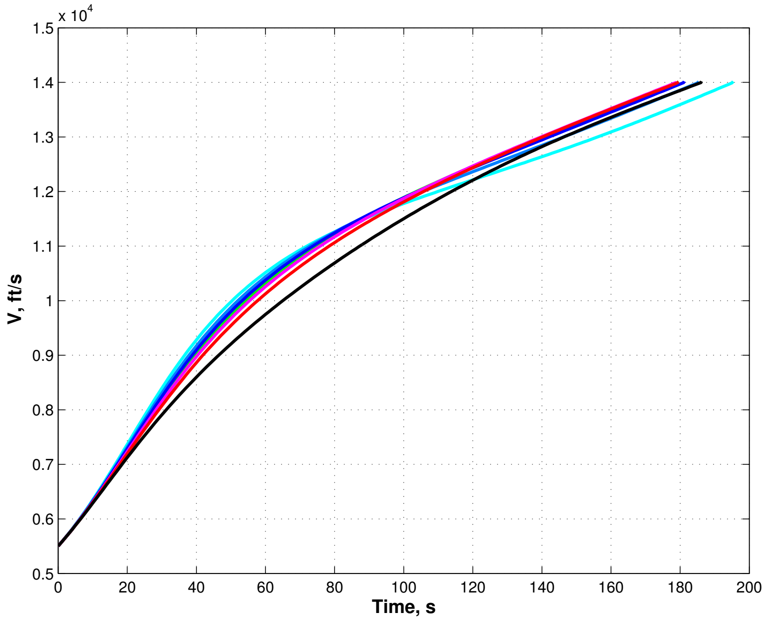

Figure 7.44 Closed-loop Simulation with Density Perturbations - Velocity Comparison

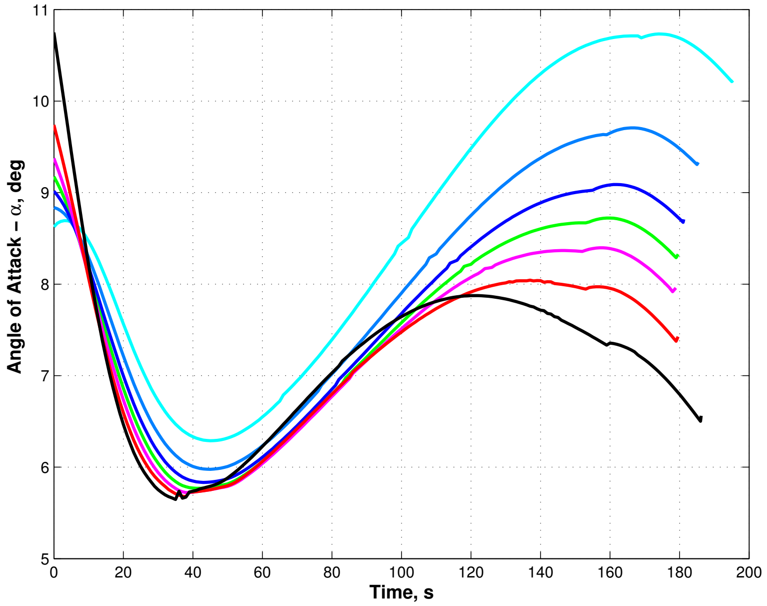

Figure 7.45 Closed-loop Simulation with Density Perturbations - Angle-of-Attack Comparison

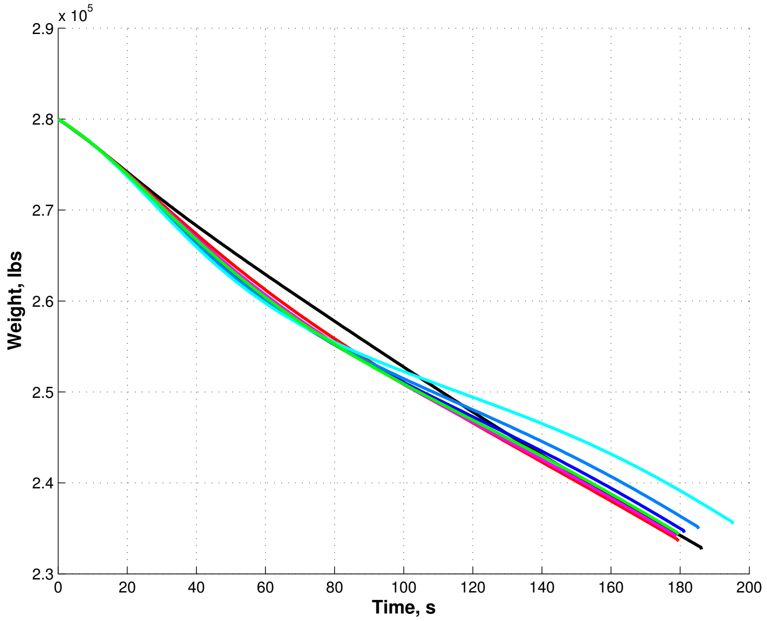

Figure 7.46 Closed-loop Simulation with Density Perturbations - Weight Comparison

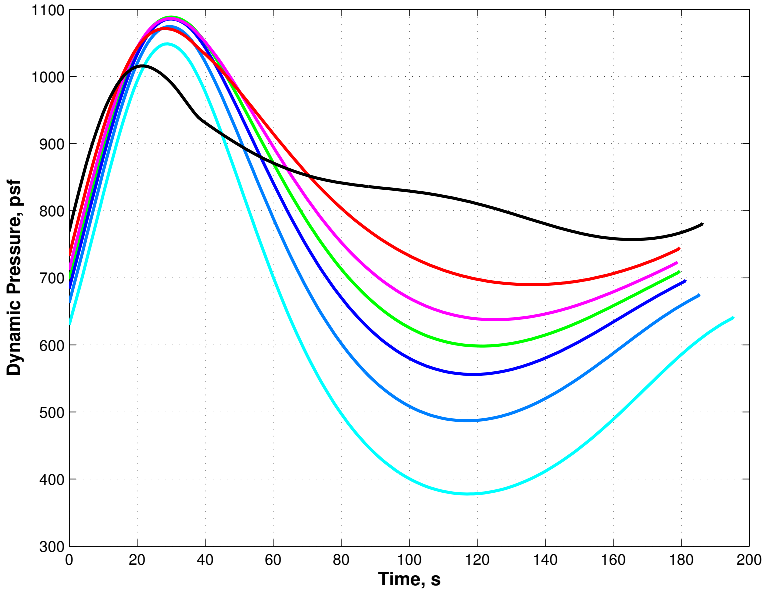

Figure 7.47 Closed-loop Simulation with Density Perturbations - Dynamic Pressure Comparison

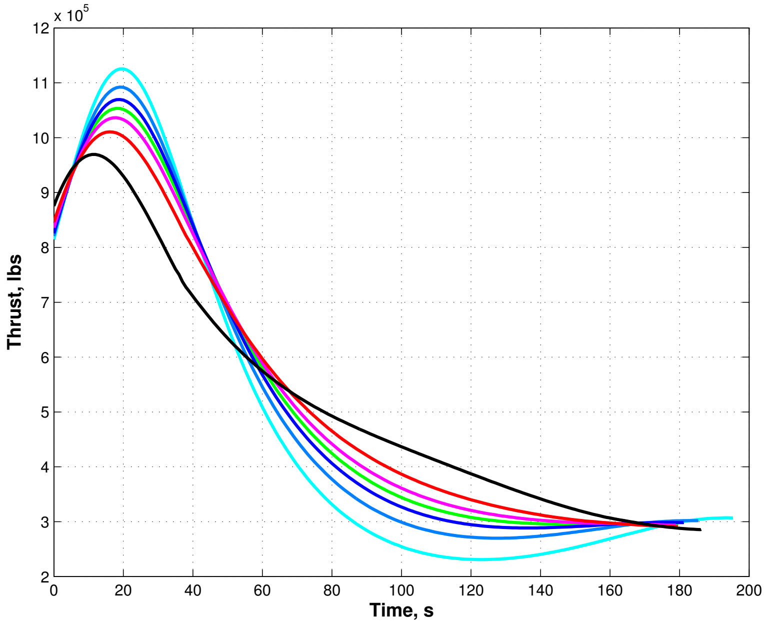

Figure 7.48 Closed-loop Simulation with Density Perturbations - Thrust Comparison

The variation in density are shown in Table 7.8. When the density is decreased the final time begins to increase. Also shown is a decrease in the fuel usage (i.e. an increase in final weight). This is to be expected since thrust decreases due to the reduction in density, which results in a lowered mass rate. The reduced thrust then requires the vehicle to fly longer to meet the final requirements.

When the density is increased by small percentage, the final time has a slight decreases. The cause can be associated to an increase in thrust as a result of the density rise. The 5% increase results in a final time similar with the nominal case, but with an increase in fuel usage. Since density was increased, mass rate would increase due to the rise in thrust. With the 10% increase in density, the final time is longer than the nominal case and the final weight is lower. Although thrust would be larger due to the increase in density, drag would also increase. Both Figures 7.43 and 7.44 show that the increase in drag effects the altitude and velocity profiles. The reduced acceleration requires the vehicle to fly for a longer duration. This longer duration coupled with the increased thrust results in more fuel being consumed.

For comparison, open-loop simulations were done with the upper and lower extreme cases. The simulation found the optimal solution using nominal conditions and use the generated body axis commands. The density was then perturbed and no corrections were made to the commands to adjust for these variations. Initial conditions for these simulations were: initial altitude is 85,000 ft; initial velocity is 5,500 ft/s; initial weight is 280,000 lbs. Final conditions desired were: final altitude is 130,000 ft; final velocity is 14,000 ft/s; final inclination is 51.6 °; final flight path angle is 0 °. Only the final altitude and velocity are presented to illustrate the differences.

Table 7.9 list a few of the final states and variables resulting from the simulations. Figures 7.49 - 7.52 show the resulting trajectory profiles.

Table 7.9 Open-loop Simulation with Density Perturbations

Final Time, s	Final Weight, lbs	Final Altitude, ft	Final Velocity, ft/s	Density
179.6	234,360	130,060	14,010	No Variation
179.6	232,550	130,410	14,370	10% decrease
179.6	236,420	129,400	13,620	10% increase

The table shows that the final times are all identical, this is due to the simulations being ran open-loop. Final weight for the decreased density case was about 1,800 pounds lower, final atlitude was higher than desired, as well as final velocity. Since the density was lower than expected, drag was lower. This allowed the vehicle to gain speed faster, as shown in the altitude and velocity profiles. The final weight was much lower due to velocity. Thrust is linearly dependent on velocity (Eq. (7.1)), and since velocity is higher it resulted in a higher mass rate, even though the lowered density would account for some lost of thrust.

For the case where density was increased, final altitude was lower than expected as well as final velocity. This again was due to the drag. Since density was increased, drag was larger preventing the vehicle from gaining speed and altitude. This resulted in

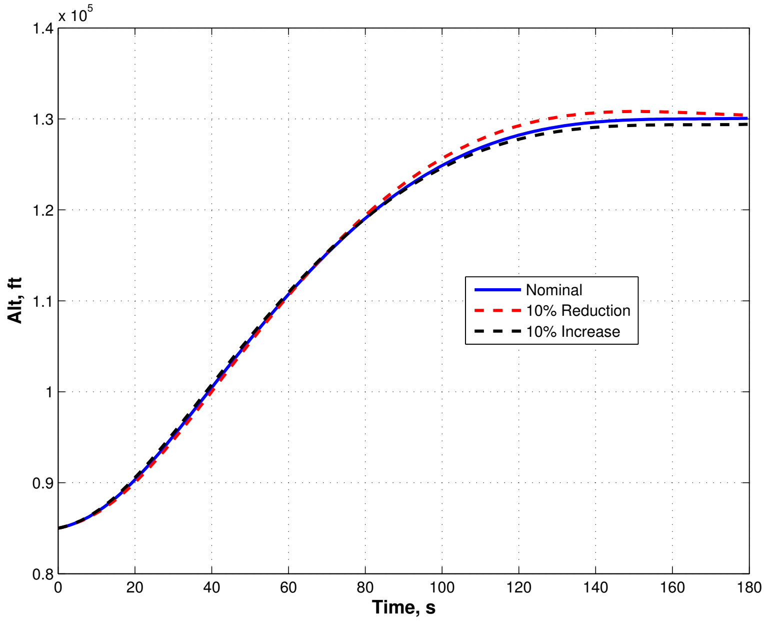

Figure 7.49 Open-loop Simulation with Density Perturbations - Altitude Comparison

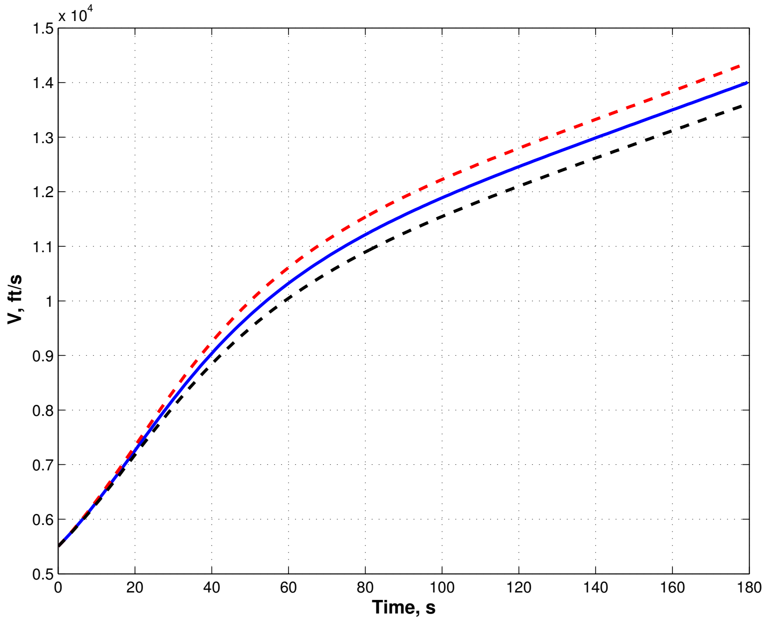

Figure 7.50 Open-loop Simulation with Density Perturbations - Velocity Comparison

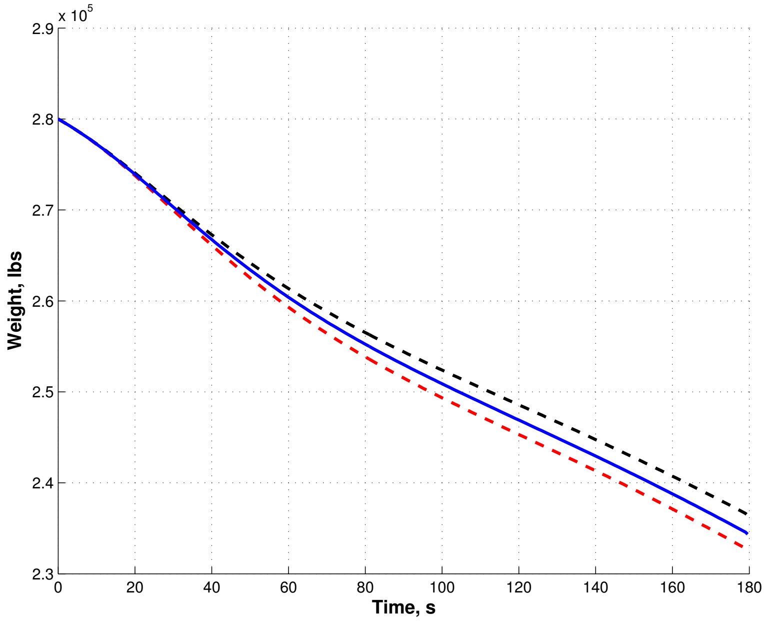

Figure 7.51 Open-loop Simulation with Density Perturbations - Weight Comparison

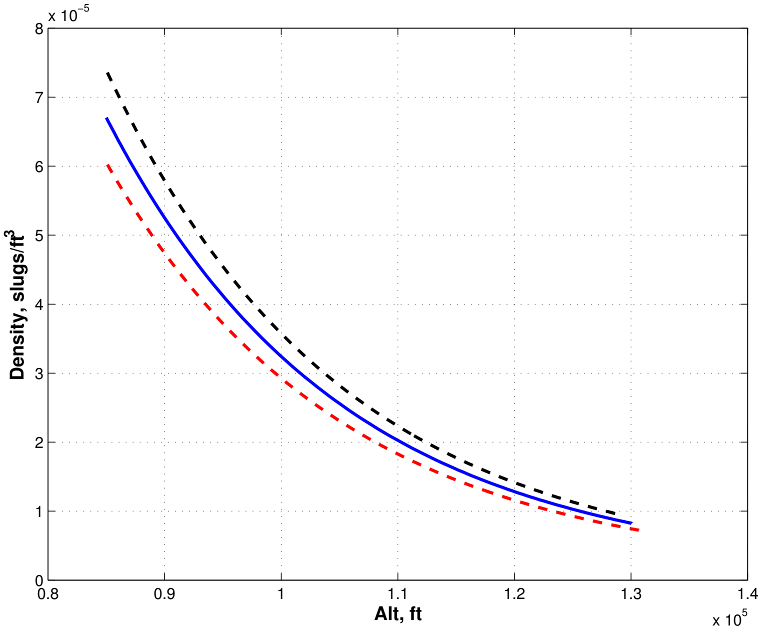

Figure 7.52 Open-loop Simulation with Density Perturbations - Density Comparison

the vehicle lower the targeted altitude and velocity. Also, since velocity was lower, this resulted in a lower thrust and mass rate, leading to the larger final weight.

7.2.3.2 Thrust Model Perturbations

The following table and figures represent solutions to the thrust model perturbed solutions. The initial altitude is 85,000 ft, initial velocity is 5,500 ft/s, initial weight is 280,000 lbs, final altitude is 130,000 ft, final velocity is 14,000 ft/s, final inclination is 51.6 °, and final flight path angle is 0 °. The total thrust is adjusted by some factor.

Table 7.10 Closed-loop Simulation with Thrust Perturbations

Final Time, s	Final Weight, lbs	Thrust
179.6	234,360	No Variation
193.9	232,510	10% decrease
180.3	233,420	5% decrease
187.0	235,160	5% increase
197.1	235,510	10% increase
216.1	236,290	20% increase

The data shows that as the thrust is reduced, the final time is longer than nominal while final weight is decreased. This can be explained by the fact that the lower thrust keeps the vehicle from accelerating and requires longer time to meet the final requirements, as evident in Figure 7.54. Additionally, the vehicle must remain at lower altitudes to keep thrust as large as possible. The longer flight time coupled with the lower altitude allows mass rate to be larger and results in an increase use of fuel.

As the thrust increases, the final time continues to grow, but final weight is larger (less fuel is required). The altitude profile, Figure 7.53, shows that the thrust increase causes the vehicle to have a large overshoot. Since the vehicle has increased thrust, the solution takes the vehicle to the upper atmosphere to keep the mass rate low. Since the total distance traveled is much larger than the nominal cause, the final time is increased. However, since the vehicle is experiencing lower density, the mass rate is kept low and

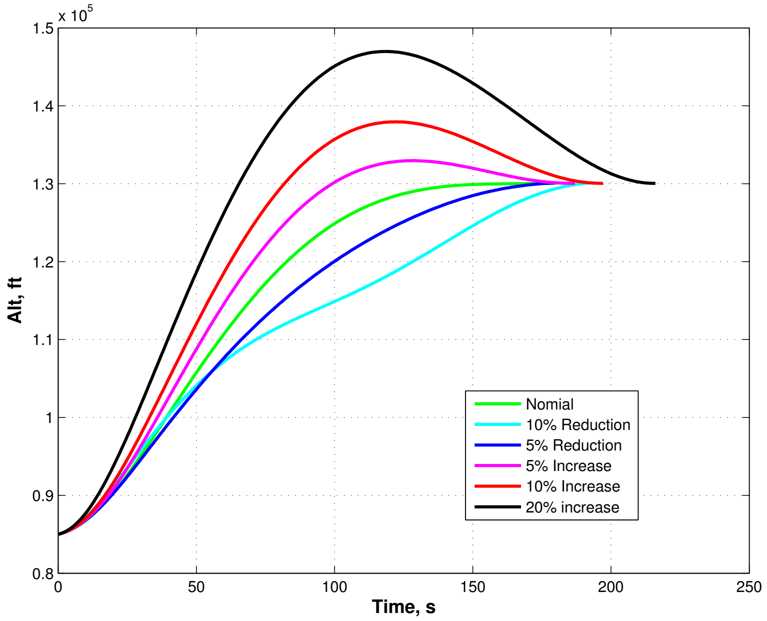

Figure 7.53 Closed-loop Simulation with Thrust Perturbations - Altitude Comparison

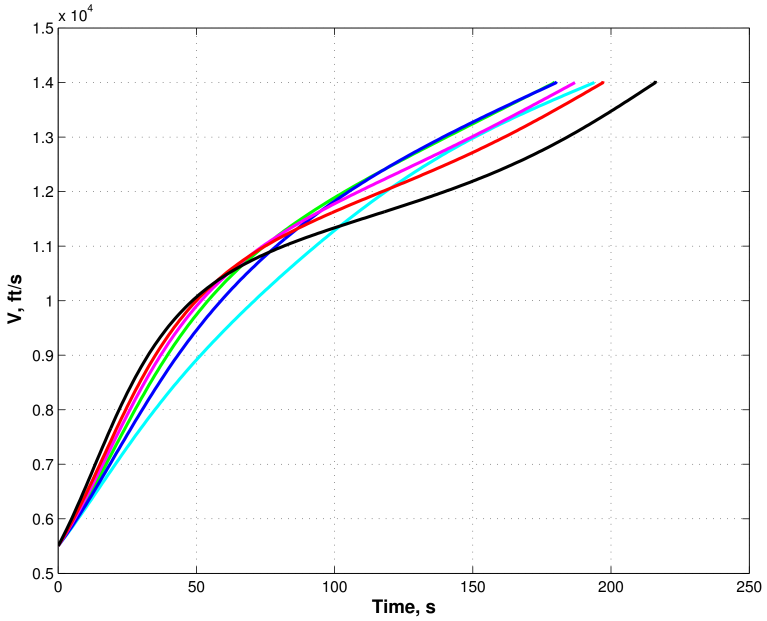

Figure 7.54 Closed-loop Simulation with Thrust Perturbations - Velocity Comparison

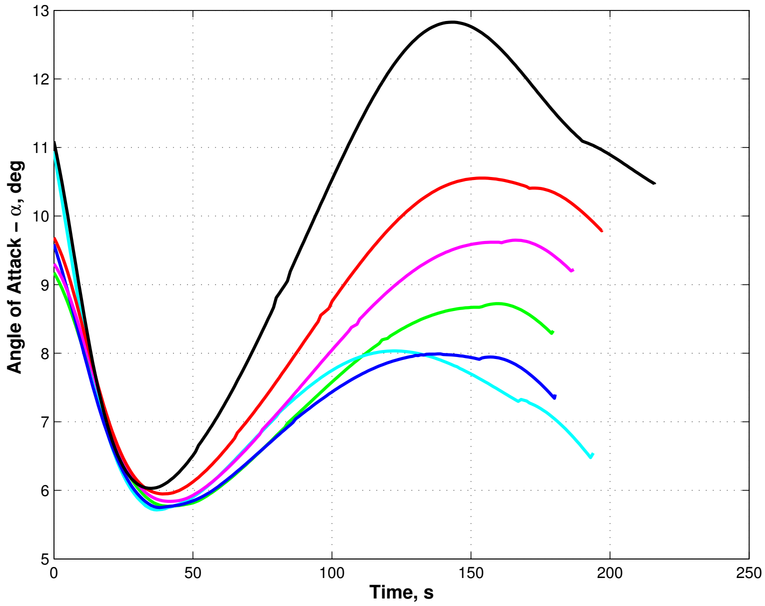

Figure 7.55 Closed-loop Simulation with Thrust Perturbations - Angle-of-Attack Comparison

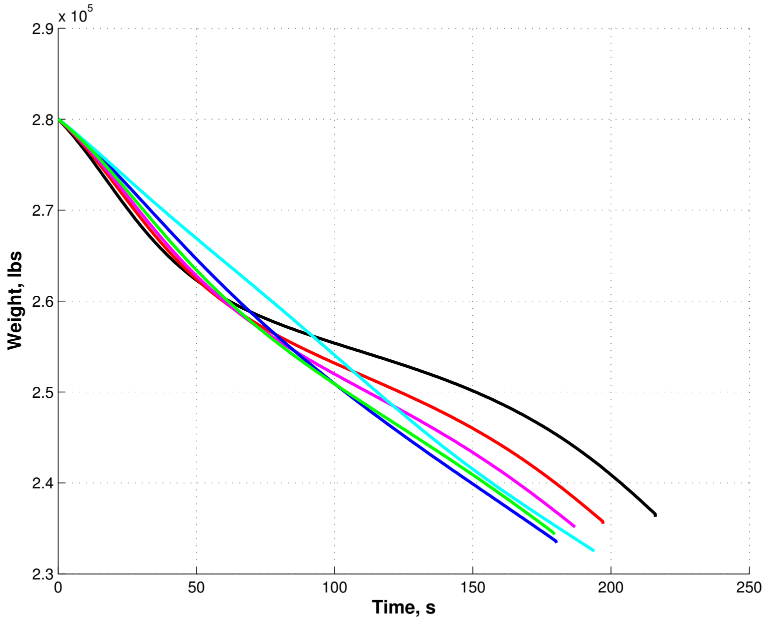

Figure 7.56 Closed-loop Simulation with Thrust Perturbations - Weight Comparison

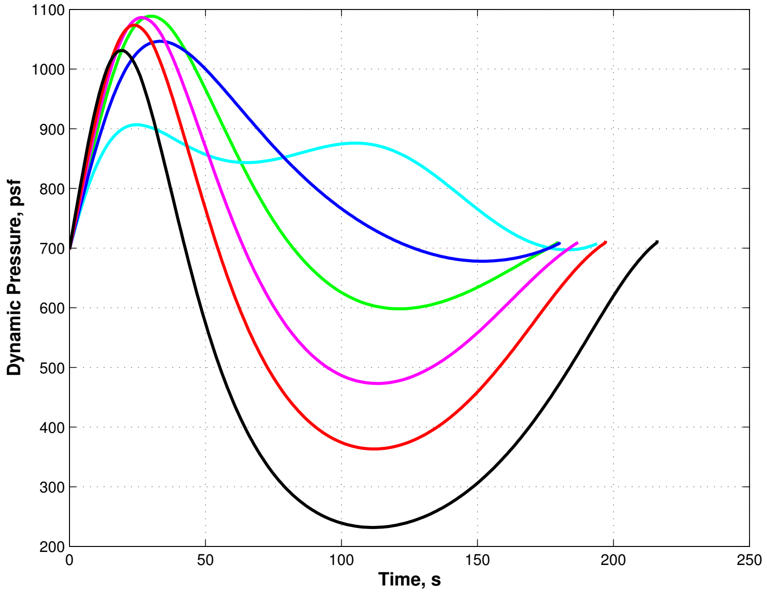

Figure 7.57 Closed-loop Simulation with Thrust Perturbations - Dynamic Pressure Comparison

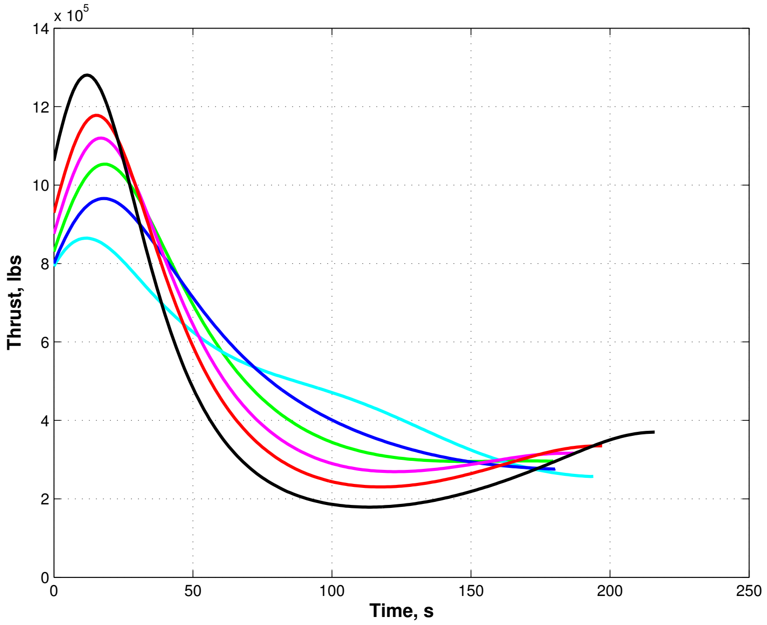

Figure 7.58 Closed-loop Simulation with Thrust Perturbations - Thrust Comparison

results in a larger final weight.

Again, open-loop simulations were done with the upper and lower extreme cases. The simulations were ran using the commands from a nominal case but the engine model is perturbed to generate the trajectory profile. Initial conditions for these simulations were: initial altitude of 85,000 ft; initial velocity of 5,500 ft/s; initial weight of 280,000 lbs. Final conditions desired were: final altitude of 130,000 ft; final velocity of 14,000 ft/s; final inclination of 51.6 °; final flight path angle of 0 °. As before, only the final altitude and velocity are presented to show the differences.

Table 7.11 Open-loop Simulation with Thrust Perturbations

Final Time, s	Final Weight, lbs	Final Altitude, ft	Final Velocity, ft/s	Thrust
179.6	234,360	130,060	14,010	No Variation
179.6	236,560	126,620	13,570	10% decrease
179.6	231,690	135,700	14,620	20% increase

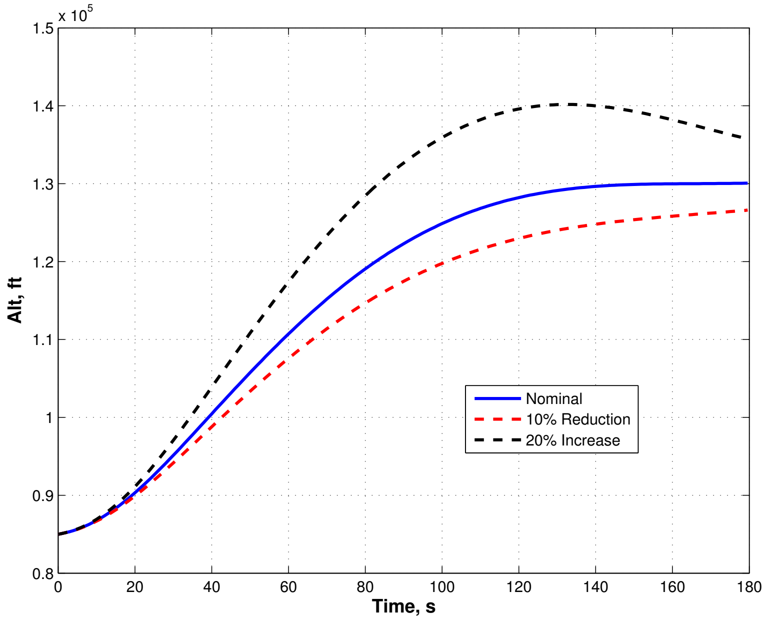

Figure 7.59 Open-loop Simulation with Thrust Perturbations - Altitude Comparison

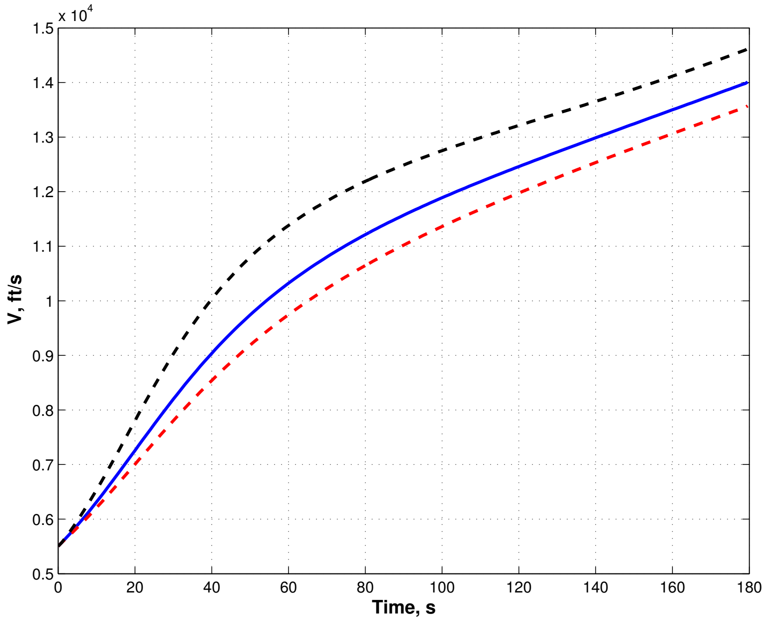

Figure 7.60 Open-loop Simulation with Thrust Perturbations - Velocity Comparison

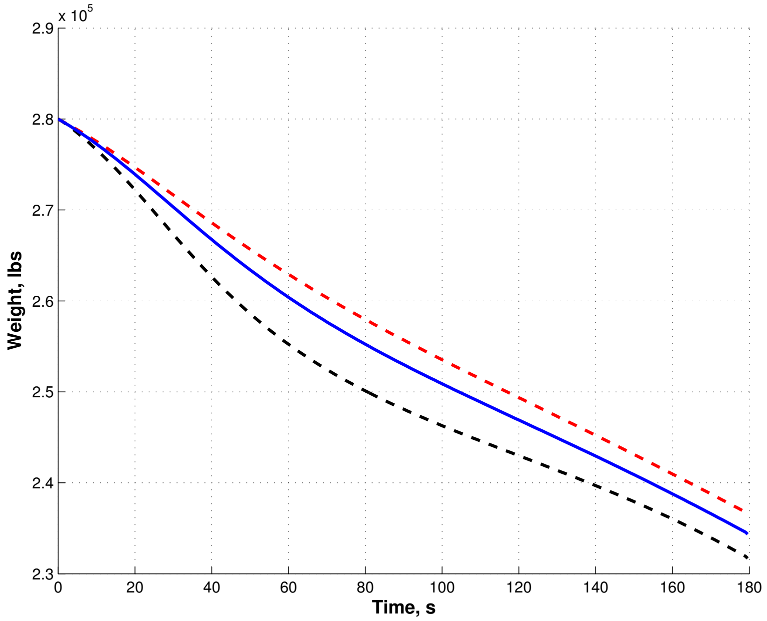

Figure 7.61 Open-loop Simulation with Thrust Perturbations - Weight Comparison

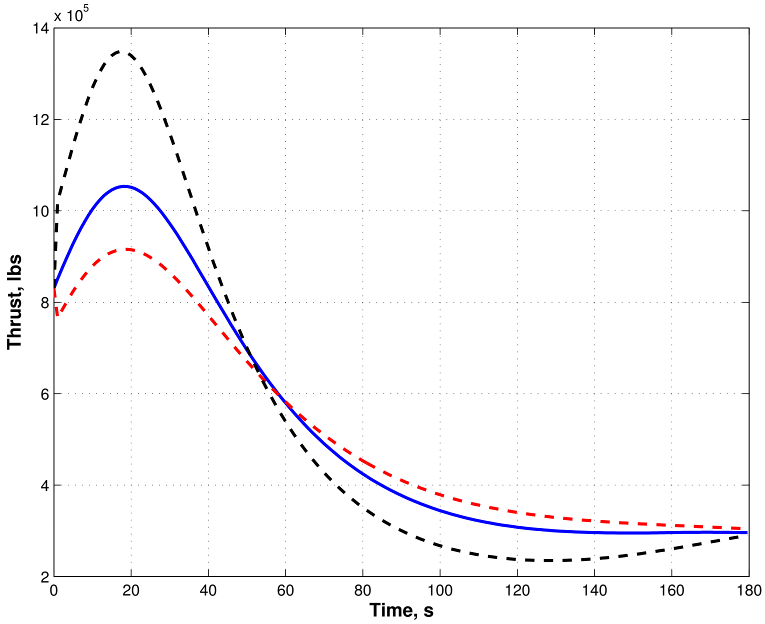

Figure 7.62 Open-loop Simulation with Thrust Perturbations - Thrust Comparison

From Table 7.11, the decrease in thrust results in the vehicle not achieving both the final altitude and velocity requirement. Because thrust is lower, the vehicle cannot gain the necessary speed or altitude. Additionally, since thrust is lower, mass rate is lower resulting in the final weight to be higher at the end of the simulation as compared to the nominal case. The increase in thrust show the vehicle ending at a much higher altitude and faster velocity that desired. Additionally, the increase in thrust causes the final weight to be significantly lower. Figures 7.59 to 7.62 plot the resulting trajectories.

7.2.3.3 Aerodynamic Model Perturbations

The following table and figures represent solutions to perturbations of the GHAME aerodynamic model. The initial altitude is 85,000 ft, initial velocity is 5,500 ft/s, initial weight is 280,000 lbs, final altitude is 130,000 ft, final velocity is 14,000 ft/s, final inclination is 51.6 °, and final flight path angle is 0 °. The lift coefficient C_L (repeated in

Eq. (7.4)) is varied by multipling C_{L_0} by some factor.

$$C_L = C_{L_0}(M_a, \alpha) + C_{L_\alpha}(M_a, \alpha)\alpha + C_{L_{\delta e}}(M_a, \alpha)\delta e \tag{7.4}$$

Table 7.12 Closed-loop Simulation with Aerodynamic Perturbations

Final Time, s	Final Weight, lbs	C_{L_0}
179.6	234,360	No Variation
204.0	234,550	10% decrease
192.9	234,590	5% decrease
163.7	234,890	5% increase
148.7	234,070	10% increase

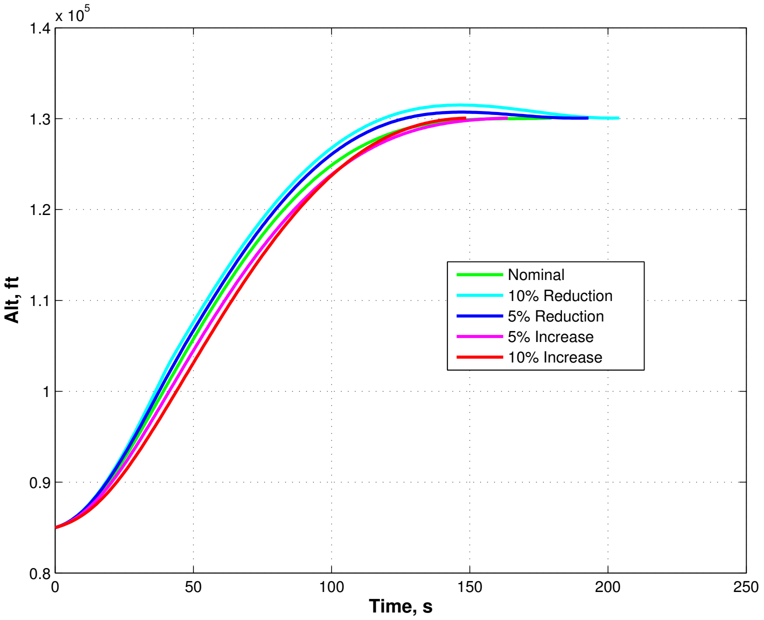

Figure 7.63 Closed-loop Simulation with Aerodynamic Perturbations - Altitude Comparison

The data in Table 7.12 show as C_{L_0} is decreased, final time increases. Additionally, when observing Figure 7.63, the decrease in C_{L_0} causes the vehicle to overshoot final altitude. This can be explained by observing the total lift coefficient, C_L, in Figure 7.69. Notice that the decrease in C_{L_0} causes C_L to increase. This is because C_{L_0} is negative,

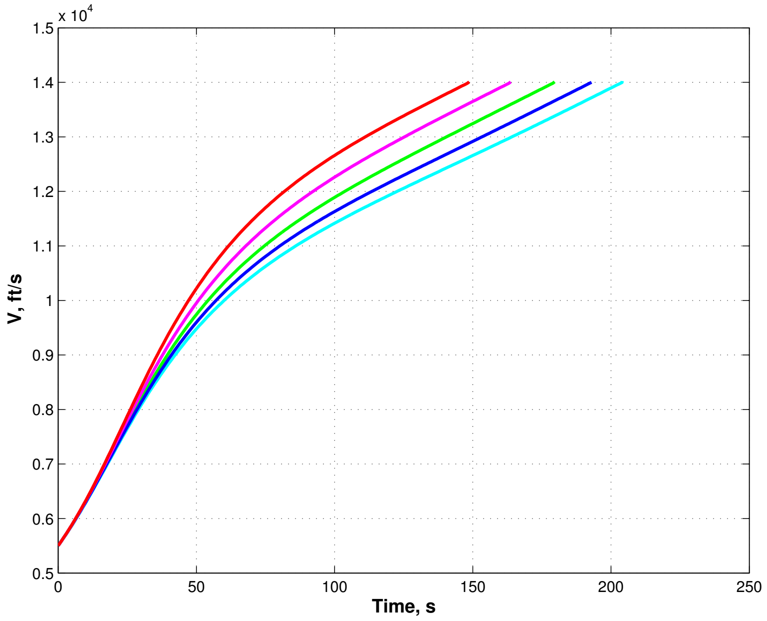

Figure 7.64 Closed-loop Simulation with Aerodynamic Perturbations - Velocity Comparison

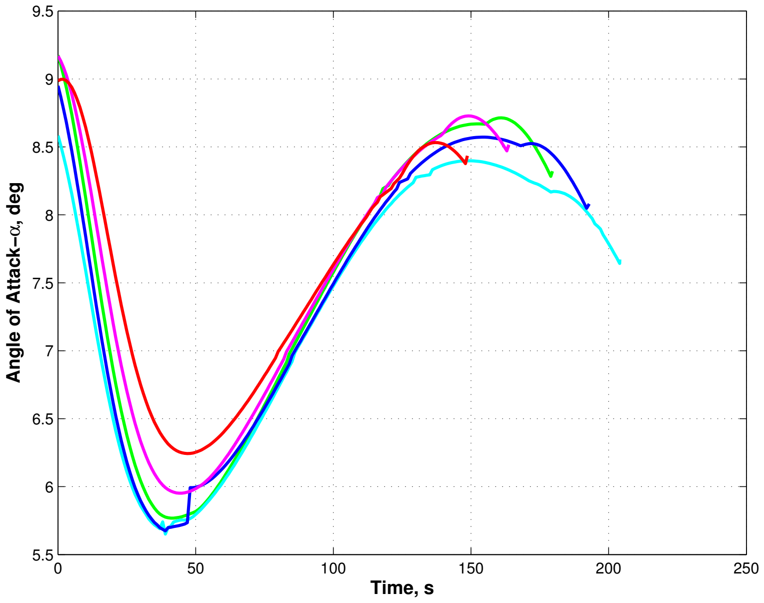

Figure 7.65 Closed-loop Simulation with Aerodynamic Perturbations - Angle-of-Attack Comparison

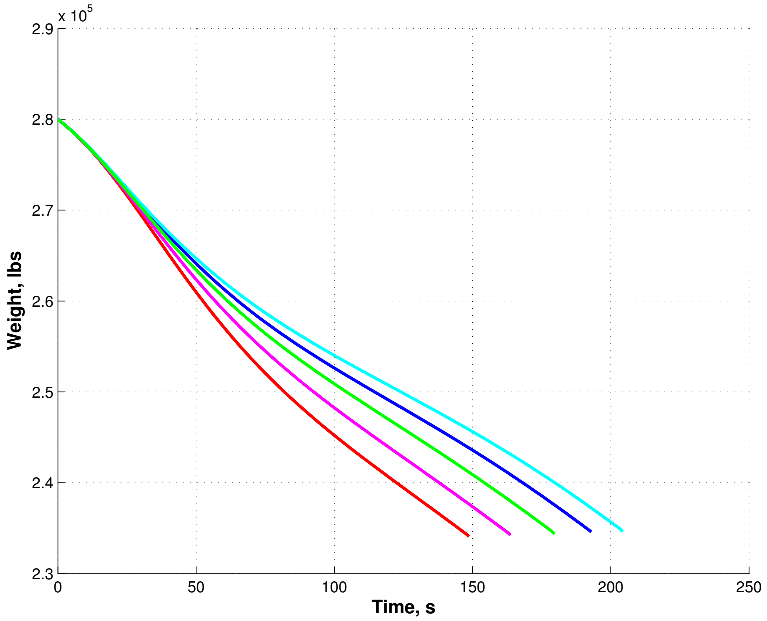

Figure 7.66 Closed-loop Simulation with Aerodynamic Perturbations - Weight Comparison

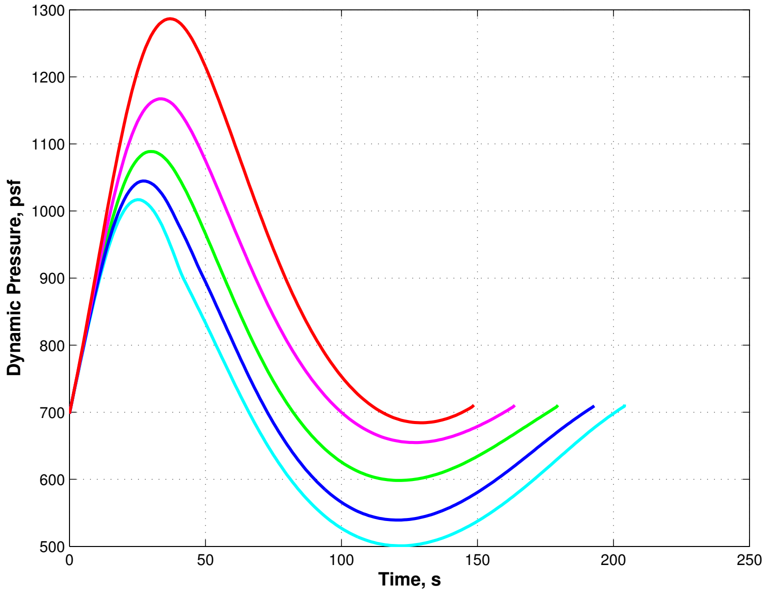

Figure 7.67 Closed-loop Simulation with Aerodynamic Perturbations - Dynamic Pressure Comparison

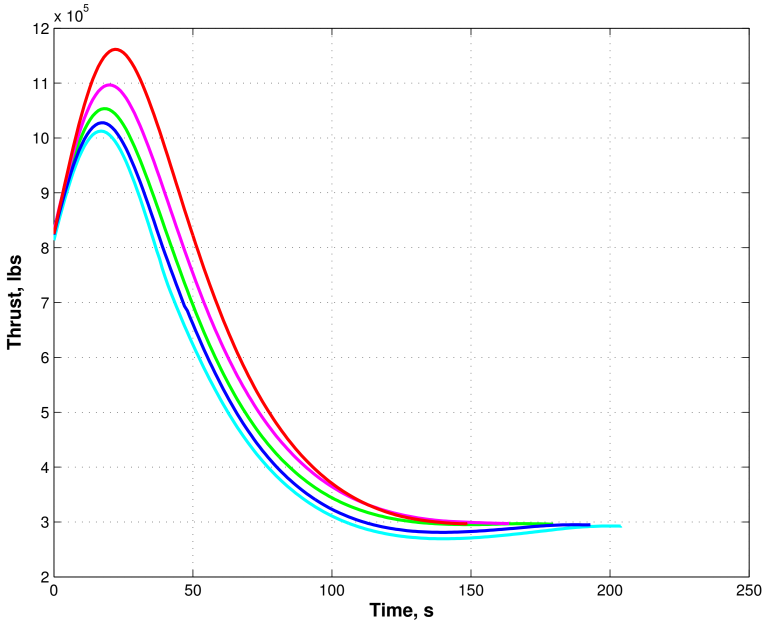

Figure 7.68 Closed-loop Simulation with Aerodynamic Perturbations - Thrust Comparison

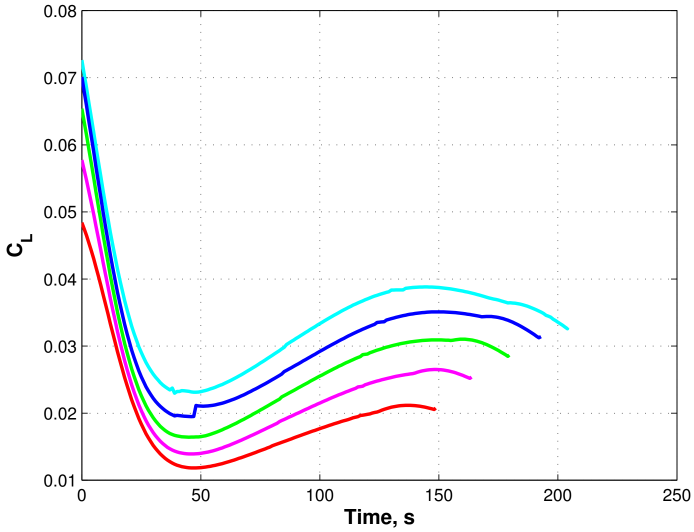

Figure 7.69 Closed-loop Simulation with Aerodynamic Perturbations - C_L Comparison

so a reduction causes the overall lift to increase. The increase in lift allows the vehicle to gain altitude quicker, but does not provide any way of increasing velocity. Additionally, the increase in altitude reduces the density and will negatively effect the thrust generated. The solution requires the final time to be longer to achieve the final velocity requirement. As C_{L_0} is increased, the opposite occurs. Total lift is decreased, allowing the vehicle to stay lower in the atmosphere. This allows the thrust to be larger and the vehicle achieving the final altitude and velocity requirements sooner.

For completeness, the simulations were conducted open-loop for the two extreme perturbed cases. Simulations were ran using commands generated from a nominal case but the aerodynamic model is changed for the simulation. Initial conditions were: initial altitude is 85,000 ft; initial velocity is 5,500 ft/s; initial weight is 280,000 lbs. Final conditions desired were: final altitude is 130,000 ft; final velocity is 14,000 ft/s; final inclination is 51.6 °; final flight path angle is 0 °. For comparison purposes, only final altitude and velocity are presented to show difference between closed-loop and open-loop simulations.

Table 7.13 Open-loop Simulation with Aerodynamic Perturbations

Final Time, s	Final Weight, lbs	Final Altitude, ft	Final Velocity, ft/s	C_{L_0}
179.6	234,360	130,060	14,010	No Variation
179.6	240,710	129,920	13,300	10% decrease
179.6	225,750	130,450	14,870	10% increase

Table 7.13 shows that the decreased C_{L_0} resulted in lower altitude and slower velocity than desired. Since C_{L_0} was lowered, the total lift, Figure 7.73, increased. This increase in lift allows the vehicle to gain altitude quickly but does allow velocity to increase. The altitude plot, Figure 7.70, shows the vehicle achieving the final altitude near 120 seconds into the flight, but then the vehicle has a negative flight path angle and falls below the required altitude at the end of the simulation. Since the vehicle was higher than the

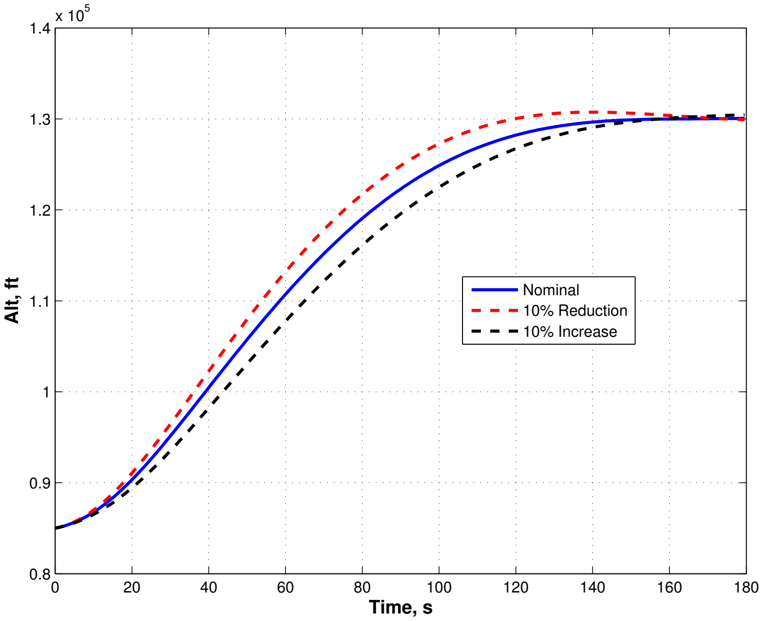

Figure 7.70 Open-loop Simulation with Aerodynamic Perturbations - Altitude Comparison

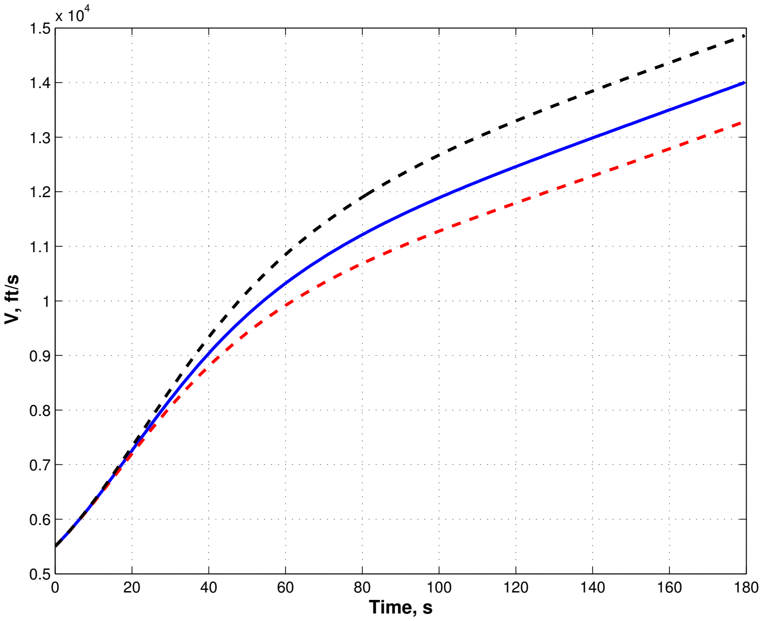

Figure 7.71 Open-loop Simulation with Aerodynamic Perturbations - Velocity Comparison

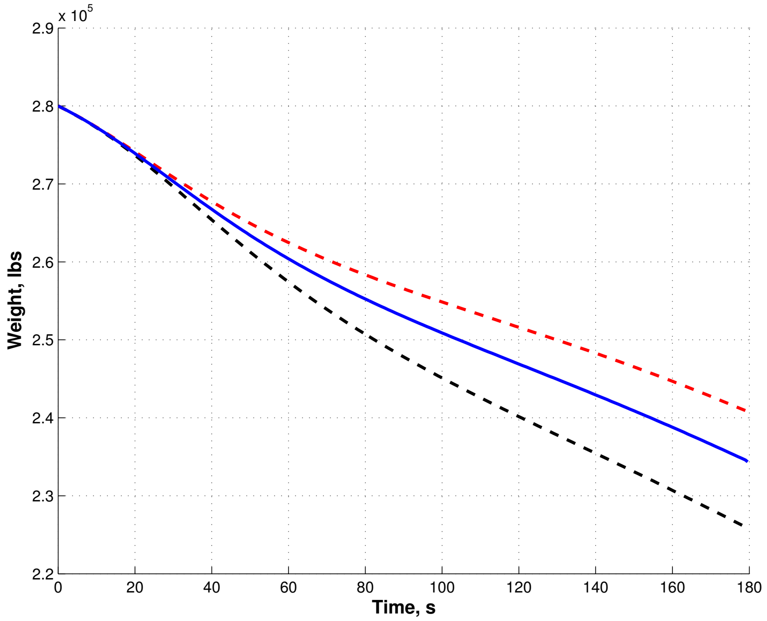

Figure 7.72 Open-loop Simulation with Aerodynamic Perturbations - Weight Comparison

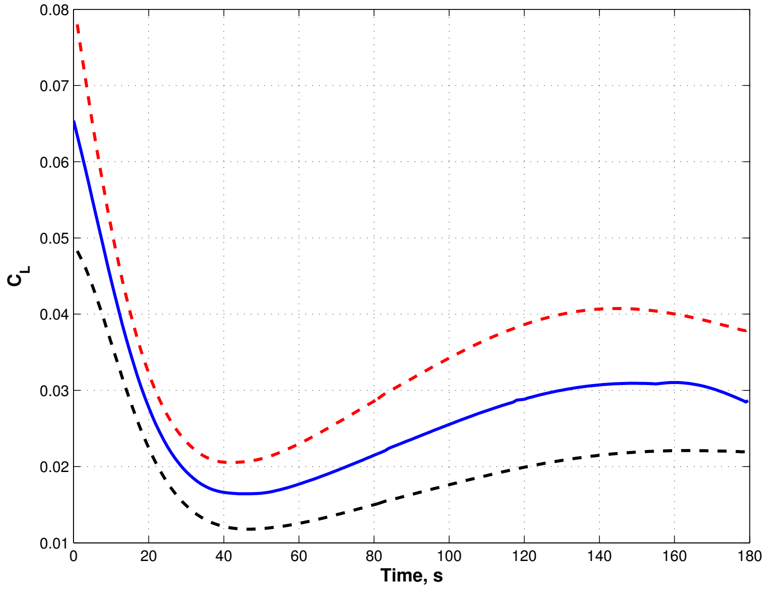

Figure 7.73 Open-loop Simulation with Aerodynamic Perturbations - C_L Comparison

nominal trajectory, the density was lower and therefore mass rate was lower. This would result in a higher final weight. With C_{L_0} increasing, total lift would be decreased. Since the vehicle flew lower than the nominal, the vehicle was able to gain higher speeds due to the increased density. This caused the vehicle to have a larger velocity than desired at the of the simulation. Additionally, the final weight was much lower due to the increase in density.

7.2.3.4 Varying Atmospheric Model Perturbations

Next, a simulation was conducted using a perturbations that were varied over the entire trajectory. To this point, only constant perturbations were used. Density was varied using the following equation,

$$\rho = \left(1 + 0.2\sin(2\pi h_{km}/15)\right)\rho^* \tag{7.5}$$

where h_{km} is the altitude in kilometers, and ρ^* is the nominal density at the given condition. The simulation was ran with initial altitude at 85,000 ft, initial velocity at 5,500 ft/s, and initial weight at 280,000 lbs. Final altitude was set at 130,000 ft, final velocity at 14,000 ft/s, final inclination at 51.6 °, and final flight path angle at 0 °. For comparison, a nominal profile and an open-loop simulation is shown.

Table 7.14 Simulations with Varying Density Perturbations

Final Time, s	Final Weight, lbs	Final Altitude, ft	Final Velocity, ft/s	Type
179.6	234,360	130,060	14,010	Nominal
180.5	233,840	130,090	14,010	Closed-loop
179.6	233,470	127,450	14,240	Open-loop

Table 7.14 shows the varying density model required the vehicle to use more fuel, but is able to meet both the final altitude and velocity requirements with an additional second of flight time. The open-loop simulation is lower than the final altitude requirement and

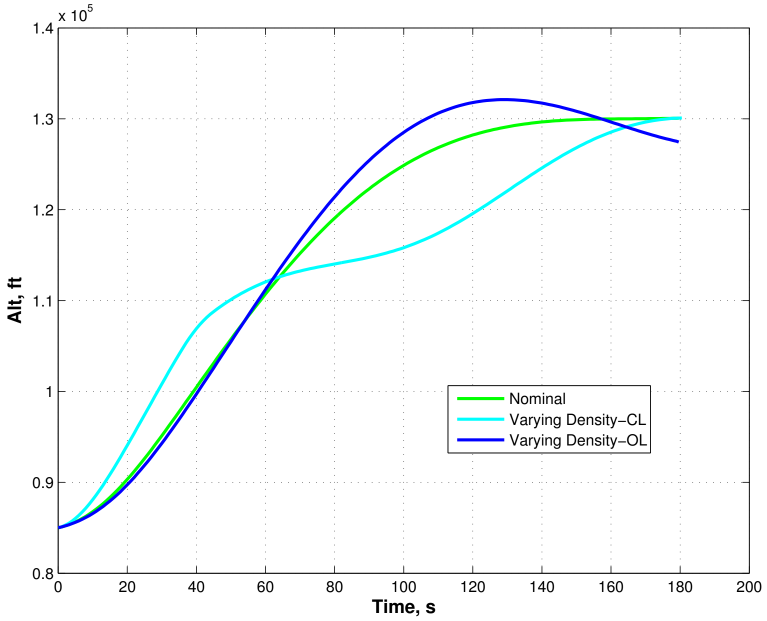

Figure 7.74 Simulations with Varying Density Perturbations - Altitude Comparison

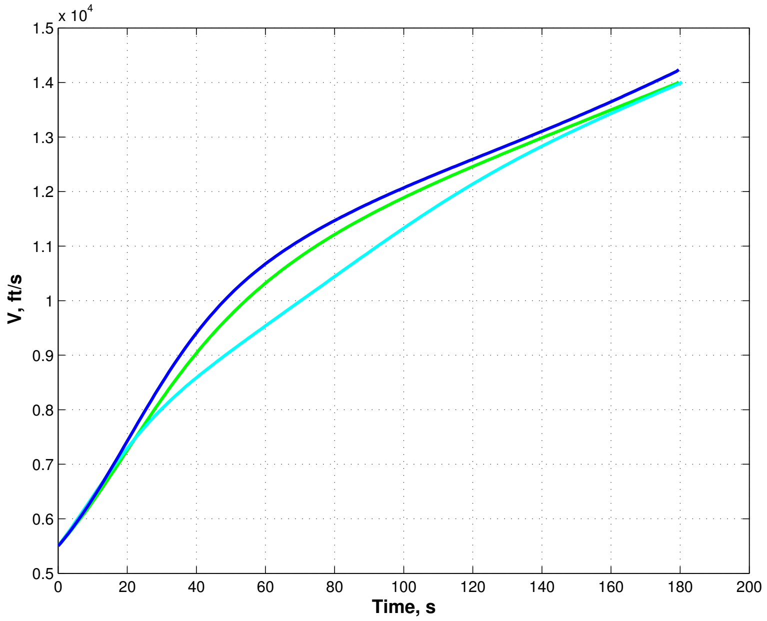

Figure 7.75 Simulations with Varying Density Perturbations - Velocity Comparison

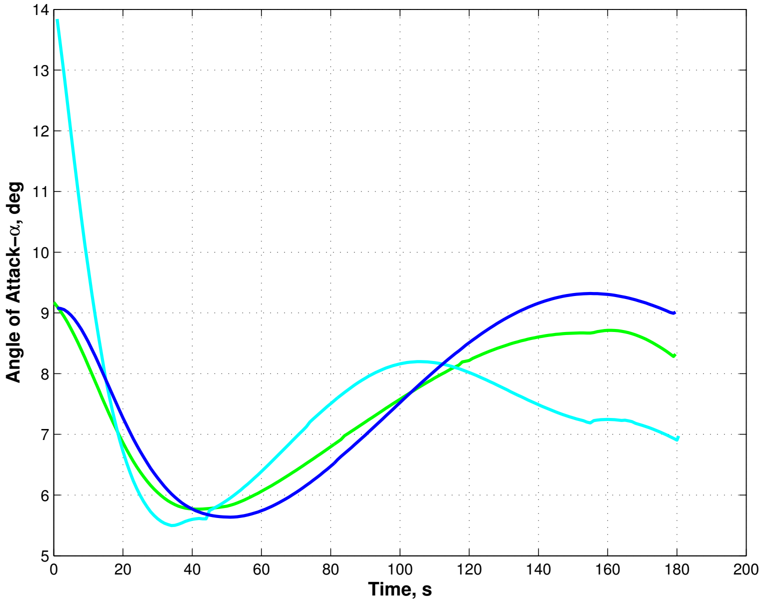

Figure 7.76 Simulations withVarying Density Perturbations - Angle-of-Attack Comparison

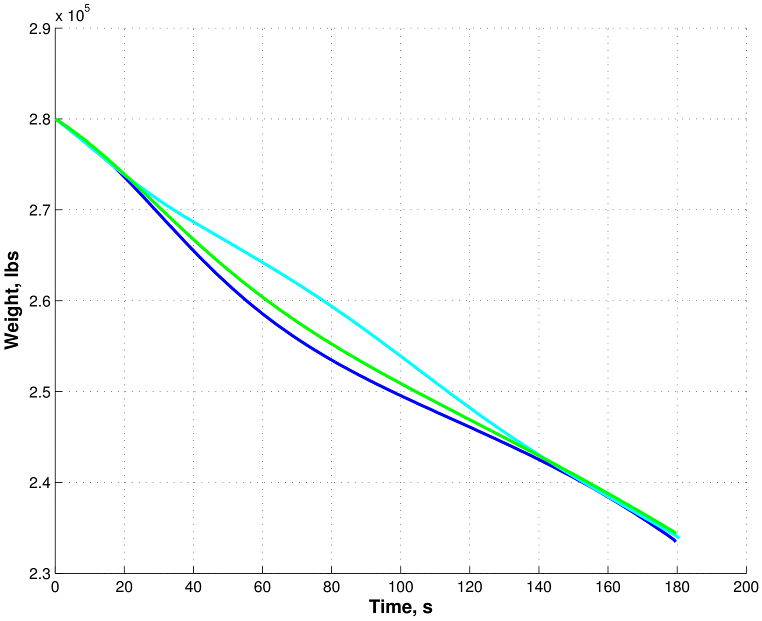

Figure 7.77 Simulations with Varying Density Perturbations - Weight Comparison

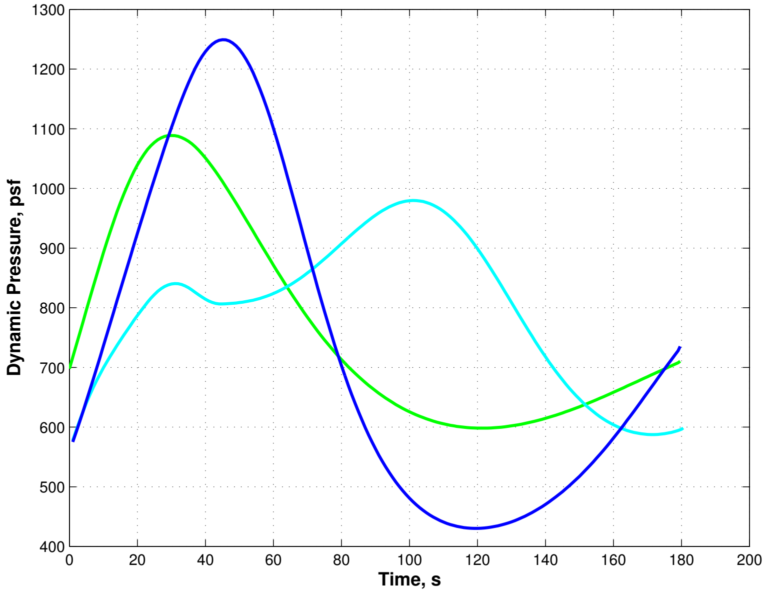

Figure 7.78 Simulations with Varying Density Perturbations - Dynamic Pressure Comparison

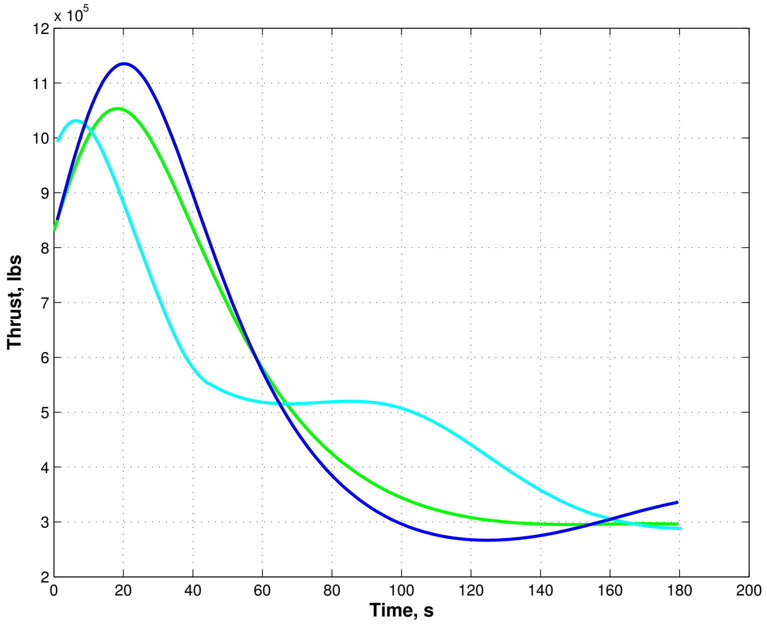

Figure 7.79 Simulations with Varying Density Perturbations - Thrust Comparison

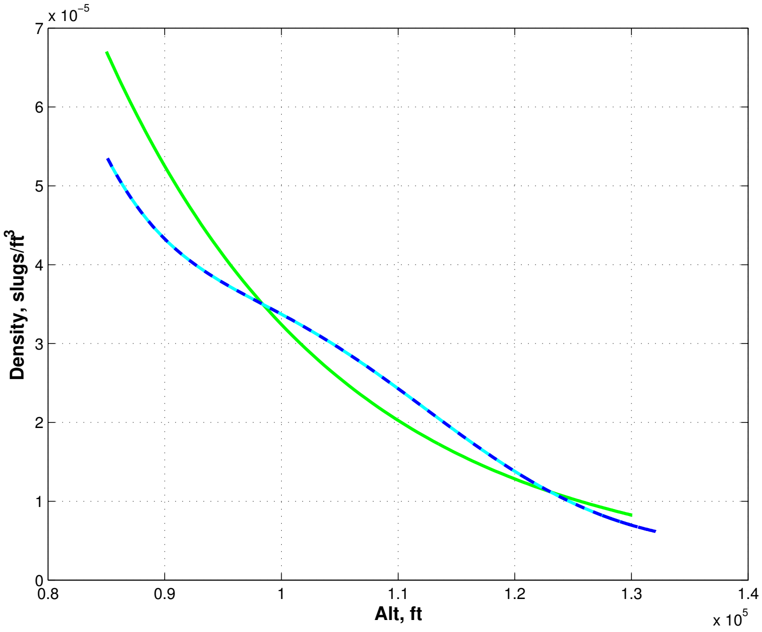

Figure 7.80 Simulations with Varying Density Perturbations - Density Comparison

faster than the final velocity requirement. The density comparison, Figure 7.80, shows that at lower altitude the perturbed density is lower and at altitudes above $100,000$ ft it is higher until approximately $125,000$ ft. The altitude profile of the closed-loop simulation shows the effect of the variability. The open-loop trajectory goes much higher than the targeted altitude midway in flight, but then drops in altitude and goes under than desired altitude.

7.3 Discussion

The ascent trajectory problem was formulated as a fuel-optimal control problem. A finite difference method was proposed to solve the resulting two-point boundary value problem. The preceding chapter showed that the finite difference method could solve a variety of ascent trajectories with and without path constraints. The various open-loop solutions show that the resulting trajectories are highly dependent on the engine model used. Although it is expected that an air-breathing scramjet engine would be a function of attitude, vehicle state, and throttle, the development of that model would effect the trajectories.

The initial and final conditions of trajectories also effected the trajectory profile. The initial conditions would be dependent on the efficiency of the previous engine cycles, particularly the ramjet engine portion. The final condition would depended on mission objective and if any additional engine cycles would be used, such as a rocket engine. As mentioned, the finite difference scheme could solve for a wide range of initial and final conditions. Some of the resulting trajectories seemed counterintuitive, but the evaluations of the trajectory profile validated the solutions.

The finite difference method also was shown to feasible as a guidance algorithm. Closed-loop simulations were shown to be accurate and the finite difference method was fast enough to be used as the guidance scheme. Even in the presence of constraints, atmospheric variations, engine model variations, and aerodynamic model variations, the vehicle was able to achieve the final conditions.

CHAPTER 8. SUMMARY AND CONCLUSION

This dissertation presented a method to generate a three-dimensional optimal ascent trajectory for hypersonic air-breathing vehicle. The commands were generated by solving the two point boundary value problem generated by the optimal control problem that minimized fuel usage. A finite difference scheme was used to solve the TPBVP numerically. Open-loop results were shown to describe the various characteristics of the ascent trajectory. Closed-loop simulations were done to show the potential for on-board trajectory optimization. The guidance algorithm was called once each guidance cycle and solved the optimal control problem using the current vehicle state, atmospheric effects, and path constraints.

A brief overview of optimal control theory was presented, showing the general formulation of an optimal control problem. The effects of state and control constraints on the control problem were reviewed. The optimal ascent of a hypersonic vehicle was then formulated, first by developing the equations of motion that govern the dynamics of the vehicle. The equations were then non-dimensionalized for numerical conditioning. Data for lift and drag coefficients, thrust coefficients, atmospheric density, and speed of sound were curve fitted to reduce the computational burden due to the aerodynamic model. Path constraints for dynamic pressure and angle-of-attack were considered in the formulation of the optimal control problem. The solution to the problem results in the optimal control, the body axis direction.

The vehicle selected for evaluation of the algorithm was GHAME model, developed at the NASA Dryden Flight Research Center. The model represents a single stage to orbit vehicle that is capable of taking off horizontally and accelerate to orbital velocities. The vehicles aerodynamic model is based loosely on empirical data. It included information from the space shuttle, lifting bodies, double-delta configuration vehicle, and theoretical data from 6 degree half-angle cones. The engine model was developed to represent the full flight envelope of the vehicle. Multiple engines are modeled, which included a turbojet cycle, a ramjet cycle, and scramjet cycle.

The classical finite difference method was selected to solve the two-point boundary value problem that results from the optimal control formulation. The algorithm takes advantage of a special structure of the Jacobian matrix and using Gauss eliminations and sequential back substitution, results in a fast and efficient algorithm. The initial guess for the algorithm was taken from a analytical vacuum optimal ascent guidance algorithm. Additionally, a secant method was used to adjust the final time because the finite difference method solves the fixed final time problem.

The guidance scheme was compared to a commercial optimization software based on a pseudospectral method for verification and validation. The same aerodynamic and engine model was used in both methods. The comparison supports the validity of the finite difference method. Then, various open-loop trajectories were generated to show the characteristics of trajectories for a hypersonic vehicle. Various initial and final conditions were shown, as well as trajectories with angle-of-attack constraints. Closed-loop simulations were also conducted to test the feasibility of using the guidance algorithm with a flight control system. Simulations were ran with various initial and final conditions, as well as simulations with both angle-of-attack and dynamic pressure constraints. Additionally, the simulations incorporated wind profiles to show that the guidance solution could incorporate winds and not need any pre-launch adjustment or a-priori planning. It was also shown that the closed-loop solution closely matched the open-loop solution. Lastly, simulations with perturbed atmospheric and vehicle models were conducted to illustrated the algorithms capability to handle such mis-modeling.

APPENDIX A. GHAME AERODYNAMIC MODEL

Tables

The aerodynamic data are arrays of size 9 by 13. The rows are Mach break points and the columns are angle-of-attack ,α, break points, which are given below. Just note that each row is broken into two lines of text to fit on the page.

$$\text{Mach} = [0.4\ 0.6\ 0.8\ 0.9\ 0.95\ 1.05\ 1.2\ 1.5\ 2.0\ 3.0\ 6.0\ 12.0\ 24.0] \tag{A.1}$$

$$\alpha = [-3.0\ 0.0\ 3.0\ 6.0\ 9.0\ 12.0\ 15.0\ 18.0\ 21.0] \tag{A.2}$$

Aerodynamic Tables

$C_{L_0} =$

0.04508	0.05491	0.04723	0.06222	0.06411	0.07569	0.06492
	0.04782	0.0348	0.01583	-0.00175	-0.00547	-0.00468
-0.03575	-0.0381	-0.04375	-0.038	-0.038	-0.0315	-0.03675
	-0.03905	-0.02965	-0.02475	-0.02075	-0.01871	-0.01562
-0.11693	-0.1169	-0.13532	-0.13317	-0.14505	-0.13861	-0.14068
	-0.12433	-0.09539	-0.06776	-0.04593	-0.03483	-0.02893
-0.22054	-0.21782	-0.23228	-0.22108	-0.25401	-0.23254	-0.25132
	-0.21391	-0.16617	-0.11392	-0.0791	-0.05409	-0.04481
-0.32599	-0.32773	-0.33138	-0.30955	-0.34726	-0.35937	-0.3657
	-0.31249	-0.24995	-0.17259	-0.12465	-0.08445	-0.06985
-0.4196	-0.43704	-0.43095	-0.43224	-0.44946	-0.49158	-0.42414
	-0.41519	-0.34693	-0.24957	-0.18941	-0.14139	-0.11688
-0.56105	-0.58493	-0.53773	-0.53748	-0.52428	-0.52394	-0.53246
	-0.48735	-0.42815	-0.32392	-0.26223	-0.21567	-0.17836
-0.72859	-0.68972	-0.61593	-0.60137	-0.52399	-0.54559	-0.6464
	-0.53332	-0.49102	-0.38885	-0.34431	-0.30273	-0.25036
-0.9232	-0.80347	-0.69635	-0.65836	-0.5002	-0.54335	-0.77975
	-0.56663	-0.54949	-0.45683	-0.4364	-0.40437	-0.33438

$C_{L_\alpha} =$

0.05483	0.05972	0.0617	0.06832	0.07085	0.07335	0.07145
	0.05858	0.04392	0.02805	0.01379	0.00956	0.00794
0.05472	0.05805	0.06173	0.06613	0.07078	0.07272	0.06948
	0.05817	0.04417	0.02854	0.01513	0.01012	0.0084
0.0546	0.05638	0.06177	0.06395	0.07072	0.07208	0.06752
	0.05775	0.04442	0.02904	0.01647	0.01068	0.00886
0.05827	0.05833	0.06255	0.06275	0.0717	0.06993	0.06987
	0.0583	0.04527	0.02967	0.01815	0.01139	0.00946
0.06087	0.0617	0.06328	0.06192	0.07006	0.07203	0.07093
	0.05973	0.0472	0.03138	0.02038	0.01297	0.01076
0.06092	0.06287	0.0637	0.06452	0.06976	0.0747	0.06717
	0.06097	0.04957	0.03409	0.02342	0.0163	0.0135
0.0644	0.06678	0.06455	0.06533	0.06792	0.06927	0.06722
	0.05978	0.05017	0.03582	0.02613	0.01986	0.01645
0.06872	0.06725	0.06368	0.06343	0.06215	0.06448	0.06847
	0.05725	0.0495	0.03651	0.02863	0.02319	0.01921
0.07303	0.06772	0.06282	0.06153	0.05638	0.0597	0.06972
	0.05472	0.04882	0.0372	0.03112	0.02652	0.02197]

C_{D_0} =

0.02941	0.03035	0.03127	0.03633	0.04871	0.06964	0.07106
	0.07076	0.06228	0.04472	0.02961	0.02122	0.01766
0.03594	0.03714	0.04141	0.04936	0.06265	0.08447	0.08354
	0.08047	0.07067	0.05161	0.03553	0.02584	0.0215
0.03261	0.03394	0.03647	0.04104	0.05359	0.07359	0.07468
	0.07486	0.06681	0.04947	0.03502	0.02583	0.0215
0.01436	0.01489	0.01049	0.01345	0.02174	0.04174	0.04369
	0.05006	0.04731	0.03597	0.02594	0.02021	0.01685
-0.02306	-0.02386	-0.04433	-0.03845	-0.04007	-0.0209	-0.01598
	0.0001	0.00808	0.00925	0.00672	0.00797	0.00672
-0.08415	-0.09375	-0.13162	-0.13204	-0.14179	-0.12953	-0.09461
	-0.07789	-0.05773	-0.03957	-0.02957	-0.01836	-0.01507
-0.18718	-0.23091	-0.25573	-0.25708	-0.26424	-0.25284	-0.23458
	-0.17409	-0.1419	-0.10402	-0.07789	-0.05742	-0.04744
-0.31882	-0.40962	-0.38482	-0.39617	-0.4082	-0.4232	-0.38219
	-0.31589	-0.26256	-0.19187	-0.14391	-0.11319	-0.09366
-0.47897	-0.62884	-0.54072	-0.56164	-0.5777	-0.62233	-0.56587
	-0.48309	-0.40512	-0.29579	-0.22221	-0.17988	-0.14894

C_{D_α} =

-0.00323	-0.00348	-0.00507	-0.00646	-0.00677	-0.00716	-0.00588
	-0.00475	-0.00419	-0.00356	-0.00319	-0.00256	-0.00213
-0.00107	-0.0012	-0.00173	-0.00157	-0.00163	-0.00132	-0.00121
	-0.00137	-0.00151	-0.00158	-0.0018	-0.00153	-0.00128
0.0011	0.00109	0.0016	0.00331	0.00352	0.00453	0.00347
	0.00201	0.00117	0.0004	-0.00041	-0.00051	-0.00043
0.00415	0.00425	0.00595	0.00764	0.00858	0.00939	0.00838
	0.00607	0.00448	0.00281	0.00139	0.00068	0.00056
0.00794	0.0082	0.0115	0.01248	0.01444	0.01514	0.01402
	0.011	0.00841	0.00554	0.00347	0.00204	0.00169
0.01227	0.01323	0.01769	0.01907	0.02153	0.02275	0.01922
	0.01645	0.01309	0.00908	0.00619	0.00407	0.00336
0.01816	0.02137	0.02453	0.02588	0.02791	0.0291	0.02683
	0.0215	0.01766	0.01269	0.00896	0.0064	0.00529
0.02424	0.02993	0.02995	0.0317	0.0338	0.03633	0.03326
	0.02777	0.02305	0.01663	0.01197	0.00904	0.00749
0.03033	0.03849	0.03537	0.03752	0.03969	0.04357	0.03969
	0.03404	0.02844	0.02057	0.01498	0.01169	0.00968

Engine Model Tables

The engine model data are arrays of size 9 by 13. For C_T, rows are Mach break points and the columns are angle-of-attack, α, break points. For I$_{sp}$, the rows are Mach break points and the columns are throttle position, ϕ_t. The breakpoints are given below.

$$\text{Mach} = [0.4\ 0.6\ 0.8\ 0.9\ 0.95\ 1.05\ 1.2\ 1.5\ 2.0\ 3.0\ 6.0\ 12.0\ 24.0] \tag{A.3}$$

$$\alpha = [-3.0\ 0.0\ 3.0\ 6.0\ 9.0\ 12.0\ 15.0\ 18.0\ 21.0] \tag{A.4}$$

$$\phi_t = [0.00\ 0.25\ 0.50\ 0.75\ 1.00\ 1.25\ 1.50\ 1.75\ 2.00] \tag{A.5}$$

$C_T =$

1.09449	0.5301	0.31459	0.26226	0.24452	0.22157	0.20981
	0.23464	0.34159	0.62377	1.45141	2.76052	4.68122
1.18766	0.58304	0.35204	0.29597	0.27698	0.25238	0.23978
	0.26638	0.38098	0.68332	1.57007	2.97269	5.03057
1.28082	0.63590	0.38950	0.32969	0.30943	0.28319	0.26975
	0.29813	0.42037	0.74286	1.68873	3.18486	5.37993
1.37399	0.68875	0.42696	0.36341 0	.34188	0.31401	0.29973
	0.32987	0.45975	0.80240	1.80739	3.39702	5.72929
1.46715	0.74161	0.46441	0.39713	0.37433	0.34482	0.32970
	0.36162	0.49914	0.86194	1.92605	3.60919	6.07865
1.56032	0.79447	0.50187	0.43085	0.40679	0.37563	0.35967
	0.39337	0.53852	0.92148	2.04471	3.82136	6.42801
1.65348	0.84732	0.53933	0.46457	0.43924	0.40644	0.38964
	0.42511	0.57791	0.98102	2.16336	4.03352	6.77737
1.74664	0.90018	0.57678	0.49829	0.47169	0.43726	0.41962
	0.45688	0.61729	1.04057	2.28202	4.24569	7.12673
1.83981	0.95304	0.61424	0.53201	0.50414	0.46807	0.44959
	0.48860	0.65668	1.10011	2.40068	4.45786	7.47609

I_{sp}=

0000.0000	0000.0000	0000.0000	0000.0000	0000.0000	0000.0000	0000.0000
	0000.0000	0000.0000	0000.0000	0000.0000	0000.0000	0000.0000
1693.1500	1693.1500	1686.9000	1682.2125	1679.0875	1661.9000	1636.9000
	1568.1500	1443.1500	1568.1500	1318.1500	0755.6500	0505.6500
2262.3999	2262.3999	2253.5625	2246.9343	2242.5156	2218.2126	2182.8625
	2085.6499	1908.9000	2085.6499	1732.1499	0936.7750	0583.2750
2699.6499	2699.6499	2688.8250	2680.7063	2675.2937	2645.5249	2602.2251
	2483.1499	2266.6501	2483.1499	2050.1499	1075.9000	0642.9000
3068.1499	3068.1499	3055.6499	3046.2749	3040.0249	3005.6499	2955.6499
	2818.1499	2568.1499	2818.1499	2318.1499	1193.1500	0693.1500
3392.6501	3392.6501	3378.6748	3368.1936	3361.2063	3322.7749	3266.8750
	3113.1499	2833.6499	3113.1499	2554.1501	1296.4000	0737.4000
3686.8999	3686.8999	3671.5874	3660.1030	3652.4468	3610.3374	3549.0874
	3380.6499	3074.3999	3380.6499	2768.1499	1390.0250	0777.5250
3956.4001	3956.4001	3939.8625	3927.4595	3919.1907	3873.7124	3807.5625
	3625.6499	3294.8999	3625.6499	2964.1501	1475.7750	0814.2750
4206.6499	4206.6499	4188.9751	4175.7188	4166.8813	4118.2749	4047.5750
	3853.1499	3499.6499	3853.1499	3146.1499	1555.4000	0848.4000

Curve Fits

The following equations represent the curve fits to the data in the previous tables, where α is angle-of-attack, M_a is Mach number, and ϕ_t is the engine throttle seen in the thrust equation.

$$\begin{aligned} y &= \alpha && \text{(A.6)} \\ x &= \frac{1.0}{M_a} && \text{(A.7)} \end{aligned}$$

$$\begin{aligned} C_{D_0} &= 0.02288046350678314 + x*(-0.009838883993226041 + \\ &\quad x*(0.5191974766999029 + x*(-0.6054070629390214))) + \\ &\quad y*(0.0004492661130680898 + y*(-0.0001089326853701854 + \\ &\quad y*(-1.245491956603068\text{E-}05))) + x*y*(0.005322199262109339 + \\ &\quad y*(-0.001552558275058275) + x*(-0.006230753754297086)) && \text{(A.8)} \\ C_{D_\alpha} &= -0.001711432610477896 + x*(0.003113436406775853 + \\ &\quad x*(-0.02328020149614377 + x*(0.03471224427423899))) + \\ &\quad y*(0.0001836383876779103 + y*(1.503198421948422\text{E-}05 + \\ &\quad y*(-6.403541588726772\text{E-}08))) + x*y*(0.001373090167597314 + \\ &\quad y*(2.274919524919525\text{E-}05) + x*(0.0001312248959652615)) && \text{(A.9)} \\ C_{L_0} &= 0.01525858829887088 + x*(-0.5487052370434285 + \\ &\quad x*(2.365405789423327 + x*(-2.918197694819037))) + \\ &\quad y*(0.002628151805075891 + y*(-0.0009599723118316869 \\ &\quad +y*(3.915139044768676\text{E-}06))) + x*y*(-0.05342505647854649 \\ &\quad +y*(0.001639042138417138) + x*(0.0008215234304324364)) && \text{(A.10)} \end{aligned}$$

$$\begin{aligned} C_{L_\alpha} &= 0.004056183731744061 + x * (0.07649021439311123 + \\ &\quad x * (-0.07390202521762121 + x * (0.1634541706944361))) + \\ &\quad y * (-8.894049021791353\text{E-}05 + y * (6.502099116161616\text{E-}05 + \\ &\quad y * (-1.212869435091657\text{E-}06))) + x * y * (0.001871609094346339 + \\ &\quad y * (-8.018308080808081\text{E-}05) + x * (-0.002465907725710150)) \end{aligned} \tag{A.11}$$

$$y = \log(M_a) \tag{A.12}$$

$$x = \alpha \tag{A.13}$$

$$\begin{aligned} C_T &= 0.2600464082059642 + \\ &\quad x * (0.01527537816578171 + x * (-1.924001924002474\text{E-}08)) + \\ &\quad y * (-0.6017185588104934 + y * (0.6909092174165687)) + \\ &\quad x * y * (0.02169241439073307) \end{aligned} \tag{A.14}$$

$$f1 = \frac{1}{\sqrt{\phi_t}} \tag{A.15}$$

$$f2 = \frac{1}{\phi_t} \tag{A.16}$$

$$f3 = M_a \tag{A.17}$$

$$f4 = M_a * \log(M_a) \tag{A.18}$$

$$f5 = M_a * \sqrt{M_a} \tag{A.19}$$

$$f6 = M_a * M_a \tag{A.20}$$

$$f7 = M_a * M_a * \log(M_a) \tag{A.21}$$

$$\begin{aligned} z &= 0.1040565990642441 + 0.3649668348281674 * f1 \\ &\quad -0.02987940888679714 * f2 + 1.455398174797576 * f3 \\ &\quad +0.7012132017557569 * f4 - 2.188899162976031 * f5 \\ &\quad +0.6295934403674957 * f6 - 0.1053092147726738 * f7 \qquad \text{(A.22)} \\ z &= \frac{1}{z} \qquad \text{(A.23)} \\ \mathrm{I}_{sp} &= 1000.0 * z \qquad \text{(A.24)} \end{aligned}$$

APPENDIX B. EXPANDED COSTATE EQUATIONS

$$
\begin{aligned}
&\vec{\mathbf{P}}'_r = \frac{1}{r^3}\vec{\mathbf{P}}_V + \Bigg\{ \frac{-3\left(\vec{\mathbf{P}}_V^T\vec{\mathbf{r}}\right)}{r^4} + \vec{\mathbf{P}}_V^T\vec{\mathbf{1}}_b\left(\frac{R_0 S_{\text{ref}} A_1}{2m_0 m} - \chi\tau_2\right) - \\
&\vec{\mathbf{P}}_V^T\vec{\mathbf{1}}_n\frac{R_0 S_{\text{ref}} N_1}{2m_0 m} + \sqrt{\frac{R_0}{G_0}}mP_m\left(\frac{\chi\tau_2}{\mathrm{I}_{sp}} + \frac{TM_a}{\mathrm{I}_{sp}^2 V_s}\frac{\partial \mathrm{I}_{sp}}{\partial M_a}\frac{\partial V_s}{\partial r}\right)\Bigg\}\frac{\vec{\mathbf{r}}}{r} + \\
&\Bigg\{\vec{\mathbf{P}}_V^T\vec{\mathbf{1}}_b\left(\frac{R_0 S_{\text{ref}} A_2}{2m_0 m} - \chi\tau_1\right) - \vec{\mathbf{P}}_V^T\vec{\mathbf{1}}_n\frac{R_0 S_{\text{ref}} N_2}{2m_0 m} + \\
&m\sqrt{\frac{R_0}{G_0}}P_m\left(\frac{\chi}{\mathrm{I}_{sp}}\tau_1 - \frac{T}{\mathrm{I}_{sp}^2 V_s V_r}\frac{\partial \mathrm{I}_{sp}}{\partial M_a}\right)\Bigg\}\left(\vec{\omega}_e \times \vec{\mathbf{V}}_r\right) + \\
&\Bigg\{\vec{\mathbf{P}}_V^T\vec{\mathbf{1}}_b\left(\frac{R_0 S_{\text{ref}}\rho V_r^2}{2m_0 m}\frac{\partial C_A}{\partial\alpha} - \chi\rho V_r \mathrm{I}_{sp}\frac{\partial C_T}{\partial\alpha}\right) - \\
&\vec{\mathbf{P}}_V^T\vec{\mathbf{1}}_n\frac{R_0 S_{\text{ref}}\rho V_r^2}{2m_0 m}\frac{\partial C_n}{\partial\alpha} + \sqrt{\frac{R_0}{G_0}}\frac{\chi m P_m}{\mathrm{I}_{sp}}\rho V_r\frac{\partial C_T}{\partial\alpha}\Bigg\}\left(\vec{\omega}_e \times \frac{\partial\alpha}{\partial\vec{\mathbf{V}}}\right)
\end{aligned}
\tag{B.1}
$$

$$\chi = \sqrt{\frac{G_0}{R_0}}\left(0.029\phi_t\right)\frac{R_0}{m_0 m}A_c \tag{B.2}$$

$$\tau_1 = \frac{\rho M_a C_T}{V_r}\frac{\partial \mathrm{I}_{sp}}{\partial M_a} + \frac{\rho C_T \mathrm{I}_{sp}}{V_r} + \frac{\rho}{V_s}\mathrm{I}_{sp}\frac{\partial C_T}{\partial\alpha} \tag{B.3}$$

$$\tau_2 = \mathrm{I}_{sp}V_r C_T\frac{\partial\rho}{\partial r} - \rho M_A^2\left(C_T\frac{\partial \mathrm{I}_{sp}}{\partial M_a}\frac{\partial V_s}{\partial r} + \mathrm{I}_{sp}\frac{\partial C_T}{\partial M_a}\frac{\partial V_s}{\partial r}\right) \tag{B.4}$$

$$A_1 = V_r^2 C_A\frac{\partial\rho}{\partial r} - \rho V_r M_a^2\frac{\partial C_A}{\partial M_a}\frac{\partial V_s}{\partial r} \tag{B.5}$$

$$A_2 = 2\rho C_A + \rho M_a\frac{\partial C_A}{\partial M_a} \tag{B.6}$$

$$N_1 = V_r^2 C_N\frac{\partial\rho}{\partial r} - \rho V_r M_a^2\frac{\partial C_N}{\partial M_a}\frac{\partial V_s}{\partial r} \tag{B.7}$$

$$N_2 = 2\rho C_N + \rho M_a\frac{\partial C_N}{\partial M_a} \tag{B.8}$$

$$\begin{aligned}\vec{\mathbf{P}}'_V &= \vec{\mathbf{P}}_r + \left\{\vec{\mathbf{P}}_V^T\vec{\mathbf{1}}_b\left(\bar{A}_1 + \bar{A}_3 - \frac{\chi\rho\bar{\tau}_1}{V}\right) - \vec{\mathbf{P}}_V^T\vec{\mathbf{1}}_n\left(\bar{N}_1 + \bar{N}_3\right) + \right. \\ &\quad \left. mP_m\sqrt{\frac{R_0}{G_0}}\left(\frac{\rho\chi}{\mathrm{I}_{sp}}\frac{\bar{\tau}_1}{V} + \frac{T}{V}\frac{\partial \mathrm{I}_{sp}}{\partial M_a}\frac{\partial M_a}{\partial V_r}\right)\right\}\vec{\mathbf{V}} + \\ &\quad \left\{-\vec{\mathbf{P}}_V^T\vec{\mathbf{1}}_b\left(\bar{\tau}_2 + \bar{A}_2\right) - \vec{\mathbf{P}}_V^T\vec{\mathbf{1}}_n N_2 + P_m\sqrt{\frac{R_0}{G_0}}m\frac{\chi\rho\bar{\tau}_2}{\mathrm{I}_{sp}}\right\}\frac{\partial\alpha}{\partial\vec{\mathbf{V}}} \end{aligned} \tag{B.9}$$

$$\chi = \sqrt{\frac{G_0}{R_0}}\left(0.029\phi_t\right)\frac{R_0}{m_0 m}A_c \tag{B.10}$$

$$\bar{\tau}_1 = V_r C_T\frac{\partial \mathrm{I}_{sp}}{\partial M_a}\frac{\partial M_a}{\partial V_r} + \mathrm{I}_{sp}C_t + \mathrm{I}_{sp}V_r\frac{\partial C_T}{\partial M_a}\frac{\partial M_a}{\partial V_r} \tag{B.11}$$

$$\bar{\tau}_2 = \mathrm{I}_{sp}V_r\frac{\partial C_T}{\partial\alpha} \tag{B.12}$$

$$\bar{A}_1 = \frac{R_0}{m}\rho S_{\mathrm{ref}}\frac{V_r}{V}C_A \tag{B.13}$$

$$\bar{A}_2 = \frac{1}{2}\frac{R_0}{m}\rho S_{\mathrm{ref}}V_r^2\frac{\partial C_A}{\partial\alpha} \tag{B.14}$$

$$\bar{A}_3 = \frac{1}{2}\frac{R_0}{m}\rho S_{\mathrm{ref}}\frac{V_r^2}{VV_S}\frac{\partial C_A}{\partial M_a} \tag{B.15}$$

$$\bar{N}_1 = \frac{R_0}{m}\rho S_{\mathrm{ref}}\frac{V_r}{V}C_N \tag{B.16}$$

$$\bar{N}_2 = \frac{1}{2}\frac{R_0}{m}\rho S_{\mathrm{ref}}V_r^2\frac{\partial C_N}{\partial\alpha} \tag{B.17}$$

$$\bar{N}_3 = \frac{1}{2}\frac{R_0}{m}\rho S_{\mathrm{ref}}\frac{V_r^2}{VV_S}\frac{\partial C_A}{\partial M_a} \tag{B.18}$$

$$P'_m = \left(\rho\frac{R_0}{m_0}V_r\right)\left[\left(\sqrt{\frac{G_0}{R_0}}\mathrm{I}_{sp}\pi C_T A_c - \frac{1}{2}V_r S_{\mathrm{ref}}C_A\right)\vec{\mathbf{P}}_V^T\vec{\mathbf{1}}_b + \left(\frac{1}{2}V_r S_{\mathrm{ref}}C_N\right)\vec{\mathbf{P}}_V^T\vec{\mathbf{1}}_n\right] \tag{B.19}$$

BIBLIOGRAPHY

[1] Heppenheimer, T. A., *Facing the Heat Barrier: A History of Hypersonics* NASA SP-2007-4232, 2007.

[2] Weber, R. J., MacKay, J. S., “An Analysis of Ramjet Engines Using Supersonic Combustion”, NACA TN-4386, 1958.

[3] Hardtla, J. W., Piehler, M. J., Bradt, J. E., “Guidance Requirements for Future Launch Vehicles”, AIAA-1987-2462 , AIAA Guidance, Navigation and Control Conference, Monterey, CA, Aug 17-19, 1987.

[4] Hicks, J. W., Trippensee, G., “NASA Hypersonic X-Plane Flight Development of Technologies and Capabilities for the 21st Century Access to Space”, AGARD Future Aerospace Technology in Service to the Alliance, Paris, France, April 14-18, 1997.

[5] Wagner, E. A., Li, I., Nguyen, D. D., Nguyen, P. L., “NASP Guidance Design for Vehicle Autonomy”, AIAA-1990-5245, International Aerospace Planes Conference, Orlando, FL, Oct 29-31, 1990.

[6] Calise, A. J., Corban, J. E., Flandro, G. A., “Trajectory Optimization and Guidance Law Development for National Aerospace Plane Applications”, American Control Conference, Atlanta, GA, June 15-17, 1988.

[7] Corban, J.E., Calise, A.J., Flandro, G.A.,"Trajectory optimization and guidance law development for transatmospheric vehicles", IEEE International Conference on Control and Applications, Jerusalem, Israel, April 3-6, 1989.

[8] Corban, J. E., Calise, A. J., Flandro, G. A., "Optimal Guidance and Propulsion Control for Transatmospheric Vehicles", AIAA-1989-3617, AIAA Guidance, Navigation and Control Conference, Boston, MA, Aug 14-16, 1989.

[9] Corban, J. E., Calise, A. J., Flandro, G. A., "Rapid Near-Optimal Aerospace Plane Trajectory Generation and Guidance", *Journal of Guidance, Control, and Dynamics*, Vol. 14, No. 6, 1991, pp 1181-1190.

[10] Cliff, E. M., Well, K. H., "Energy-Heading Transients in Atmospheric Flight Guidance for Airbreathing Hypersonic Vehicles", AIAA-91-5065, AIAA International Aerospace Planes Conference, Orlando, FL, Dec 3-5, 1991.

[11] Cliff, E. M., Well, K. H., Schneper, K. , "Flight-test guidance for airbreathing hypersonic vehicles ", AIAA-92-4301, AIAA Guidance, Navigation and Control Conference, Hilton Head Island, SC, Aug 10-12, 1992.

[12] Van Buren, M. A., Mease, K. D., "Minimum-Fuel Ascent to Orbit using Air-Breathing Propulsion," American Control Conference, Pittsburgh, PA, June 21-23, 1989.

[13] Van Buren, M. A., Mease, K. D., "A Geometric Approach to Regulator and Tracker Design for an Aerospace Plane," AIAA-91-5054, AIAA International Aerospace Planes Conference, Orlando, FL, Dec 3-5, 1991.

[14] Van Buren, M. A,, and Mease, K. D., "Aerospace Plane Guidance Using Time-Scale Decomposition and Feedback Linearization, *Journal of Guidance, Control, and Dynamics*, Vol. 15, No. 5, 1992, pp. 1166-1174.

[15] Schmidt, D. K., Velapoldi, J., "Optimum Mission Performance and Guidance for Hypersonic Single Stage to Orbit", AIAA-96-3904, AIAA Guidance, Navigation and Control Conference, San Diego, CA, July 29-31, 1996.

[16] Schmidt, D. K., "Optimum Mission Performance and Multivariable Flight Guidance for Airbreathing Launch Vehicles", *Journal of Guidance, Control, and Dynamics*, Vol. 20, No. 6, 1997, pp 1157-1164.

[17] Schmidt, D. K., Hermann, J. A., "Use of Energy-State Analysis on a Generic Air-Breathing Hypersonic Vehicle", *Journal of Guidance, Control, and Dynamics*, Vol. 21, No. 1, 1998, pp 71-76.

[18] Kremer, J. P., Mease, K. D., "Near-Optimal Control of Altitude and Path Angle During Aerospace Plane Ascent", *Journal of Guidance, Control, and Dynamics*, Vol. 20, No. 4, 1997, pp 789-796.

[19] Lu, P., "Trajectory Optimization and Guidance for a Hypersonic Vehicle", AIAA-91-5068, AIAA International Aerospace Planes Conference, Orlando, FL, December 3-5, 1991.

[20] Lu, P., "Trajectory Optimization for the National Aerospace Plane: Final Report, 1 May 1991- 30 May 1992", NASA-CR-190355 , June 1992.

[21] Lu, P., "Inverse Dynamics Approach to Trajectory Optimization for an Aerospace Plane", *Journal of Guidance, Control, and Dynamics*, Vol. 16, No. 4, 1993, pp. 726-732.

[22] Lu, P., "Analytical Solutions to Constrained Hypersonic Flight Trajectories", *Journal of Guidance, Control, and Dynamics*, Vol. 16, No. 5, 1993, pp. 956-960.

[23] Lu, P., "Trajectory Optimization for the National Aerospace Plane: Final Report, 13 June 1992 - 30 Oct 1993", NASA-CR-194618, November, 1993.

[24] Paus, M., Well, K. H., “Optimal Ascent Guidance for a Hypersonic Vehicle”, AIAA-96-3901, AIAA Guidance, Navigation and Control Conference, San Diego, CA, July 29-31, 1996.

[25] Doman, D. B., Oppenheimer, M. W., Bolender, M. A., “Progress in Guidance and Control Research for Space Access and Hypersonic Vehicles, IEEE Conference on Decision & Control, San Diego, CA, December, 2006.

[26] Lu, P., Sun, H., Tsai, B., “Closed-Looop Endoatmospheric Ascent Guidance”, *Journal of Guidance, Control, and Dynamics*, Vol. 26, No. 2, 2003, pp. 283-294.

[27] Sun, H., “Closed-loop endo-atmospheric ascent guidance for reusable launch vehicle”, Ph. D. Dissertation, Department of Aerospace Engineering , Iowa State University, Ames, IA, 2005.

[28] Bryson, A. E., Ho, Y.-C., *Applied Optimal Control: Optimization, Estimation, and Control*, Taylor & Francis Group, LLC., New York, NY, 1975, pp. 1-89.

[29] Lewis, F. L., Syrmos, V. L., *Optimal Control*, John Wiley & Sons, Inc., New York, NY, 1995.

[30] White, D. A., Bowers, A., Iliff, K., and Menousek, J., “Flight, Propulsion, and Thermal Control of Advanced Aircraft and Hypersonic Vehicles”, *Handbook of Intelligent Control: Neural, Fuzzy, and Adaptive Approaches*, Multiscience Press, Inc., New York, NY, 1992, pp 357-465.

[31] Zipfel, P. H., *Modeling and Simulation of Aerospace Vehicle Dynamics*, American Institute of Aeronautics and Astronautics, Inc., Reston, VA, 2000, pp 273-276.

[32] Keller, H. B., *Numerical Methods for Two-Point Boundary-Value Problems*, Blaisdell Publishing Company, Waltham, MA, 1968, pp 91-100.

[33] Stoer, J., and Bulirsch, R., *Introduction to Numerical Analysis*, Springer-Verlag, New York, 1980, pp. 256-262.

[34] Press, W. H. *et al.*, *Numerical Recipes in FORTRAN*, Cambridge, University Press, Cambridge, UK, 1992, pp. 753-759.

[35] Ross, I. M., and Fahroo, F., “User’s Manual for DIDO 2001 (α): A MATLAB$^{\text{TM}}$Application Package for Dynamic Optimization”, Technical Report NPS-A-01-003, October 2001, Naval Postgraduate School, Monterey, CA.